

# Flexible Micro/Nanofabricated Systems for Medical Devices and Implants

THÈSE N° 5512 (2013)

PRÉSENTÉE LE 7 MARS 2013

À LA FACULTÉ DES SCIENCES ET TECHNIQUES DE L'INGÉNIEUR  
LABORATOIRE DE MICROSYSTÈMES 4  
PROGRAMME DOCTORAL EN BIOTECHNOLOGIE ET GÉNIE BIOLOGIQUE

ÉCOLE POLYTECHNIQUE FÉDÉRALE DE LAUSANNE

POUR L'OBTENTION DU GRADE DE DOCTEUR ÈS SCIENCES

PAR

Willyan HASENKAMP CARREIRA

acceptée sur proposition du jury:

Prof. N. Stergiopoulos, président du jury  
Prof. Ph. Renaud, directeur de thèse  
Prof. K. Aminian, rapporteur  
Dr W. Eberle, rapporteur  
Dr H. Pereira Neves, rapporteur



ÉCOLE POLYTECHNIQUE  
FÉDÉRALE DE LAUSANNE

Suisse  
2013



with love to  
*Evelise Bastos de Braga*

and

in the loving memory of  
*Marinês Hasenkamp*

***In the Middle of the Road***

*In the Middle of the Road*

*In the middle of the road there was a stone  
there was a stone in the middle of the road  
there was a stone  
in the middle of the road there was a stone.*

*Never should I forget this event*

*in the life of my fatigued retinas.*

*Never should I forget that in the middle of the road  
there was a stone*

*there was a stone in the middle of the road  
in the middle of the road there was a stone.*

Carlos Drummond de Andrade  
1902–1987

# Acknowledgements

I will forever be indebted to a great person and teacher, who became my mentor and friend, Professor Philippe Renaud. He gave me a great opportunity to expand and succeed by providing unlimited advice and support throughout all this time.

I thank Dr. Andre Mercanzini for believing in me, for helping to get this PhD position and for the friendship through these hard days. I sincerely thank Dr. Arnaud Bertsch for being a great motivator and for helping in all necessary matters to execute this work.

Also, I truly enjoyed the company and friendship of my current and former colleagues at the Microsystems Laboratory (LMIS4), Kristopher Pataky, Harsha Kasi, Robert Meissner, Pierre Joris, Carmen Biagini, Sylvie Clavel, Bilge Eker, Rodrigo Martinez Duarte, Harald Van Lintel, Sophie Baranek, Nina Buffi, Ludovica Colella, Anja Kunze, Mojtaba Taghipoor, Fabien Wildhaber, Elodie Dahan, Marc Olivier Heuschkel, Pietro Maoddi, Alessandro Mapelli, Sebastien Jiguet, and Matteo Leonardi. It is impossible to summarize the debt of gratitude I owe to everyone that has helped me through these years.

I've spend quite long time in the EPFL clean room, the Centre for MicroNanoTechnology (CMI). I made good friends and had the chance to learn from the best. I thank all the CMI staff for their support, ideas, and professionalism. I sincerely thank Boris Lunardi for his amazing dedication and good humor, Cyrille Hibert for his help and advise, and Philippe Flückiger for managing this great working environment and, as some might say, "the best clean room in

the world".

A great part of this accomplishment is due to the support of my family. Specially, my three wonderful aunts: Marlise, Marly, and Marlene, my lovely sister, Nataly and my fantastic godfather, Ricardo. Also, I would like to express my deepest gratitude to Raquel, Edson and Edgar, which I became to love unconditionally as family.

Finally, I thank my great and beautiful wife, Evelise, for her unrelenting dedication during all this years. Without having her by my side and her loving support, I could never have achieved this goal.

# Publications

A number of publications have been originated during the course of this project and they are the base for this thesis.

- G. Mernier, W. Hasenkamp, N. Piacentini, and P. Renaud, *Multiple-frequency impedance measurements in continuous flow for the evaluation of electrical lysis of yeast cells*, *Procedia Engineering*, vol. 5, pp. 37-40, Jan. 2010.
- G. Mernier, W. Hasenkamp, N. Piacentini, and P. Renaud, *Multiple-frequency Impedance Measurements in Continuous Flow for Automated Evaluation of Yeast Cell Lysis*, *Sensors and Actuators B: Chemical*, Nov. 2010.
- H. Kasi, W. Hasenkamp, G. Cosendai, A. Bertsch, and P. Renaud, *Simulation of epiretinal prostheses - Evaluation of geometrical factors affecting stimulation thresholds.*, *Journal of neuroengineering and rehabilitation*, vol. 8, no. 1, p. 44, Aug. 2011.
- A. Arami, M. Simoncini, O. Atasoy, W. Hasenkamp, S. Ali, A. Bertsch, E. Meurvell, S. Tanner, H. Dejnabadi, V. Leclercq, P. Renaud, C. Dehollain, P. A. Farine, B. M. Jolles, K. Aminian, P. Ryser, *Instrumented prosthesis for knee implants monitoring*, 2011 IEEE International Conference on Automation Science and Engineering, 2011, pp. 828-835.
- W. Hasenkamp, D. Forchelet, K. Pataky, J. Villard, H. V. Lintel, A. Bertsch, Q. Wang, and P. Renaud, *Polyimide/su-8 catheter-tip mems gauge pressure sensor*, *Biomedical Microdevices*, May 2012.
- W. Hasenkamp, J. Villard, J. R. Delaloye, A. Arami, A. Bertsch, B. Jolles-Haeberli, K. Aminian, P. Renaud, *Smart Instrumentation for Determination of*

*Ligament Stiffness and Ligament Balance in Total Knee Arthroplasty, Medical Engineering Physics - accepted.*

- W. Hasenkamp, N. Thevenaz, J. Villard, A. Bertsch, A. Arami, K. Aminian, A. Terrier, P. Renaud, *Design and Test of a MEMS Strain-Sensing Device for Monitoring Artificial Knee Implants.*, Biomedical Microdevices - submitted.



# Abstract

MEMS technology has exerted a significant impact on sensing practices as more complex and sophisticated devices are developed in response to emerging needs in a wide range of industries. The introduction of microsystems into the biomedical and health sciences can substantially contribute to significant advancements in the biomedical tools while reducing healthcare costs. Therefore, this thesis will focus in three applications of BioMEMS: (i) smart medical instrumentation, (ii) sensors for artificial knee implants and (iii) catheter pressure sensors.

In the first application, we have developed a smart medical instrumentation that has its direct utilization in ligament balance during total knee arthroplasty (TKA) procedure. The "instrumented distractor" proposed in this thesis can assist surgeons in performing ligament balance by measuring the distraction gap and applied load. Also, the device allows the determination of the ligament stiffness which can contribute for a better understanding of the intrinsic mechanical behavior of the knee joint. The smart medical instrumentation involved the use of Hall sensors for measuring the distractor displacement and strain gauges to transduce the force. The sensors were calibrated and tested to demonstrate their suitability for surgical use. Results show that the distraction gap can be measured reliably with 0.1 mm accuracy and the distractive loads could be assessed with an accuracy in the range of 2 N. These characteristics fill the need surgeons have for a device to perform ligament balance while enabling the surgeon's evaluation based on his experience. Preliminary results from *in vitro* tests were in accordance with expected stiffness values for medial collateral ligament (MCL) and lateral collateral ligament (LCL).

The second application of BioMEMS is focused on the development of a polyimide-based MEMS strain-sensing device capable of measuring forces in an artificial knee implant. Finite element analysis was used to investigate an artificial knee implant, assist on the design of the sensor and optimize sensing characteristics. The sensing element of the device was fabricated using polyimide micromachining with embedded thin metallic wires and placed into a knee prosthesis. The device was evaluated experimentally in a mechanical knee simulator using static and dynamic axial load conditions similar to those encountered *in vivo*. Results indicate the sensor is capable of measuring the strain associated to the total axial forces in the range of approximately 4 times body weight with a good sensitivity and accuracy for events happening within 1s time window.

In the third application, we describe the development of a polyimide/SU-8 catheter-tip MEMS gauge pressure sensor. Finite element analysis was used to investigate critical parameters, impacting on the device design and sensing characteristics. The sensing element of the device is fabricated by polyimide-based micromachining on a flexible membrane, using embedded thin-film metallic wires as piezoresistive elements. A chamber containing this flexible membrane was sealed using an adapted SU-8 bonding technique. The device was evaluated experimentally and its overall performance compared with a commercial silicon-based pressure sensor. Furthermore, the device use was demonstrated by measuring blood pressure and heart rate *in vivo*.

**Keywords:** MEMS, BioMEMS, Biomedical Devices, Bioengineering, Biomechanics, Implantable sensor, Metal thin-film gauges, Metallic thin films, Micro strain sensor, Microfabricated strain gauges, Microsensors, Polymers, Real-time monitoring, Strain gauge, Strain gauges, Strain measurement, Strain sensors, Thin film metal strain gauges.

# Résumé

La technologie MEMS devient de plus en plus utilisés pour créer des capteurs sophistiqués pour des applications émergentes. L'utilisation de la micro et nanotechnologie en science de la vie et dans la science biomédicale permettra des avancées techniques impressionnantes et réduira le prix des soins médicaux. Cette thèse présente le développement de trois dispositifs BioMEMS : (i) un outil chirurgicale doté d'un capteur de force (ii) un prothèse de genou contenant un capteur de force intégré, (iii) une sonde de pression miniaturisé et monté dans un cathéter.

Le premier dispositif est un distracteur chirurgicale doté d'un capteur de force intégré. Cet outil a été développé pour faciliter les arthroplasties du genou. Pendant cette forme d'arthroplastie, le chirurgien doit équilibrer la tension des ligaments et contrôler l'espace entre le fémur et le plateau du tibia. Le capteur permet de vérifier ces valeurs de manière quantitative. En plus, le dispositif peut mesurer la tension des ligaments, qui permettra de mieux comprendre le comportement mécanique de ce joint compliqué. Des capteurs de force flexibles du type "Hall" ont été développés utilisant des procédés de fabrication MEMS. Après leurs calibration et caractérisation dans le distracteur, l'outil était capable de mesurer des distances de distraction avec une précision de 0.1 mm et des forces de distraction avec une précision de 2 N. Cette outil permettra aux chirurgiens de vérifier l'emplacement des prothèses pendant des arthroplasties. Le distracteur a été testé dans des genoux cadavériques. Les valeurs mesurés de la tension des ligaments collatérales latérales et médiales étaient équivalentes à celles de la littérature.

Le deuxième dispositif développé dans le cadre de cette thèse est un capteur de contraintes en polyimide, encore fabriqué utilisant des procédés de fabrication MEMS polymeriques. Le but du développement de ce capteur c'était de pouvoir

l'utiliser dans une prothèse de genou. L'implant a été modélisé par éléments finis pour étudier son comportement mécanique, et pour guider le développement et l'emplacement du capteur. Le capteur comprenait des méandres métalliques recouverts par des lamelles de polyimide et a été monté dans une prothèse de genou. La prothèse a été testée dans un simulateur de mouvement mécanique. Des charges axiales dynamiques et statiques ont été appliquées à la prothèse et démontrent qu'elle est capable de mesurer des forces en excès de 4x le poids humain avec une bonne sensibilité et précision.

Le troisième dispositif développé dans le cadre de cette thèse est une sonde de pression en polyimide et SU-8 intégrée dans un cathéter. Premièrement, une analyse par éléments finis a permis d'évaluer des paramètres critiques de la sonde pour optimiser sa sensibilité. La sonde elle-même a été fabriquée par un procédé de fabrication MEMS. La partie active de la sonde est un méandre métallique qui fonctionne par principe piezoresistive. Le méandre est encapsulé dans une membrane de polyimide et capte la pression relative à une chambre à air. La chambre est formée par un procédé de lamination adapté au SU-8. Des tests de la sonde ont démontré qu'elle est comparable à une sonde en silicone déjà commercialisée. Finalement, le fonctionnement du dispositif a été démontré en mesurant la tension sanguine dans un modèle animal.

**Les mots clés:** MEMS, BioMEMS, Biomedical Devices, Bioengineering, Biomechanics, Implantable sensor, Metal thin-film gauges, Metallic thin films, Micro strain sensor, Microfabricated strain gauges, Microsensors, Polymers, Real-time monitoring, Strain gauge, Strain gauges, Strain measurement, Strain sensors, Thin film metal strain gauges.

# Contents

<b>Acknowledgements</b>	<b>v</b>
<b>Publications</b>	<b>vii</b>
<b>Abstract</b>	<b>ix</b>
<b>Résumé</b>	<b>xi</b>
<b>Contents</b>	<b>xiii</b>
<b>List of Figures</b>	<b>xvi</b>
<b>List of Tables</b>	<b>xx</b>
<b>List of Abbreviations</b>	<b>xxii</b>
<b>1 Introduction</b>	<b>1</b>
1.1 Advances in biomedical microsystems . . . . .	3
1.1.1 Diagnostic microsystems . . . . .	3
1.1.2 Therapeutic microsystems . . . . .	4
1.1.3 Surgical applications . . . . .	5
1.1.4 Implantable devices . . . . .	7
1.2 Motivation and scope of this thesis . . . . .	7
1.3 Organization of this thesis . . . . .	8
1.4 References . . . . .	9
<b>2 State of the Art and Technology</b>	<b>13</b>
2.1 Micro-/Nano-sensors . . . . .	14

2.1.1	Mechanical sensors . . . . .	14
2.2	Previous research in MEMS strain and pressure sensors . . . . .	17
2.2.1	MEMS pressure sensors . . . . .	17
2.2.2	Micromachined strain sensors . . . . .	18
2.2.3	Robotic tactile sensors . . . . .	19
2.2.4	Orthopedic load determination . . . . .	19
2.2.5	MEMS strain and pressure sensors summary . . . . .	22
2.3	Stress/Strain measurements . . . . .	23
2.3.1	Strain gauges . . . . .	25
2.3.2	Measuring force and pressure . . . . .	28
2.3.3	Electronic interfacing - The Wheatstone bridge . . . . .	29
2.4	Release and Detachment . . . . .	33
2.4.1	Anodic dissolution . . . . .	33
2.5	Finite Element Analysis . . . . .	34
2.6	Biocompatibility . . . . .	36
2.7	References . . . . .	37
<b>3</b>	<b>Selected Biomedical Applications</b>	<b>40</b>
3.1	Orthopaedic surgery . . . . .	41
3.1.1	Total knee arthroplasty . . . . .	42
3.2	Cardiac Catheterization . . . . .	46
3.2.1	Pressure monitoring . . . . .	47
3.3	References . . . . .	49
<b>4</b>	<b>Smart Instrumentation for TKA</b>	<b>50</b>
4.1	Introduction . . . . .	51
4.2	Materials and methods . . . . .	52
4.3	Results . . . . .	54
4.3.1	<i>In vitro</i> measurements . . . . .	57
4.4	Discussions . . . . .	58
4.5	Conclusion . . . . .	61
4.6	References . . . . .	62
<b>5</b>	<b>Strain Sensors for Knee Prosthesis</b>	<b>64</b>

5.1	Introduction . . . . .	65
5.2	Finite element analysis . . . . .	66
5.3	Results of finite element analysis . . . . .	68
5.4	Sensor design, fabrication and packaging . . . . .	70
5.5	Experimental setup and results . . . . .	73
5.6	Viscoelasticity and Creep . . . . .	76
5.7	Discussion . . . . .	82
5.8	Conclusion . . . . .	83
5.9	References . . . . .	85
<b>6</b>	<b>Catheter Pressure Sensor</b>	<b>87</b>
6.1	Introduction . . . . .	88
6.2	Finite element analysis of the UHMWPE insert and sensing element placement . . . . .	89
6.3	Results of the finite element analysis . . . . .	92
6.4	Sensor design, fabrication and packaging . . . . .	96
6.5	Experimental setup and procedure . . . . .	101
6.6	Experimental Results . . . . .	102
6.7	<i>in vivo</i> experiment . . . . .	103
6.8	Discussion . . . . .	105
6.9	Conclusion . . . . .	106
6.10	References . . . . .	107
<b>7</b>	<b>Conclusion</b>	<b>109</b>
7.1	Summary of results . . . . .	110
7.2	Future perspectives . . . . .	111
	<b>Appendix A - MEMS/NEMS Technology</b>	<b>114</b>
	Materials growth and deposition . . . . .	115
	Photolithography . . . . .	116
	Etching . . . . .	118
	References . . . . .	120
	<b>Biography and Curriculum Vitae</b>	<b>121</b>

# List of Figures

2.1	NovaSensor medical pressure sensor NPC-100. <a href="http://www.ge-mcs.com/en/pressure-mems.html">http://www.ge-mcs.com/en/pressure-mems.html</a> . . . . .	18
2.2	single-axis, flexible, pressure-sensing array based on organic field-effect transistors for artificial skin applications [20]. . . . .	20
2.3	Knee instrumented prosthesis proposed by Bergmann's group. <a href="http://jwi.charite.de/en/resea">http://jwi.charite.de/en/resea</a>	
2.4	Knee instrumented prosthesis proposed by D'Lima [28]. . . . .	22
2.5	Strain gauge. . . . .	26
2.6	A single leg of a piezoresistive gauge is used to explain the source of the relative resistance change that occurs in response to strain. . .	27
2.7	Block diagram of force/pressure sensor components. . . . .	29
2.8	Basic Wheatstone bridge. . . . .	30
2.9	Four commonly used bridge configurations suitable for sensor applications [31]. . . . .	31
2.10	Instrumentation amplifier schematics. . . . .	32
2.11	Schematic of an electrochemical cell used for the anodic dissolution of aluminum [33]. . . . .	34
3.1	Modern artificial knee comprising the Cr-Co-Mo femoral and tibial components and an Ultra High Molecular Weight (UHMW) Polyethylene (PE) insert, and an illustration of the knee structure before and after TKA ( <i>picture modified from A.D.A.M., Inc. - <a href="http://www.healthcentral.com/rheumatoid-arthritis/9494-146.html">http://www.healthcentral.com/rheumatoid-arthritis/9494-146.html</a></i> ). . . . .	43
3.2	Anatomy of the knee. Reprinted from Tandeter H.B., Shvartzman P., Stevens M.A.. <i>Acute knee injuries: use of decision rules for selective radiograph ordering. Am Fam Physician</i> 1999; 60:2600. . . . .	44
3.3	The six degrees of freedom motion of the knee joint. . . . .	45



4.1	Instrumented distractor prototype capable of continuous and real-time measurements of (A) tibiofemoral forces and (B) flexion-extension gaps. . . . .	53
4.2	Data acquired for the static calibration of the Hall sensor represented by the dots and the third order exponential decay fit to the data represented by the line. The graph presents the distance as a function of the voltage output of the Hall sensor. Error bars are plotted, however they are not visible because it is within the size of the black dots. . . . .	55
4.3	Data acquired for the calibration of the strain sensors to transduce the force represented by the star points and the correspondent linear regression to the data. The curve presents the Force as a function of the output of the Wheatstone bridge. Error bars are plotted, however they are not visible because it is within the size of the star points. . .	56
4.4	Control experiment with a spring attached to the tip of the distractor. The graph shows the force as a function of the distance. . . . .	57
4.5	Experiment for determining the ligament stiffness which consists of recording the force and distance in a series of consecutive loading and unloading of the distractor. The graph presents the measured Forces and distances as a function of the time. . . . .	58
4.6	Results of two <i>ex vivo</i> experiment for determining MCL stiffness. The graph presents the Force as a function of the distance. The stiffness of the ligament can be estimated by the slope of a linear regression fitting the acquired data. . . . .	59
5.1	Components of the CAD model comprising the femoral component (FC), the UHMWPE insert, the tibial component (TC) and the guide pin, and a UHMWPE insert cross-section depicting the location of the strain sensors. . . . .	67
5.2	Simplified 3D CAD model used in the FEA. . . . .	68
5.3	Evolution of the x-component strain, in the xy-plane at 6 mm from the FC/UHMWPE bearing surface, for different applied loads. . . .	69

5.4	Evolution of the x-component strain at the line of intersection between the xy- and the xz-planes, along the UHMWPE width, for different applied loads. . . . .	70
5.5	Cross section view of the fabrication process. . . . .	71
5.6	Polyimide-metal-polyimide micro-machined structure. . . . .	72
5.7	(A) A cross-sectioned UHMWPE insert with the strain sensors positioned for final assembly and (B) the complete packaged device re-joined and sealed using a biocompatible epoxy glue. . . . .	73
5.8	Simulated x-component strain and measured strain as a functions of applied loads. . . . .	75
5.9	Series of slow (A) and fast (B) dynamic loading/unloading and respective sensor's output as a function of time. . . . .	75
5.10	Most common viscoelastic models employed to predict material's response under different loading conditions [16]. . . . .	77
5.11	Sensor's response over time for several constant forces applied. . . . .	78
5.12	Sensor's response over time when the applied constant forces are released. . . . .	79
5.13	Evolution of the fitting parameters "a" and "b", for both creep and stress relaxation, as a function of the force. . . . .	80
5.14	Experimental creep curves for different loading levels versus the logarithm of time. . . . .	81
6.1	CAD model comprising the polyimide membrane, the platinum as piezoresistive material and the SU-8 enclosed chamber (cross-section along the device width). . . . .	90
6.2	x-component of the membrane stress along the device width as a function of the membrane thickness, in the transverse plane situated at the top of the PI membrane. . . . .	93
6.3	PI membrane deflection with the applied pressure, in the transverse plane situated at the top of the PI membrane. (a) Width cross-section and (b) Length cross-section. . . . .	94
6.4	x-component of the membrane strain with the applied pressure, in the transverse plane situated at the top of the PI membrane and along the device width. 2D model without platinum trace. . . . .	95

6.5	x-component of the membrane (a) strain and (b) stress with the applied pressure, in the transverse plane situated at 2 $\mu\text{m}$ from the bottom of the PI membrane and along the device width. 2D model including the defined platinum line embedded into the polyimide membrane. . . . .	97
6.6	Cross-section view of the fabrication process. . . . .	98
6.7	Optical images, respectively top-view and tilted-view, of a released device comprising the enclosed SU-8 chamber, the active and passive strain gauges, as well as the suspended PI membrane. . . . .	100
6.8	Assembled polyimide/SU-8 catheter-tip MEMS gauge pressure sensor in comparison with a commercial Millar Mikro-Cath <sup>TM</sup> disposable pressure catheter. . . . .	100
6.9	Schematic diagram of the experimental setup . . . . .	101
6.10	Polyimide/SU-8 gauge pressure sensor calibration curve showing reference pressure as a function of the voltage output of the gauge pressure sensor and corresponding linear regression fitting the data. . . . .	102
6.11	Polyimide/SU-8 gauge pressure sensor response to changes in ambient temperature as a function of the voltage output of the gauge pressure sensor and corresponding linear regression fitting to the data. . . . .	103
6.12	Response of the reference pressure transducer and the polyimide/SU-8 gauge pressure sensor as a function of the time for pressure variations at a frequency of $\sim 7$ Hz . . . . .	104
6.13	Trace of carotid arterial blood pressure and heart rate in a male C57BL/6J mouse during inhalation of 0.5-1% isoflurane. . . . .	105
1	General concept of the sputtering process. . . . .	116
2	General steps of the spin coating process. . . . .	117
3	General photolithography process [3]. . . . .	118

# List of Tables

- 4.1 Summary of the results from the two *ex vivo* experiments to determine the ligament stiffness and previous reported MCL and LCL stiffness [8]. . . . . 59
- 6.1 Material properties used in the FEA. . . . . 91



# List of Abbreviations

<b><math>\mu</math>TAS</b>	Micro Total Analysis Systems
<b>ACL</b>	Anterior Cruciate Ligament
<b>ADC</b>	Analog to Digital Converter
<b>BioMEMS</b>	Biological-Microelectromechanical Systems
<b>BP</b>	Blood Pressure
<b>CAD</b>	Computer Assisted Design
<b>CVD</b>	Chemical Vapor Deposition
<b>DOF</b>	Degrees of Freedom
<b>ECG</b>	Electrocardiography
<b>FC</b>	Femoral Component
<b>FEA</b>	Finite Element Analysis
<b>LCL</b>	Lateral Collateral Ligament
<b>LoC</b>	Lab-on-Chip
<b>MCL</b>	Medial Collateral Ligament
<b>MEMS</b>	Microelectromechanical Systems
<b>MOS</b>	Metal-Oxide-Semiconductor
<b>NEMS</b>	Nanoelectromechanical Systems
<b>PE</b>	Polyethylene
<b>PI</b>	Polyimide
<b>PM</b>	Polyimide Micro-machining
<b>PCL</b>	Posterior Cruciate Ligament
<b>PVD</b>	Physical Vapor Deposition
<b>PZT</b>	Lead Zirconate Titanate
<b>RF</b>	Radio Frequency
<b>TC</b>	Tibial Component
<b>TKA</b>	Total Knee Arthroplasty
<b>UHMW</b>	Ultra High Molecular Weight
<b>UHMWPE</b>	Ultra High Molecular Weight Polyethylene
<b>UV</b>	Ultraviolet
<b>YP</b>	Yield Point

# CHAPTER 1

## Introduction

*If you knew what you were doing  
it wouldn't be called research.  
- Albert Einstein*

The roots of microelectromechanical systems (MEMS) technology go back to the early development of process techniques for microelectronics. The origins of what we know as MEMS technology can be traced back to 1954 when, for the first time, certain stress-sensitive effects in silicon and germanium was characterized as piezoresistance [1]. In the 1970s, the advancement of semiconductor microelectronics processing allowed the formation of three dimensional silicon geometries [2]. In the 1980s, the Metal-Oxide-Semiconductor (MOS) process, that uses the silicon dioxide as a sacrificial layer material [3], led to the development of surface micromachined devices such as electrostatically actuated motors [4], and interdigitated finger capacitive sensors and resonators [5]. In the 1990s, many commercially successful MEMS products began to appear in the market and substantial sub-domains of MEMS appeared [6], including optical MEMS [7], RF MEMS [8], MEMS for harsh environments [9], power MEMS [10], NEMS [11] and BioMEMS [12, 13]. Over the last 40 years, such evolution in the fabrication techniques at small scale has stepped up from being one of the several segments of microelectronics and has emerged as a separate global industry, taking advantage of flourishing semiconductor technology. Nowadays, MEMS market is on path to reach \$20B in 2016, with major classes of devices being: inertial sensors, microfluidics, pressure sensors and inkjet heads.

The last decade has been an exciting period for people working in the fields of micro and nanosystems technology and the keen explosive growth of MEMS has introduced a variety of promising products in major disciplines [14], from microelectronics [15] and micro-fabrication technology [16] to life sciences [17]. In recent years, MEMS applications in biology and biomedicine have rapid evolved and their combination created a common term of "biological-microelectromechanical systems" (BioMEMS); the synergy between these topics yielded completely new devices with numerous applications in biochemistry [18], biology [19] and medicine [20]. The healthcare implications expected after the successful development of BioMEMS technology is enormous, and include early disease diagnostics, more accurate assessment on risk conditions, less physical trauma, short recovery times, and more accessible healthcare monitoring and delivery at a lower total cost [21].



Analytical and therapeutic micro/nanosystems will be mandatory for medical doctors and biologists in the long run, in order to obtain insight into morphology and the interactive processes of the living system. BioMEMS in combination with low-power integrated circuits and biomaterials has the potential to provide many of the future tools for life science and in particular miniaturized therapeutic and diagnostic devices, less invasive, more precise and suitable even for long-term implantation. Micro and nanofabrication techniques also offer different types of advantages for implantable devices, such as higher surface-area-to-volume ratio, reduced size, enhanced geometrical control during manufacturing, batch processing, high throughput and relatively easy integration with conventional electronics [22].

## **1.1 Advances in biomedical microsystems**

### **1.1.1 Diagnostic microsystems**

Diagnostics has been subjected to continuous improvement due to the progress of science and technology over the last years. A lot of effort is put into research to develop personalized diagnostic tools that are highly sensitive and capable of early detection of diseases. Some devices are already available in consumer friendly packages such as the home pregnancy tests and hand held glucose monitoring systems, introducing substantial diagnostic advancement [13].

#### **Point of care diagnostics**

The scaling of diagnostic tools was made a reality by the engineering advances in surface and material science. MEMS use several of the techniques employed in the microelectronic industry in order to build single electronic chips that are able to characterize samples and run an entire diagnostic operation. Such systems are also known as  $\mu$ TAS (micro Total Analysis Systems) or LoC (Lab-on-Chip) devices. For the determination of a specific type of disease, multiplexing of tests can be required and each component can have different MEMS stages such as cell separation [23], cell lysis [24] and sensing elements [25]. The potential application of such devices in blood analysis and drug screening

systems can revolutionize our healthcare system [26].

### **Other MEMS based diagnostics**

Other remarkable advances of BioMEMS include the development of devices for measuring physiological parameters such as temperature, pressure and pulse-rate. MEMS techniques have been used to develop devices for applications such as intracranial pressure monitoring in case of head trauma [27], intraocular pressure evaluation for glaucoma [28], blood pressure and heart rate monitoring for cardiovascular assessment [29]. More exotic MEMS applications include sensors embedded into smart textiles or wearable cardiovascular monitoring systems, such as wearable electrocardiography (ECG) foils [30].

## **1.1.2 Therapeutic microsystems**

### **Drug Discovery**

Drug discovery process is organized into different phases starting with the identification of drug targets, a process known as target identification, wherein the biomolecules that play significant role in diseases are identified. Next, from a library of a large number of chemical compounds, the ones that have the potential to treat the disease by interacting with the drug targets in a desirable way are identified. These compounds undergo optimization to become a possible clinical candidate followed by a testing phase to ensure that it is safe to be administered to the patients.

Microarrays, created using photolithographic method, have extended the capability of target identification, reducing its development time and cost and thus resulting in enhanced throughput [31]. The lead identification and optimization process (identification and optimization of chemical compounds that can interact with the target molecules to produce drug like effect) was revolutionized with the creation of microchip patch clamp [32]. Also, laboratory tests conducted on the investigational drug to see its effects both in living organism (*in vivo*) and cells (*in vitro*) was improved with the creation of microfluidic structures mimicking the actual *in vivo* environment [33].

## **Drug Delivery**

A variety of devices and components has been developed using MEMS techniques that are able to release drugs, e.g. of different dosages. One of the first proposed methods for drug delivery was throughout microneedles, e.g. hollow microneedles have been fabricated and used to flow drug solutions through the skin [34]. Also, for an implantable drug delivery system, a drug reservoir or supply is required. This drug reservoir has to protect the drug from the body until needed and also allow delivery in a controlled dosage. MEMS fabrication techniques have been explored to form reservoirs with good biocompatibility [35] and despite research on microfabricated drug delivery devices has rapidly expanded, much research still has to be done to optimize the size, shape, number, volume, and surface characteristics of the drug delivery systems [36].

### **1.1.3 Surgical applications**

#### **Minimally invasive surgery**

Medical procedures are evolving into the use of minimally invasive methods and new assessment tools to reduce trauma from surgery. The main advantages are to decrease post-operative pain and improve recovery time. MEMS technology has played an important role in the evolution of these minimally invasive procedures and assessment tools, by allowing surgical devices downscale to the size of individual cells, thus providing access to areas of the body previously inaccessible. With the aid of microfabrication techniques researchers have developed tools such as micro-grippers, micro-tweezers, micro-forceps and micro-scissors that can now explore previously inaccessible areas with high spatial resolution [37, 38].

#### **Tactile sensing**

Following the trends of minimally invasive surgeries, a major challenge faced by surgeons is the lack of sense of touch. To overcome this limitation microfabricated devices capable of restoring and enhancing tactile sensation are being developed [39]. Tactile sensors typically consisting of piezoelectric or

piezoresistive elements embedded at critical locations along the structure of a mechanical device have been developed to provide three-dimensional mapping of the mechanical deformations in the device. In addition to these sensing mechanisms, various other methods have also been investigated. MEMS sensors for monitoring mechanical properties of tissues, such as the elastic modulus, have also been developed [40].

### **MEMS Cutting tools**

The miniaturization enable the utilization of ultra small cutting tools to make smaller incision and, therefore, less bleeding. The development of these sharper devices can be made by etching silicon precisely along its crystal planes [41]. Also, the utilization of vibratory mechanism for cutting tissues have been demonstrated [42]. Some of the sensing mechanisms added to this devices are pressure sensors, temperature sensors as well as impedance sensors for measuring tissue impedance.

### **Endoscopy**

The advancement of BioMEMS allowed the reduction of endoscopy systems to fit into a drug capsule, permitting the monitoring of the gastrointestinal tract [43]. These capsules consist of image sensors, LED illumination devices, telemetry units for signal transmission and control electronics, all combined into micro-devices by microfabrication techniques. Still, a limitation of these capsule endoscopes is their dependency on the peristaltic waves, therefore, their active interaction capabilities are very restricted. To overcome such limitations, researchers are looking into the possibility of making capsular endoscopy active through the use of micro robots [44]. The field of micro robotics for locomotion inside the human body is yet another interesting for the application of MEMS in biomedical technology.

### **1.1.4 Implantable devices**

#### **Neuro prosthesis**

Neural implants are technological devices that allow the connection between the brain and a computational system. Its main functions are to record brain activity and perform electrical stimulation to circumvent damaged or disabled nervous system attempting to restore functions. The neural probe, from a biological standpoint is considered as a foreign body, therefore, biocompatibility issues have to be taken into consideration. For this reason, polymers such as polyimide have also been looked into for developing neural probes [45]. One of the focus of current research in MEMS technology is to miniaturize such devices for the purpose of stimulating or recording from a neural population with reduced potential damage to the tissues. Also, miniaturization of neural implants promote the integration with circuitry for amplification, multiplexing, spike detection, and wireless transmission of power and bidirectional data that facilitates prosthetic devices for many debilitating neurological disorders [46].

#### **Retinal prosthesis**

Certain diseases that cause blindness have the potential of being managed using retinal prosthesis. MEMS technology provides means for developing these prosthetic devices since the stimulation of the ganglion cells produce visual sensations in the brain. The main function of retinal implant is that it should be capable of detecting light and transform this information into artificial electrical stimulus, thus mimicking the damaged photoreceptor cells. Several approaches such as epiretinal, subretinal, optic nerve and cortical visual stimulations have been proposed, and examples of such prosthesis are the flexible electrodes based on polymers such as parylene and polyimide [47].

## **1.2 Motivation and scope of this thesis**

Overall, MEMS technology has exerted a significant impact on sensing practices as more complex and sophisticated devices are developed in response to emerging needs in a wide range of industries. The introduction of such microsystems

in the biomedical and health sciences substantially contributed to significant advancements in biomedical tools while reducing healthcare costs.

The scope of this research is to investigate, design, fabricate, characterize and test novel microsystems (combining micro/nanofabrication technologies, microelectronics and biomaterials) for the assessment of medical devices and implants. This thesis will focus in three applications of BioMEMS: (i) smart medical instrumentation, (ii) artificial knee implants and (iii) catheter pressure sensors. Despite the broad range of applications, the key common element in all these devices is a MEMS strain gauge sensor fabricated using polyimide micro-machining (PM) process.

### 1.3 Organization of this thesis

In **Chapter 2** the state of the art and MEMS technology of the devices employed in this thesis are described, while in **Chapter 3** the selected biomedical applications for the developed BioMEMS are presented. Next chapters will be dedicated to present individually each of the developed devices. In **Chapter 4** we present a smart medical instrumentation to be used in total knee arthroplasty in order to improve surgical outcome without changing surgical procedures or impose to surgeons new surgical techniques. In **Chapter 5** we demonstrate a polyimide-based MEMS strain-sensing device for monitoring knee implants, and in **Chapter 6** a polyimide/SU-8 catheter-tip MEMS gauge pressure sensor is presented. This thesis is concluded in **Chapter 7** with a discussion about future steps and potential of this technology for other applications.

## 1.4 References

- [1] C. S. Smith, "Piezoresistance effect in germanium and silicon," *Physical Review*, vol. 94, pp. 42–49, Apr 1954.
- [2] K. E. Bean, "Anisotropic etching of silicon," *IEEE Transactions on Electron Devices*, vol. 25, no. 10, pp. 1185–1193, 1978.
- [3] R. T. Howe and R. S. Muller, "Polycrystalline silicon micromechanical beams," *Journal of the Electrochemical Society*, vol. 130, pp. 1420–1423, June 1983.
- [4] L. S. Fan, Y. C. Tai, and R. S. Muller, "Integrated movable micromechanical structures for sensors and actuators," *IEEE Transactions on Electron Devices*, vol. 35, no. 6, pp. 724–730, 1988.
- [5] W. C. Tang, M. G. Lim, and R. T. Howe, "Electrostatic comb drive levitation and control method," *Journal of Microelectromechanical Systems*, vol. 1, no. 4, pp. 170–178, 1992.
- [6] C. Liu, "Recent developments in polymer mems," *Advanced Materials*, pp. 3783–3790, Nov 2007.
- [7] W. Noell, P. A. Clerc, L. Dellmann, B. Guldimann, H. P. Herzig, O. Manzardo, C. R. Marxer, K. J. Weible, R. Dandliker, and N. de Rooij, "Applications of soi-based optical mems," *IEEE Journal of Selected Topics in Quantum Electronics*, vol. 8, no. 1, pp. 148–154, 2002.
- [8] J. J. Yao, "Rf mems from a device perspective," *Journal of Micromechanics and Microengineering*, vol. 10, p. R9, 2000.
- [9] C.-H. Wu, C. Zorman, and M. Mehregany, "Fabrication and testing of bulk micromachined silicon carbide piezoresistive pressure sensors for high temperature applications," *IEEE Sensors Journal*, vol. 6, pp. 316–324, Apr 2006.
- [10] A. Pattekar and M. Kothare, "A microreactor for hydrogen production in micro fuel cell applications," *Journal of Microelectromechanical Systems*, vol. 13, pp. 7–18, Feb 2004.
- [11] H. G. Craighead, "Nanoelectromechanical systems," *Science*, vol. 290, pp. 1532–1535, Nov 2000.
- [12] R. Bashir, "Biomems: state-of-the-art in detection, opportunities and prospects," *Advanced Drug Delivery Reviews*, pp. 1565–1586, Sep 2004.

- [13] T. James and M. Mannoor, "Biomems - advancing the frontiers of medicine," *Sensors*, pp. 6077–6107, Sep 2008.
- [14] J. Gardner, V. Varadan, and O. Awadelkarim, "Microsensors, MEMS, and Smart Devices," Dec. 2001.
- [15] S. Lyshevski, *MEMS and NEMS: systems, devices, and structures*. 2002.
- [16] C. Leondes, *MEMS/NEMS: handbook techniques and applications*. 2006.
- [17] W. Wang and S. A. E. Soper, eds., *Bio-MEMS: technologies and applications*. CRC Press, 1 ed., Dec 2007.
- [18] P. Chu and X. Liu, *Biomaterials fabrication and processing handbook*. CRC Press, 2008.
- [19] W. Pompe, "Nanodevices for the Life Sciences.," *Acta Crystallographica Section F: Structural Biology and Crystallization Communications*, vol. 63, p. 635, July 2007.
- [20] M. Kutz, *Biomedical Engineering & Design Handbook, Volumes I and II*. McGraw-Hill Professional, 2 ed., Aug. 2009.
- [21] A. Offenhäusser, K. Jaenich, and R. Rinaldi, *Nanobioelectronics: For Electronics, Biology, and Medicine*. Springer Verlag, 2009.
- [22] J. Korvink and O. Paul, *MEMS: a practical guide to design, analysis, and applications*. 2006.
- [23] K. Cheung, S. Gawad, and P. Renaud, "Impedance spectroscopy flow cytometry: on-chip label-free cell differentiation.," *Cytometry. Part A : the Journal of the International Society for Analytical Cytology*, vol. 65, pp. 124–32, Jun 2005.
- [24] G. Mernier, W. Hasenkamp, N. Piacentini, and P. Renaud, "Multiple-frequency impedance measurements in continuous flow for automated evaluation of yeast cell lysis," *Sensors and Actuators B: Chemical*, Nov 2010.
- [25] G. Mernier, W. Hasenkamp, N. Piacentini, and P. Renaud, "Multiple-frequency impedance measurements in continuous flow for the evaluation of electrical lysis of yeast cells," *Procedia Engineering*, vol. 5, pp. 37–40, Jan 2010.
- [26] P. Abgrall, "Lab-on-chip technologies: making a microfluidic network and coupling it into a complete microsystem - a review," *Journal of Micromechanics and Microengineering*, pp. R15–R49, May 2007.



- [27] C. Li, P.-M. Wu, L. a. Shutter, and R. K. Narayan, "Dual-mode operation of flexible piezoelectric polymer diaphragm for intracranial pressure measurement," *Applied Physics Letters*, vol. 96, no. 5, p. 053502, 2010.
- [28] M. Leonardi, P. Leuenberger, D. Bertrand, A. Bertsch, and P. Renaud, "First steps toward noninvasive intraocular pressure monitoring with a sensing contact lens.," *Investigative ophthalmology & visual science*, vol. 45, pp. 3113–3117, Sept. 2004.
- [29] A. Grayson, R. Shawgo, A. Johnson, N. Flynn, Y. Li, M. Cima, and R. Langer, "A BioMEMS review: MEMS technology for physiologically integrated devices," *Proceedings of the IEEE*, vol. 92, no. 1, pp. 6–21, 2004.
- [30] M. O. Schurr, S. Schostek, C.-N. Ho, F. Rieber, and A. Menciassi, "Microtechnologies in medicine: An overview," *Minimally Invasive Therapy Allied Technologies*, vol. 16, pp. 76–86, Jan 2007.
- [31] M. J. Heller, "An active microelectronics device for multiplex dna analysis," *Engineering in Medicine and Biology Magazine, IEEE*, vol. 15, no. 2, pp. 100–104, 1996.
- [32] A. Brüggemann, S. Stoelzle, M. George, J. C. Behrends, and N. Fertig, "Microchip technology for automated and parallel patch-clamp recording," *Small*, vol. 2, pp. 840–846, Jul 2006.
- [33] A. Tourovskaia, X. Figueroa-Masot, and A. Folch, "Differentiation-on-a-chip: A microfluidic platform for long-term cell culture studies," *Lab on a Chip*, vol. 5, no. 1, p. 14, 2005.
- [34] J. W. Lee, J. H. Park, and M. R. Prausnitz, "Dissolving microneedles for transdermal drug delivery," *Biomaterials*, vol. 29, no. 13, pp. 2113–2124, 2008.
- [35] G. Voskerician, M. S. Shive, R. S. Shawgo, H. Recum, J. M. Anderson, M. J. Cima, and R. Langer, "Biocompatibility and biofouling of mems drug delivery devices," *Biomaterials*, vol. 24, no. 11, pp. 1959–1967, 2003.
- [36] S. Sharma, A. J. Nijdam, P. M. Sinha, R. J. Walczak, X. Liu, M. M.-C. Cheng, and M. Ferrari, "Controlled-release microchips," *Expert Opinion on Drug Delivery*, vol. 3, pp. 379–394, May 2006.
- [37] R. B. Bhisitkul, "Development of microelectromechanical systems (mems) forceps for intraocular surgery," *British Journal of Ophthalmology*, vol. 89, pp. 1586–1588, Dec 2005.
- [38] W. C. Chang and D. W. Sretavan, "Microtechnology in medicine: The emergence of surgical microdevices," *Clinical Neurosurgery*, vol. 54, p. 137, 2007.

- [39] M. Hosseini, S. Najarian, S. Motaghinasab, and J. Dargahi, "Detection of tumours using a computational tactile sensing approach," *The International Journal of Medical Robotics and Computer Assisted Surgery*, vol. 2, pp. 333–340, Dec 2006.
- [40] M. H. Lee and H. R. Nicholls, "Review article tactile sensing for mechatronics - a state of the art survey," *Mechatronics*, vol. 9, no. 1, pp. 1–31, 1999.
- [41] D. W. Sretavan, W. Chang, E. Hawkes, C. Keller, and M. Klot, "Microscale surgery on single axons," *Neurosurgery*, pp. 635–646, Oct 2005.
- [42] A. Lal and R. M. White, "Silicon microfabricated horns for power ultrasonics," *Sensors and Actuators A: Physical*, vol. 54, no. 1-3, pp. 542–546, 1996.
- [43] F. Gong, P. Swain, and T. Mills, "Wireless endoscopy," *Gastrointestinal Endoscopy*, vol. 51, no. 6, pp. 725–729, 2000.
- [44] A. Moglia, A. Menciassi, M. O. Schurr, and P. Dario, "Wireless capsule endoscopy: from diagnostic devices to multipurpose robotic systems," *Biomedical Microdevices*, vol. 9, pp. 235–243, Dec 2006.
- [45] S. Metz, A. Bertsch, D. Bertrand, and P. Renaud, "Flexible polyimide probes with microelectrodes and embedded microfluidic channels for simultaneous drug delivery and multi-channel monitoring of bioelectric activity," *Biosensors and Bioelectronics*, vol. 19, no. 10, pp. 1309–1318, 2004.
- [46] K. D. Wise, "Integrated sensors, mems, and microsystems: Reflections on a fantastic voyage," *Sensors and Actuators A: Physical*, vol. 136, no. 1, pp. 39–50, 2007.
- [47] D. C. Rodger, A. J. Fong, W. Li, H. Ameri, A. K. Ahuja, C. Gutierrez, I. Lavrov, H. Zhong, P. R. Menon, E. Meng, and et al., "Flexible parylene-based multielectrode array technology for high-density neural stimulation and recording," *Sensors and Actuators B: Chemical*, vol. 132, no. 2, pp. 449–460, 2008.

# CHAPTER 2

## State of the Art and Technology

*The only true wisdom is knowing  
that you know nothing.  
- Socrates*

## 2.1 Micro-/Nano-sensors

In abstract terms, a transducer is a device that transforms one form of energy (e.g. a physical variable of interest) into another (e.g. a quantity suitable for recording). The deformation of a piezoelectric crystal under an applied electric field is one example of how this occurs. Sensors are special types of transducer that convert one physical or chemical quantity into an electrical one for processing by the microsystem. On the other hand, an actuator is a device that converts an electrical quantity into a physical or chemical one [1].

One typical element in a MEMS/NEMS device is the sensor, which has the function of converting the physical variable input into a signal variable output. Signal variables can be manipulated in an electrical or mechanical circuit and be transmitted to an output or recording device that can be remote from the sensor. In electrical circuits, voltage is a common signal variable. In mechanical systems, displacement or force are commonly used as signal variables [2]. If the signal output from the sensor is small, it is sometimes necessary to amplify the output signal to be transmitted or recorded, depending on the particular measurement application. In the case a computer-based data acquisition or communications system is used (display and/or store the data) the sensor has to provide a digital signal output. If the sensor does not inherently provide a digital output, then the analog output of the sensor is converted by an analog to digital converter (ADC). In principle, a sensor can be regarded as a black box that relates the input signal with the output signal. This relationship is made throughout a transfer function that establishes the dependence between the output electrical signal and the input variable [3].

### 2.1.1 Mechanical sensors

Generally there exist two different types of mechanical sensors. The first uses physical mechanisms to directly sense the parameter of interest (e.g., distance and strain). The second uses microstructures to enable the mechanical sensors to detect parameters of interest (e.g., acceleration) that cannot be measured directly with the first type of sensor [1]. The most relevant transduction mechanisms in mechanical sensors include the following effects: piezoresistivity,

piezoelectricity, capacitance, magnetic and inductive sensing, and resonant techniques.

### **Piezoresistive sensor**

Piezoresistivity is an effect exhibited by various materials that exhibit a change in resistivity due to a mechanical stress. The effect was first discovered by Lord Kelvin in 1856, who noted that the resistance of copper and iron wires increased when mechanically stretched. Despite this early discovery of the piezoresistive effect its first applications only came out about 70 years later, in the 1930s, with the invention of the strain gauge [4]. These devices (strain gauges) were initially made from a thin metal foil that could be glued onto surfaces, and just afterwards metal wires started to be used.

### **Piezoelectric sensors**

Certain classes of materials exhibit the property of producing an electric charge on its surface when deformed (direct effect). They also deform in response to an externally applied electric field (inverse effect). This unusual effect make piezoelectric materials to be used both as sensor and actuator. It was first discovered in quartz by Jacques and Pierre Curie in 1880. The origin of piezoelectricity phenomenon arises due to the charge asymmetry within the crystal structure of the materials. Common piezoelectric materials used for microengineered devices include zinc oxide and PZT ( $\text{PbZrTiO}_3$  - lead zirconate titanate), which can be deposited on microstructures and patterned.

### **Capacitive sensors**

The conceptual physical structures of capacitive sensors are relatively simple. The simplest capacitive sensor consists of two parallel plates separated by a gap and its output capacitance is a function of the area of the conductors and the distance (gap) between them. More elaborate structures, such as interdigitated capacitors, are also used, and the effects of the fringing fields have to be considered during the design of such sensors. The membrane-type devices are often used as the basis for pressure sensors and microphones. Capacitive techniques are less noisy than those based on piezoresistance since

thermal (Johnson) noise is not present. However, for micromachined devices the inherent small capacitance (in the range of femto- to attofarads), and the additional noise from the interface electronic circuits, make its usage more costly than resistance-based system.

### **Magnetic and inductive sensors**

In magnetic or inductive sensors the measurement system is composed of an emitter and a receiver. The emitter generates a magnetic field and is usually mounted on a movable part of the sensing device while the receiver is placed on a fixed reference part and measures the variation of the magnetic field induced by the emitter displacement. In magnetic sensors the emitter is a permanent magnet and the receiver is a magnetic field detector based on the Hall effect. The Hall effect is the production of a potential difference (the Hall voltage) across an electrical conductor, transverse to an electric current in the conductor when a magnetic field is applied perpendicularly to the current. This effect was discovered by Edwin Hall in 1879. In its simplest form, when an electrical current traverses a metallic plate, submerged in a magnetic field, the electrons going through the plate experience a Lorentz force perpendicular to the current direction. Due to this effect the voltage that appears on the conductor border has its amplitude varying proportionally to that of the magnetic field crossing the plate. On the other hand, in inductive sensors the emitter is a coil powered by an alternating current, thus generating an oscillating magnetic field. The receiver is also a coil, into which the emitted magnetic field induces a current. The amplitude of the induced current varies with the magnetic field amplitude [5].

### **Resonant sensors**

A resonator is a mechanical structure designed to vibrate at a particular resonant frequency. A resonant sensor is designed such that its natural frequency is a function of the physical variable of interest. This physical variable typically alters the stiffness, mass, or shape of the resonator, hence causing a change in its resonant frequency. Resonators can be fabricated in micron-sized dimensions using various micromachining processes and having very stable resonant

frequencies [6]. Due to its stability some resonators can be used as a time base element or as the sensing element in a resonant sensor. In a well-designed resonator the resolution can easily reach 1 part in  $10^8$ , which is at least three orders of magnitude higher than a piezoresistive and capacitive sensor. However, the fabrication of such devices is more complex and the requirements for packaging such devices are extremely demanding.

## **2.2 Previous research in MEMS strain and pressure sensors**

Previous work in the area of sensors for the measurement of strain and pressure has used mostly capacitive and piezoresistive sensors, and less often optical and resonant devices. A lot of research has been done in the past, for example, on the development of fluid shear stress sensors which were mainly used in aerodynamics for flow measurements [7] and in composite materials to determine the stress [8, 9]. More recently, there has been a growing interest on measuring the pressure exerted by the limbs and prosthesis. [10]. This section will provide an overview on MEMS strain and pressure sensors.

### **2.2.1 MEMS pressure sensors**

The literature contains several references to the application of MEMS for the measurement of strain and pressure. Much of the early development on bulk micromachined silicon, diaphragm-based, sensors was performed at Motorola [11]. These were silicon diaphragm-based MEMS pressure sensors for the sensing of gas and liquid pressures. These devices consist of single sensors and are primarily designed to measure the air pressure in automobile tires or the pressure in a compressed gas cylinder or lines. They may have piezoresistive strain gauges implanted in the membranes or measure the capacitance between the diaphragm and the surface below. Recently, MEMS pressure sensors are approaching maturity for some applications in automotive industry and aerospace [12, 13].

Pressure is one of the important parameters to diagnose many diseases in body.

Since much of our body is a complex system which consist of pumps, valves, vessels and interconnects, pressure sensors can be used to measure blood pressure, bladder pressure and cerebral spinal fluids. With help of MEMS or NEMS technology the size of pressure sensor inserted in the body can be made small and disposable. A commercially successful low cost disposable medical pressure sensor was developed by General Electric (NovaSensor medical pressure sensor NPC-100 - Fig. 2.1). In these sensors, generally silicon micromachined sensing element can be used to complete the industry requirements such as sensitivity and linearity. Recently, MEMS based absolute micro pressure sensor, functioning on the principle of piezoresistive effect, has been designed and fabricated [14], which could be used as a blood pressure sensor.

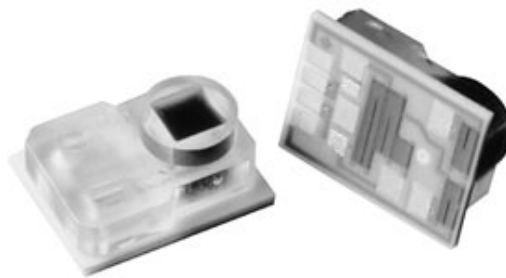


Figure 2.1: NovaSensor medical pressure sensor NPC-100. <http://www.gemcs.com/en/pressure-mems.html>.

### 2.2.2 Micromachined strain sensors

Microfabricated systems consisting of layers of thin films of various materials deposited under a variety of thermal conditions are subject to distortion due to coefficient of thermal expansion (CTE) mismatch effects. Residual strain existing in the thin films affects the device performances and is one of the most common properties to be characterized. Damage to microdevices may be caused by unacceptably high residual strains by buckling or warping, or other damage. A measurement device to monitor and characterize residual strain during microfabrication is crucial for sensitive applications. These sensors decrease



required die size and may simplify integration with electronics, however at the cost of reduced sensitivity and reproducibility of mechanical properties [15]. A vernier mechanical amplifier approach has been developed by Lin and Pisano from University of California at Berkeley whereby surface residual stress causes movement in a surface micromachined lever [16]. More recently, this concept for measuring chip surface strain in air was extended by the Berkeley researchers using a double ended tuning fork resonant technique capable of nanostrain resolution [17].

### 2.2.3 Robotic tactile sensors

Researchers in the field of robotics have been interested in developing tactile sensor arrays to determine the forces exerted by robotic grippers, tele-operational manipulators, and haptic interfaces. A group of researchers at Stanford University led by Prof. Gregory Kovacs has developed a tactile sensing array for such an application. This array was fabricated on a silicon wafer using CMOS-compatible fabrication processes, uses four piezoelectric sensors per array element, and includes digital control circuitry fabricated in conjunction with the sensor elements [18]. Researchers at the University of Illinois have developed a polyimide-based, flexible sensor array with nickel-chrome resistors capable of measuring normal displacements [19]. Recently, the University of Tokyo has developed a single-axis, flexible, pressure-sensing array based on organic field-effect transistors for artificial skin applications [20]. A picture of such device is presented in Fig. 2.2 An extensive review on the subject can be found in [21].

### 2.2.4 Orthopedic load determination

The ability to determine *in vivo* forces is necessary in order to predict the performance of new orthopedic implant designs, to determine the effects of orthopedic procedures and surgical parameters, and to understand the biomechanics of the limbs. Studies employing instrumented prosthetics and incorporating data telemetry produce the most direct method of determining implant loads. In the past, these devices were expensive and not approved for use in a wide range

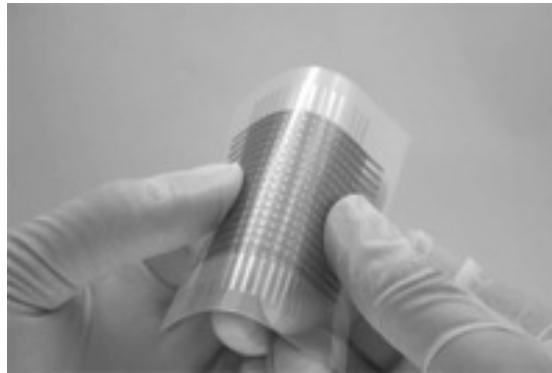


Figure 2.2: single-axis, flexible, pressure-sensing array based on organic field-effect transistors for artificial skin applications [20].

of subjects [22]. The first use of telemetry to measure hip forces measured peak loads of 2.56 times body weight during gait, but published data is not extensive [23]. Another pioneer of *in vivo* force sensing using telemetry was German researcher Georg Bergmann. Bergmann has published research on hip, spine and knee loadings using strain gauges. A picture of a knee instrumented prosthesis is shown in Fig. 2.3. The instrumented prosthesis is powered using an inductive coil, and the measurements are sent to a personal computer using an RF telemetry system [24]. The power for this system is transmitted inside the limb using an inductive coil worn around the patient's leg during testing. Similar research has been performed by Davy and Kotzar where they implanted a hip prosthesis in two patients that measured peak loads of 2.1 - 2.8 times body weight during gait and a maximum value of 5.5 times body weight during periods of instability during single leg stance [25].

The earliest work on measuring femoral loads was an extrapolation of the work performed on hip implants using massive femoral implants. Bassey, Littlewood, and Taylor instrumented a titanium implant which replaced the hip and the proximal half of the tibia. This implant used four foil strain gauges bonded to a proximal internal cavity in two half-bridge configurations and a distal, intramedullary (inside the bone canal) extension to the prosthesis. The distal-femoral, intramedullary extension was the earliest attempt to measure loading near the knee joint. This implant was powered using inductive coupling and allowed for the axial strain in the femoral prosthesis to be measured. Implant



Figure 2.3: Knee instrumented prosthesis proposed by Bergmann's group. <http://jwi.charite.de/en/research/>.

forces were measured at 2.5 up to 4 times body weight during for jumping activities, 1.2 times body weight for treadmill gait activities, and about 1.4 times body weight for stair climbing and descending activities [26].

Darryl D'Lima and Clifford Colwell have recently published information regarding a tibial prosthesis instrumented with strain gauges and telemetry. This was a ten-year project performed in collaboration with several industrial partners. For this project, a tibial tray was modified by DePuy and instrumented by Microstrain, Inc. and Kenton Kaufman of NK Biotechnical [27]. The portion of the tibial tray comprising the tibial plateau was modified to function as a load cell (Fig. 2.4). The tray was separated into upper and lower halves connected by four short rods. Material was removed from areas in the lower portion of the tray to form four diaphragms, and strain gauges were attached to these areas, which

resemble four load cells at the anteriomedial, anteriolateral, posteriomedial, and posteriolateral corners of the implant. The hollow portion of the stem of the tibial tray enclosed the electronics for this system. This system was powered using inductive coupling, and power was transmitted using a coil worn around the leg of the subject. This device appears to have been fabricated using off-the-shelf surface-mount electronic components [28]. In a recent publication on the follow-up of the implantation procedure, they showed peak forces during gate averaged 2.2 times body weight. Stair climbing averaged 1.9 times body weight six days following the procedure and increased to 2.5 times body weight six weeks following the initial procedure [29].

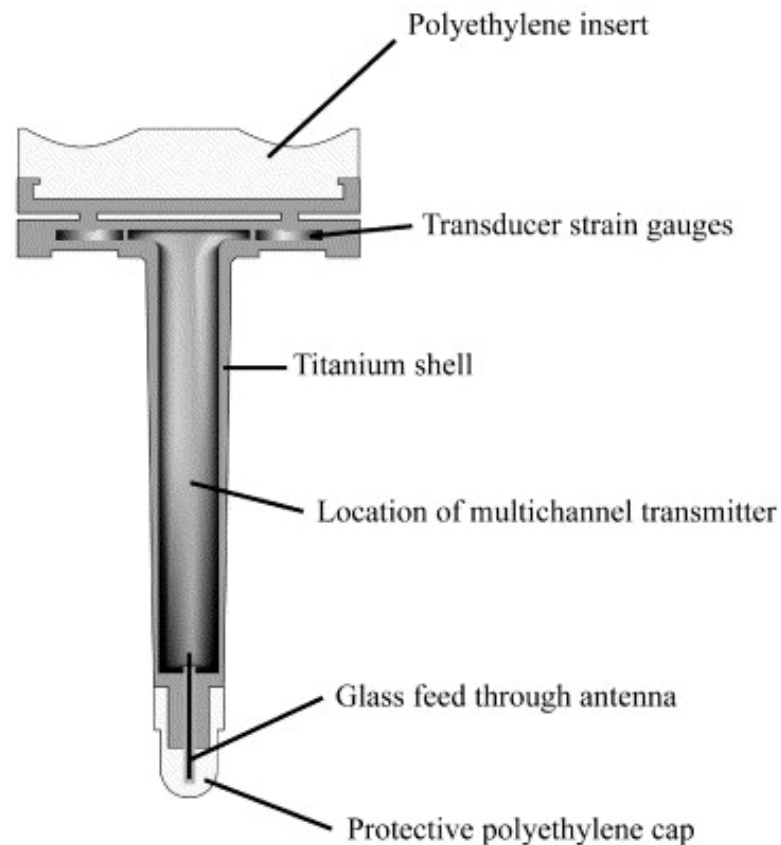


Figure 2.4: Knee instrumented prosthesis proposed by D'Lima [28].

### 2.2.5 MEMS strain and pressure sensors summary

Previous researchers investigating miniaturized sensors for the measurement of strain, pressure, and displacement have performed excellent work. However,

in the case of MEMS devices mentioned, the measurement range has been several orders of magnitude smaller than those required for the measurement of orthopedic loads. Also, previous work on orthopedic load determination, despite being extensive, has not provided a pathway to low-power long-term exchangeable biocompatible implantable sensors for measuring the dynamic loads in orthopedic components.

## 2.3 Stress/Strain measurements

The terms stress and strain are used to describe loads on and deformations of solid materials. The description of stress/strain is simpler in a solid that is homogenous and isotropic. Homogeneous means that the material properties do not differ at different locations and isotropic means the material properties are independent of direction in the material.

The concepts of stress and strain are introduced in the context of a long homogeneous isotropic bar subjected to a tensile load. The stress  $\sigma$  is the applied force  $F$  divided by the cross-sectional area  $A_0$ . The resulting strain  $\epsilon$  is the length change  $\Delta l$  divided by the initial length  $l_0$ . The bar elongates in the direction the force is pulling (longitudinal strain  $\epsilon_l$ ) and contracts in the direction perpendicular to the force (transverse strain  $\epsilon_t$ ).

A good way for describing stresses is by means of the method of analysis used in the mechanics of materials, assuming the equilibrium of forces. Therefore we have:

$$\Sigma F = 0 \quad (2.1)$$

$$F - \sigma A_0 = 0 \quad (2.2)$$

$$\sigma = \frac{F}{A_0} \quad (2.3)$$

where engineering (average) stress can be calculated by dividing the applied tensile force (normal to the cross section) by the area of the original cross-

sectional area. In this description the following stress convention is used: tensile stresses are positive and compressive stresses are negative.

As the applied force  $F$  increases, the length  $l$  also increases. For a force increase  $\partial F$ , the length  $l$  increases by  $\partial l$ . The normalized (per unit length) increase in length is defined by the following equation following equation:

$$\partial\varepsilon = \frac{\partial l}{l_0} \quad (2.4)$$

Upon integration of the equation above the engineering (average) strain in the direction of the tensile load can be found by dividing the change in length,  $\partial l$  by the original length  $l_0$ ,

$$\varepsilon = \int_{l_0}^l \frac{\partial l}{l_0} = \frac{l - l_0}{l_0} \quad (2.5)$$

The sign convention for strains is the same as that for stresses: tensile strains are positive, compressive strains are negative. When the strain is reasonably small, several solid materials behave like linear springs; that is, the displacement is proportional to the applied force.

Elastic material properties are defined in terms of stress and strain. In the linear range of material response, the stress is proportional to the strain, following Hooke's law. This law postulates the stress varies linearly with strain, and the Young's modulus  $E$  may be determined from the slope of a stress-strain curve or by dividing stress by strain,

$$E = \frac{\sigma}{\varepsilon} \quad (2.6)$$

Several types of sensors are used to measure strain, e.g. piezoresistive and piezoelectric sensors. Each type of sensor requires its own specialized signal conditioning. Selection of the best strain sensor for a given measurement is based on many factors, including specimen geometry, temperature, strain rate, frequency, magnitude, as well as cost, complexity, accuracy, spatial resolution, time resolution, sensitivity to transverse strain, sensitivity to temperature, and complexity of signal conditioning [2].

### 2.3.1 Strain gauges

Strain gauges transduce a mechanical signal into an electrical one by measuring the change in resistance of a strained metallic conductor. The stress acting on the strain gauge (area =  $A$ , length =  $L$ , resistivity =  $\rho$ ) will cause the strain gauge to either elongate or shorten, inducing the change of resistance according to the equation below.

$$R = \frac{\rho L}{A} \quad (2.7)$$

$$\frac{\Delta R}{R} = \frac{\rho}{A} \frac{\Delta L}{L} \quad (2.8)$$

The quantity  $\Delta L/L$  is a measure of the strain applied to the strain gauge, and is usually expressed in microstrains ( $1 \mu\epsilon = 10^{-6} \text{m/m}$ ).

Piezoresistive foil and wire gauges comprise: a thin insulating/encapsulating substrate (usually made of polymers), a foil or wire grid (usually made of metallic components) bonded to the substrate, and lead wires to connect the grid to a resistance measuring circuit. The grid (wire meandering) is typically made in a single direction so that strain will stretch the meandering strip of the strain gauge in the length direction (parallel to the direction of the meandering strip). The gauges are designed so that strain in the width (transverse direction) can be neglected. This makes the strain gauge sensitive to strain along its length. A typical metal foil strain gauge is depicted in Fig. 2.5.

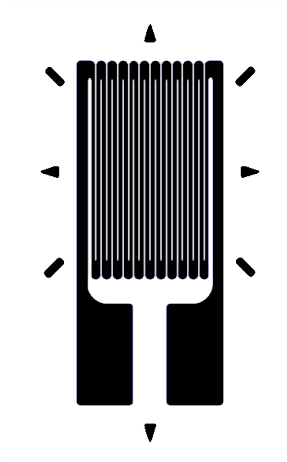


Figure 2.5: Strain gauge.

When piezoresistive foil or wire strain gauges are bonded to a specimen and the specimen is strained, the strain gauge strains as well. The resistance change is related to the strain by a gauge factor or strain factor of a strain gauge defined by equation 2.9, the ratio of relative change in electrical resistance to the applied strain  $\epsilon$ , which is the relative change in length, and a dimensionless quantity.

$$GF = \frac{\text{relative change in electrical resistance}}{\text{applied strain}} = \frac{\frac{\Delta R}{R}}{\frac{\Delta L}{L}} = \frac{\Delta R}{R} \frac{L}{\Delta L} = \frac{\Delta R}{R} \frac{1}{\epsilon} \quad (2.9)$$

In practice, the resistance is also dependent on temperature. The total effect is given below, with  $\alpha$  being the temperature coefficient and  $\Delta T$  being the temperature change.

$$\frac{\Delta R}{R} = GF\epsilon + \alpha\Delta T \quad (2.10)$$

Strain of piezoresistive materials produces a relative resistance change. The resistance change is the result of changes in resistivity and dimensional changes. Consider a single leg of the grid of a strain gauge with a rectangular cross-



section (Fig. 2.6).

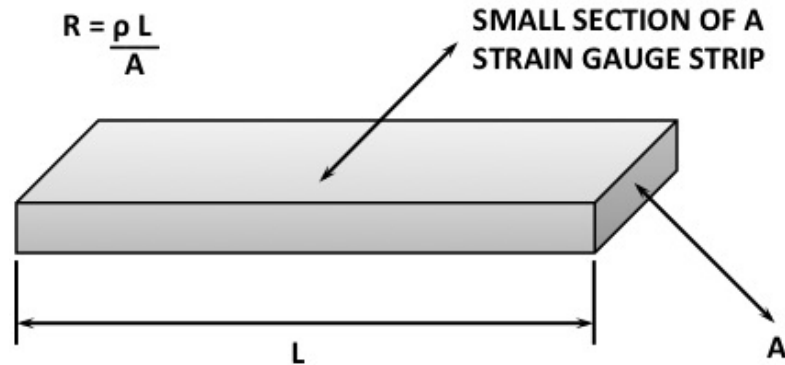


Figure 2.6: A single leg of a piezoresistive gauge is used to explain the source of the relative resistance change that occurs in response to strain.

Assuming this block is made of resistive material then its resistance is given by the equation below,

$$R = \frac{\rho l}{A} = \frac{\rho l}{wt} \quad (2.11)$$

where  $\rho$  is the bulk resistivity of the material ( $\Omega\text{cm}$ ),  $l$  is the length, and  $A$  is the cross-sectional area (i.e., the product of width  $w$  and thickness  $t$ ).

Differentiating the equation above gives

$$\partial R = \frac{l}{wt} \partial \rho + \frac{\rho}{wt} \partial l - \frac{\rho l}{w^2 t} \partial w - \frac{\rho l}{wt^2} \partial t \quad (2.12)$$

hence

$$\frac{\partial R}{R} = \frac{\partial \rho}{\rho} + \frac{\partial l}{l} - \frac{\partial w}{w} - \frac{\partial t}{t} \quad (2.13)$$

By definition,  $\varepsilon = \partial l/l$ , so the following equations apply in the assumption we are dealing with small changes, and hence  $\partial l = \Delta l$ ,  $\partial w = \Delta w$ , and  $\partial t = \Delta t$ :

$$\frac{\Delta w}{w} = \varepsilon_w = -\nu\varepsilon \quad (2.14)$$

$$\frac{\Delta t}{t} = \varepsilon_t = -\nu\varepsilon \quad (2.15)$$

where  $\nu$  is Poisson's ratio. The minus signs indicate the width and thickness are both under compression. The Poisson's ratio is a measure of the Poisson effect happening when a material is expanded in one direction; it usually tends to contract in the other two directions perpendicular to the direction of expansion.

Therefore, the relative resistance change is given by the following equation:

$$\frac{\Delta R}{R} = \frac{\Delta \rho}{\rho} + \frac{\Delta l}{l}(1 + 2\nu) \quad (2.16)$$

The contribution to the overall resistance change can be found in terms of strain using the elastic constitutive law [30]. The results lead to an elastic gauge factor just over 2 for microfabricated strain gauges, since the geometric effect dominates the piezoresistive effect. If the applied strain is too large, the foil or wire in the gauge will experience plastic deformation. When the deformation is plastic, the resistivity change is negligible and the dimensional change dominates. When metals undergo plastic deformation, they do not unload to the initial strain. This shows up as hysteresis in the gauge response, that is, upon withdrawing the load, the resistance does not return to its initial value.

### 2.3.2 Measuring force and pressure

Strain gauges are devices commonly employed to measure pressure and force. However in order to obtain an accurate and reliable data from the measurements

the strain gauge needs to be properly installed, placed satisfying the sensor geometry requirements, and calibrated. A block diagram of this process is shown in Fig. 2.7. The strain gauge measures force indirectly by measuring the strain due to the deflection of a calibrated carrier (e.g., parts such as torque shafts, crankshafts, gears, bearings, balances, and membranes). Pressure can also be converted into a force using transducers, meaning that strain gauges can be used to measure pressure. A range of sensing elements designed to deform under applied pressure can be fabricated using micromachining techniques, the most common by far being the diaphragm. The performance the device will depend upon the behavior of the sensor element, the influence of the material from which it is made, and the nature of the transduction mechanism. Another important aspect of such devices that define the most appropriate type of sensor for a particular application are the specifications (e.g. operating range of the sensor and temperature drift).

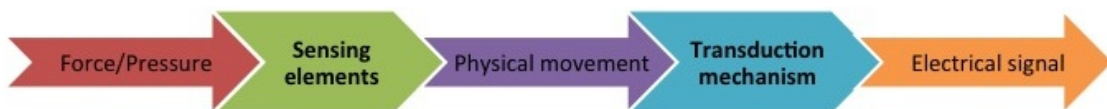


Figure 2.7: Block diagram of force/pressure sensor components.

### 2.3.3 Electronic interfacing - The Wheatstone bridge

The Wheatstone bridge offer a good method for measuring small changes in resistance. It was named after the inventor Charles Wheatstone for being the first to use this configuration for performing highly accurate measurement of electrical resistance. The basic Wheatstone bridge consists of four resistors connected in a square circuit, as shown in Fig. 2.8, and the bridge equation is presented below.

$$V_{output} = \left[ \frac{R_4}{R_4 + R_3} - \frac{R_2}{R_1 + R_2} \right] V_{input} \quad (2.17)$$

For a system employing the Wheatstone bridge the deviation of one or more resistors in the arrange will affect the output voltage. Due to the usually small

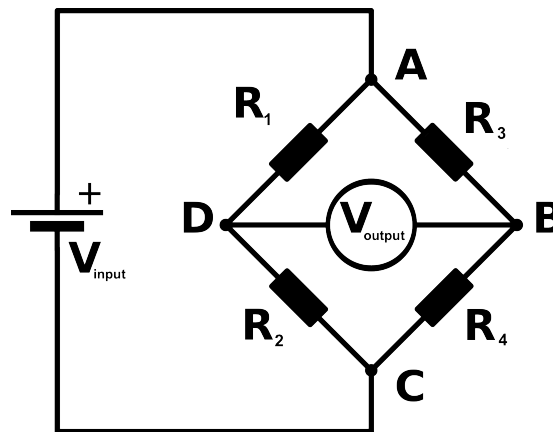


Figure 2.8: Basic Wheatstone bridge.

resistance changes, the output voltage change may be as small as tens of millivolts, therefore signal conditioning are generally used coupled with Wheatstone bridges. The changes in resistance, in the majority of the applications, is an indirect indication of the magnitude of the variable under investigation (e.g. force). The relative resistance change of a piezoresistive gauge is generally measured using such Wheatstone bridge, and by calibrating the Wheatstone bridge it is possible to measure small changes in resistance relative to an initial zero value, allowing measurements with better resolution.

There are four commonly used Wheatstone bridge configurations suitable for sensor applications. These configurations are presented in Fig. 2.9 (A to D) as well as the equations relating the bridge output voltages to the excitation voltages and the bridge resistance values [31]. The Wheatstone bridge is also a versatile electronic circuit since it can be used to directly cancel the effect of thermal drift. For example, by using two or four strain gauges in a Wheatstone bridge its possible to minimize the effect of temperature. With all strain gauges in a bridge at the same temperature and mounted on the same material, any changes in temperature will likely to affect all gauges in the same way. Because the temperature changes are identical in the gauges, the ratio of their resistance does not change, and the output voltage of the gauge does not change.

In certain application, such as force and pressure measurements, the Wheatstone bridge is used to provide a highly sensitive output from transducers

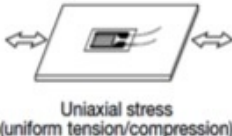
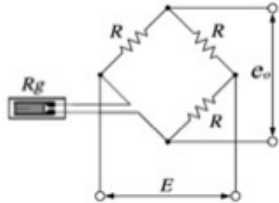
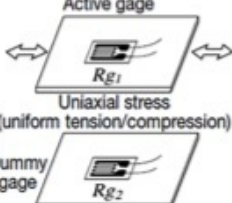
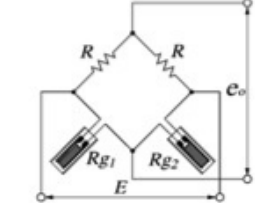
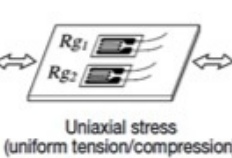
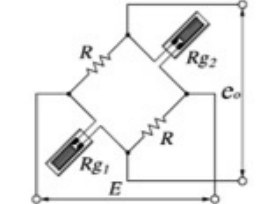
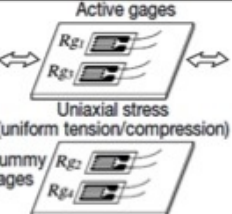
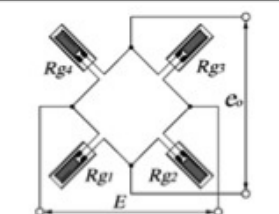
<p><b>A</b></p> <p>1-active-gage 2-wire system</p> <p>Number of gages: 1</p>	 <p>Uniaxial stress (uniform tension/compression)</p>		$e_o = \frac{E}{4} K_s \cdot \epsilon_o$ <p> <math>K_s</math>: Gage factor  <math>\epsilon_o</math>: Strain  <math>E</math>: Bridge voltage  <math>e_o</math>: Output voltage  <math>R_g</math>: Gage resistance  <math>R</math>: Fixed resistance                 </p>	<p>Suitable for use under environment of less ambient temperature changes; no temperature compensation. x1 output</p>
<p><b>B</b></p> <p>Active-dummy 2-gage system</p> <p>Number of gages: 2</p>	 <p>Active gage <math>R_{g1}</math></p> <p>Uniaxial stress (uniform tension/compression)</p> <p>Dummy gage <math>R_{g2}</math></p>		$e_o = \frac{E}{4} K_s \cdot \epsilon_o$ <p> <math>K_s</math>: Gage factor  <math>\epsilon_o</math>: Strain  <math>E</math>: Bridge voltage  <math>e_o</math>: Output voltage  <math>R_{g1}</math>: Strain: <math>\epsilon_o</math>  <math>R</math>: Fixed resistance  <math>R_{g2}</math>..... Strain: 0                 </p>	<p>Temperature compensation; thermal effect of leadwires cancelled. x1 output</p>
<p><b>C</b></p> <p>Opposite side 2-active-gage 2-wire system</p> <p>Number of gages: 2</p>	 <p>Uniaxial stress (uniform tension/compression)</p>		$e_o = \frac{E}{2} K_s \cdot \epsilon_o$ <p> <math>R_{g1}</math>..... Strain: <math>\epsilon_o</math>  <math>R_{g2}</math>..... Strain: <math>\epsilon_o</math>  <math>R</math>: Fixed resistance                 </p>	<p>No temperature compensation; bending strain cancelled by bonding to the front and rear. x2 output</p>
<p><b>D</b></p> <p>Active-dummy 4-gage system</p> <p>Number of gages: 4</p>	 <p>Active gages <math>R_{g1}</math> <math>R_{g2}</math></p> <p>Uniaxial stress (uniform tension/compression)</p> <p>Dummy gages <math>R_{g3}</math> <math>R_{g4}</math></p>		$e_o = \frac{E}{2} K_s \cdot \epsilon_o$ <p> <math>R_{g1}, R_{g3}</math>..... Strain: <math>\epsilon_o</math>  <math>R_{g2}, R_{g4}</math>..... Strain: 0                 </p>	<p>Temperature compensation; thermal effect of leadwires cancelled; bending strain cancelled by bonding to the front and rear. x2 output</p>

Figure 2.9: Four commonly used bridge configurations suitable for sensor applications [31].

(when using transducers as one or more elements of the Wheatstone bridge). Considering the full-scale outputs of such devices are small voltages, currents, or resistance changes, it is required that the output signals to be conditioned before any performing analog or digital processing. These circuits are known as signal-conditioning circuits. Examples of such circuits are amplification, linearization, and filtering. However, the performance of the sensor will mainly depend on the electrical character of the sensor and its output.

### Signal conditioning

There exist many data acquisition boards and units that can be readily interfaced to a computer, providing analog and digital inputs and outputs, however

it is still necessary to use signal-conditioning circuitry to either drive a MEMS device or to amplify and filter the signal received from a sensor. The challenge of selecting the right amplifier for a particular signal-conditioning application is complicated by the wide selection of processes, architectures, and such amplifiers. One of the most used amplification devices is the instrumentation amplifier, which is a type of differential amplifier that eliminates the need for input impedance matching due to the additional input buffers making the amplifier particularly suitable for use in situations in which a differential measurement is preferable to an absolute measurement. The instrumentation amplifier configuration is basically a closed-loop gain block, which is single-ended with respect to a reference terminal (Fig. 2.10). The input impedances are balanced and have high values. Unlike an operational amplifiers an instrumentation amplifier uses an internal feedback resistor network that is isolated from its signal input terminals. An important aspect of the instrumentation amplifier is that it is capable of amplifying microvolt signals, while simultaneously rejecting volts of common mode signals of its inputs.

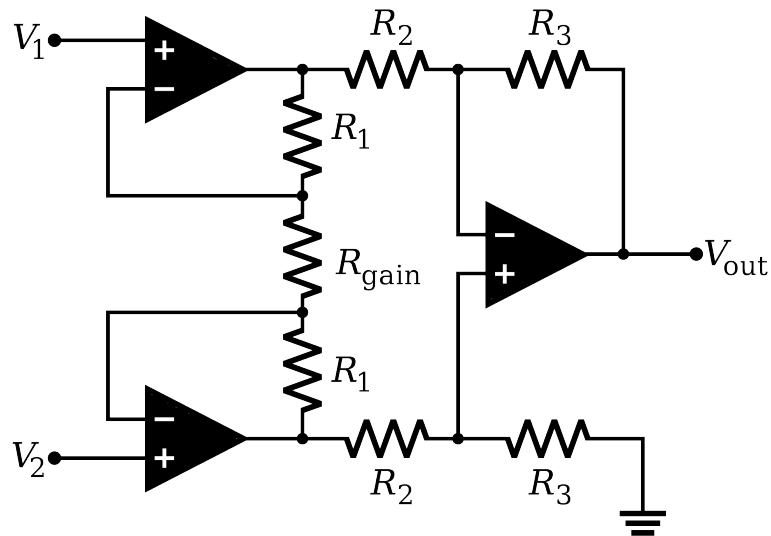


Figure 2.10: Instrumentation amplifier schematics.

## 2.4 Release and Detachment

At the end of the fabrication process the devices need to be detached without damage from the fabrication support in order to be used. Device detachment has been extensively studied since it is a common and repetitive problem in micromachining. Many detachment or release procedures involve the use of a sacrificial material, which can be removed by wet chemical etching, dissolution in an appropriate solvent, dry etching or heating. A wide variety of sacrificial materials have been demonstrated for microstructure detachment, such as silicon-based materials, metals, photoresists, and polymers [32]. The major problem with sacrificial materials is that for releasing large devices the under etch distances are very large and the structures might be exposed to the etchant for a considerable amount of time and decrease the yield. In flexible polymer-based devices, structures can be detached by using a special surface treatment on the fabrication support, by using the crack propagation at the interface between the fabrication support and the flexible device, and by using different kinds of sacrificial materials. In the case of polyimide-based devices an interesting method for the detachment of microfabricated structures is the anodic metal dissolution of an Al sacrificial layer in a saline solution.

### 2.4.1 Anodic dissolution

Anodic metal dissolution is based on the principle of electrochemical metal removal from the working electrode, which constitutes the anode in an electrolytic cell. A non-toxic salt solution is used as electrolyte and an external current is applied to control the material removal rates. Several metallic films of interest in the microelectronics industry can be anodically dissolved in neutral salt solutions (e.g. sodium chloride), allowing for an environmentally friendly fabrication procedure [33]. Aluminum is well suited as sacrificial layer and it is fully compatible with the clean room process. In order to perform an anodic dissolution of Al a potential of at least 0.7 V is applied to the electrochemical cell so that the dissolution of Al occurs at reasonable speed. Another important aspect is the selection of an appropriate metal as cathode and anode back electrode that is stable at a potential needed for Al dissolution (0.7 V), other-

wise contaminants might pollute the system and prevent its usage, specially in biomedical applications. To avoid such problems Pt and W:Ti10% can be used as cathode or anode back electrode since they are known to be stable material that are not easily dissolved by chemicals used during microsystems fabrication.

The schematic of an electrochemical cell used for the anodic dissolution of Al and detachment of polyimide-based microdevices is presented in Fig. 2.11. In this process the wafers with the devices to be released are immersed into a saturated NaCl solution. A constant positive potential of 0.7 V is applied to the aluminum layer by a voltage supply while another wafer with sputtered platinum layer is used as counter electrode. After the detachment, the microdevices become available in the electrolyte solution and can be retrieved for subsequent rinsing and drying.

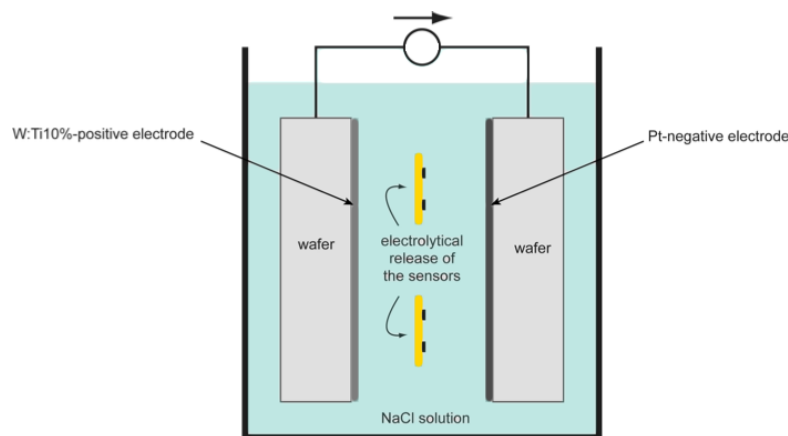


Figure 2.11: Schematic of an electrochemical cell used for the anodic dissolution of aluminum [33].

## 2.5 Finite Element Analysis

Finite Element Analysis (FEA) was first developed in 1943 to obtain approximate solutions to vibration systems and, shortly thereafter, in 1956 a broader definition of numerical analysis was established in a scientific article centered on the "stiffness and deflection of complex structures". By the early 70's, FEA expanded but was still limited to expensive mainframe computers generally



owned by the aeronautics, automotive, defense, and nuclear industries. However, with the rapid decline in the cost of computers and the phenomenal increase in computing power, FEA has been developed to produce accurate results for all kinds of problems.

FEA consists of a computer model of a material or design that is stressed and analyzed for specific results by using numerical techniques for finding approximate solutions to partial differential equations. In solving partial differential equations, the primary challenge is to create an equation that approximates the equation to be studied, but is numerically stable, meaning that errors in the input and intermediate calculations do not accumulate and cause the resulting output to be meaningless. This method is often used in new product design, and existing product refinement, since it is able to verify a proposed design will be able to perform to the desired specifications prior to manufacturing or construction. Also, FEA is employed in existing product or structure to help determine the design modifications to meet new conditions.

There are generally two types of analysis: 2-D modeling, and 3-D modeling. 2-D modeling conserves simplicity and allows the analysis to be run relatively fast to obtain information on the problem under investigation, however it tends to yield less comprehensive results, since a level of abstraction is necessary to understand the results. 3-D modeling, on the other hand, produces more comprehensive results while sacrificing the speed. Within each of these modeling schemes, the programmer can insert numerous algorithms which may make the system behave linearly or non-linearly, depending on the desired analyses that need to be performed. Linear systems are far less complex and generally do not take into account plastic deformation while non-linear systems do account for plastic deformation, and can analyze a material all the way to fracture.

In spite of the great power of FEA, the disadvantages of computer solutions must be kept in mind when using this and similar methods, since errors in input data can produce wildly incorrect results that may be overlooked by the investigator. Perhaps the most important function of theoretical modeling is that of sharpening the designer's intuition; users of finite element codes should

plan their strategy toward this end, supplementing the computer simulation with as much closed-form and experimental analysis as possible.

## 2.6 Biocompatibility

The importance of implantable devices in medicine is growing. Due to increasing life expectancy, there is a increasing number of devices to monitor the evolutions of disease conditions or even substitute deteriorating or failing body parts. Examples of implants are orthopedic joint prostheses, cardiovascular devices, dental implants, brain implant and others. Implants do not only comprises devices located inside de body, but also percutaneous devices, such as catheters for the infusion of fluids.

The most external part of implants are made from materials that have a common property: biocompatibility. Although biocompatibility is a difficult term to define, it is strongly related to the success of an implanted device in fulfilling its intended function while being harmless to the body. This implies that a biomaterial used for the manufacturing of a medical device or a implant, that is classified as biocompatible, cannot be used for the manufacturing of other devices with different functions. Therefore, if the same biomaterial is used in devices with different functions, extended tests and clinical trials are mandatory in order to guarantee de device safety and obtain its usage approval from the regulatory agencies.

For any new devices intended for use *in vivo* the biocompatibility has to be evaluated at several different levels. A first level is to identify any acute reaction that may immediate affect the host tissue. At a second stage it is necessary to evaluate the longer-term responses of the host tissue caused by the prolonged presence of the devices. Another important aspects to be evaluated during this stage, for example, is whether such materials promote excessive coagulation or elicit undesirable immunological responses. In applications in which non-biocompatible materials are necessary, the devices can be alternatively coated with some biomaterials in order to be used *in vivo* [33].

## 2.7 References

- [1] D. Banks, *Microengineering, MEMS, and Interfacing: A Practical Guide*. CRC Press, 1 ed., Mar 2006.
- [2] J. Webster, *The Measurement, Instrumentation, and Sensors Handbook*. Electrical Engineering Handbook Series, CRC Press, 1999.
- [3] R. Perez, *Design of Medical Electronic Devices*. Academic Press, Feb 2002.
- [4] D. M. Stefanescu, *Handbook of Force Transducers: Principles and Components*. Springer, May 2011.
- [5] D. Crottet, *A force-sensing device for assistance in soft-tissue balancing during knee arthroplasty*. PhD thesis, 2005.
- [6] S. P. Beeby, G. Ensel, and M. Kraft, *MEMS Mechanical Sensors*. Artech House Publishers, Apr. 2004.
- [7] L. Löfdahl and M. Gad-el Hak, "Mems-based pressure and shear stress sensors for turbulent flows," *Measurement Science and Technology*, vol. 10, pp. 665–686, Aug 1999.
- [8] C. Hautamaki, S. Zurn, S. Mantell, and D. Polla, "Experimental evaluation of mems strain sensors embedded in composites," *Journal of Microelectromechanical Systems*, vol. 8, pp. 272–279, Sep 1999.
- [9] L. Cao, T. S. Kim, S. C. Mantell, and D. L. Polla, "Simulation and fabrication of piezoresistive membrane type mems strain sensors," *Sensors and Actuators A: Physical*, vol. 80, pp. 273–279, Mar 2000.
- [10] M. C. Hsieh, Y. K. Fang, M.-S. Ju, G.-S. Chen, J.-J. Ho, C. Yang, P. M. Wu, G. Wu, and T. Y.-F. Chen, "A contact-type piezoresistive micro-shear stress sensor for above-knee prosthesis application," *Journal of Microelectromechanical Systems*, vol. 10, pp. 121–127, Mar 2001.
- [11] G. Bitko, R. Harries, J. Matldn, A. C. McNeil, D. J. Monk, M. Shah, and J. Wertz, "Thin film polymer stress measurement using piezoresistive anisotropically etched pressure sensors," *MRS Online Proceedings Library*, vol. 436, 1996.
- [12] B. Gogoi and D. Mladenovic, *Integration technology for MEMS automotive sensors*, vol. 4, pp. 2712–2717. Nov 2002.
- [13] L. Lin and W. Yun, *MEMS pressure sensors for aerospace applications*, vol. 1, pp. 429–436. Mar 1998.

- [14] T. Eggers, C. Marschner, U. Marschner, B. Clasbrummel, R. Laur, and J. Binder, *Advanced hybrid integrated low-power telemetric pressure monitoring system for biomedical applications*, pp. 329–334. Jan 2000.
- [15] W. P. Eaton and J. H. Smith, “Micromachined pressure sensors: review and recent developments,” *Smart Materials and Structures*, vol. 6, pp. 530–539, Oct 1997.
- [16] L. Lin, A. Pisano, and R. Howe, “A micro strain gauge with mechanical amplifier,” *Journal of Microelectromechanical Systems*, vol. 6, pp. 313–321, Dec 1997.
- [17] K. Wojciechowski, B. Boser, and A. Pisano, *A MEMS resonant strain sensor with 33 nano-strain resolution in a 10 kHz bandwidth*, p. 4 pp. Nov 2005.
- [18] B. Kane, M. Cutkosky, and G. Kovacs, “A traction stress sensor array for use in high-resolution robotic tactile imaging,” *Journal of Microelectromechanical Systems*, vol. 9, pp. 425–434, Dec 2000.
- [19] J. Engel, J. Chen, and C. Liu, “Development of polyimide flexible tactile sensor skin,” *Journal of Micromechanics and Microengineering*, vol. 13, pp. 359–366, May 2003.
- [20] H. Kawaguchi, T. Someya, T. Sekitani, and T. Sakurai, “Cut-and-paste customization of organic fet integrated circuit and its application to electronic artificial skin,” *IEEE Journal of Solid-State Circuits*, vol. 40, pp. 177–185, Jan 2005.
- [21] J. G. Webster, *Tactile Sensors for Robotics and Medicine*. John Wiley amp; Sons, Inc., 1st ed., 1988.
- [22] R. D. Komistek, T. R. Kane, M. Mahfouz, J. A. Ochoa, and D. A. Dennis, “Knee mechanics: a review of past and present techniques to determine in vivo loads,” *Journal of Biomechanics*, vol. 38, pp. 215–228, Feb 2005.
- [23] T. A. English and M. Kilvington, “In vivo records of hip loads using a femoral implant with telemetric output (a preliminary report),” *Journal of Biomedical Engineering*, vol. 1, pp. 111–115, Apr 1979. PMID: 537339.
- [24] F. Graichen, R. Arnold, A. Rohlmann, and G. Bergmann, “Implantable 9-channel telemetry system for *in vivo* load measurements with orthopedic implants,” *IEEE Transactions on Biomedical Engineering*, vol. 54, pp. 253–261, Feb 2007.
- [25] G. M. Kotzar, D. T. Davy, V. M. Goldberg, K. G. Heiple, J. Berilla, K. G. Heiple, R. H. Brown, and A. H. Burstein, “Telemeterized in vivo hip joint force data: A report on two patients after total hip surgery,” *Journal of Orthopaedic Research*, vol. 9, no. 5, pp. 621–633, 1991.

- [26] E. Bassey, J. Littlewood, and S. Taylor, "Relations between compressive axial forces in an instrumented massive femoral implant, ground reaction forces, and integrated electromyographs from vastus lateralis during various osteogenic exercises," *Journal of Biomechanics*, vol. 30, pp. 213–223, Mar 1997.
- [27] K. R. Kaufman, N. Kovacevic, S. E. Irby, and C. W. Colwell, "Instrumented implant for measuring tibiofemoral forces," *Journal of Biomechanics*, vol. 29, pp. 667–671, May 1996.
- [28] D. D. D'Lima, C. P. Townsend, S. W. Arms, B. A. Morris, and C. W. Colwell Jr, "An implantable telemetry device to measure intra-articular tibial forces," *Journal of Biomechanics*, vol. 38, pp. 299–304, Feb 2005.
- [29] D. D. D'Lima, S. Patil, N. Steklov, J. E. Slamin, and C. W. Colwell, "Tibial forces measured in vivo after total knee arthroplasty," *The Journal of Arthroplasty*, vol. 21, pp. 255–262, Feb 2006.
- [30] C. S. Lynch, "Strain compensated thin film stress gauges for stress wave measurements in the presence of lateral strain," *Review of Scientific Instruments*, vol. 66, pp. 5582–5589, Dec 1995.
- [31] W. N. S. Jr and W. N. Sharpe, *Springer Handbook of Experimental Solid Mechanics*. Springer, Dec 2008.
- [32] S. Metz, A. Bertsch, and P. Renaud, "Partial release and detachment of microfabricated metal and polymer structures by anodic metal dissolution," *Journal of Microelectromechanical Systems*, vol. 14, pp. 383–391, Apr 2005.
- [33] M. Leonardi, "Microfabricated thin film strain gage sensor with telemetry microprocessor embedded in a soft contact lens for minimally invasive intraocular pressure monitoring," vol. 3978, 2008.

# CHAPTER 3

## Selected Biomedical Applications

*The art of medicine consists in amusing  
the patient while nature cures the disease.*

*- Voltaire*

### 3.1 Orthopaedic surgery

Orthopaedic surgery is a branch of surgery concerned with injuries and disorders of the musculoskeletal system. The early development of orthopaedic surgery can be traced back to the usage of tourniquets and suturing of large vessels for amputations, associated with the development of artificial limbs using iron or wood. The modern orthopaedics is considered to have started on the last century with the development of X-rays and also with the fact that orthopaedics became a specialty in its own. Since then, the surgical techniques, the tools for diagnosis and the instrumentation have been continuously improved with the objective of obtaining predictable and satisfying outcome of orthopaedic interventions. Nowadays, the large majority of the instrumentation for orthopaedic surgery consists in mechanical tools (e.g. saws, drillers, and mechanical ancillaries) that provide the surgeon with instruments to attest morphological parameters of bones as well as to correct and repair bony structure.

To improve the surgery outcome and the safety of orthopaedic interventions sensors can be used to give real-time feedback to the surgeons in the operating room. Despite of the great number of possibilities provided by the introduction of "smart instrumentation" current systems are mainly limited to the control of geometrical parameters while important biomechanical parameters such as stress in soft-tissue or forces applied by the surgeon still remain unknown. Measurement of forces with smart instrumentation and modified prosthesis can therefore improve the quality of orthopaedic surgery.

Some of the benefits includes the detection of possible damage of healthy tissues, force monitoring of surgical actions for optimal adjustment of soft-tissue, assistance for optimal implant placement and lifetime monitoring of prosthesis. To achieve a satisfying stability and improve the lifetime of the prosthetic joint, the alignment of the bones and the forces experienced by the surrounding soft-tissue must be optimally corrected at the time of the surgery. The intraoperative use of instrumented tools or specific force-sensing devices embedded on the prosthesis could provide valuable measurements to assist

the surgeon in optimally balancing the soft-tissue tensions as well as to give reliable post-surgery feedback on the implant evolution.

### 3.1.1 Total knee arthroplasty

Total Knee Arthroplasty (TKA) is a widely used surgical procedure to replace a damaged knee joint by an artificial knee implant with the main goal of relieving the pain and restoration of motion [1, 2]. Total knee arthroplasty (TKA) is nowadays a standard procedure for the treatment of degenerative diseases and injuries at the knee joint, and due to the increase in population and life time expectancy the number of TKA has been continuously increasing over the last years [3]. Moreover the age at the time of primary TKA is decreasing therefore it is critical to ensure operation success and to access the status of the artificial knee implant along its lifetime aiming to minimize the possibilities of revision surgery and to maximize the longevity of the implant [4].

Despite knee prostheses having been used for more the 100 years the intensive development of TKA started around the 1950's. Design limitations in those early days included improper sizing, no provision for replacing the patello-femoral joint, lack of rotational freedom and improper stem fixation. Design of condylar knee replacement and polycentric knees were developed by the 1970's, while the 1980's and 1990's were spent for design improvements, thus allowing: better fixation with or without cement; reduced wear; enhanced kinematics and increased range of motion [5]. The standard modern artificial joint is composed of three parts being two metallic parts (femoral and tibial components) and a polyethylene inlay. Fig. 3.1 presents a modern artificial knee comprising the Cr-Co-Mo femoral and tibial components, and an Ultra High Molecular Weight (UHMW) Polyethylene (PE) insert, as well as an illustration of the knee structure before and after TKA. In the current age of technological advances, reproducing knee kinematics, minimizing wear and increasing range of motion with proper alignment and stability have become the major goals of TKA.





Figure 3.1: Modern artificial knee comprising the Cr-Co-Mo femoral and tibial components and an Ultra High Molecular Weight (UHMW) Polyethylene (PE) insert, and an illustration of the knee structure before and after TKA (picture modified from A.D.A.M., Inc. - <http://www.healthcentral.com/rheumatoid-arthritis/9494-146.html>).

### Knee anatomy

The knee is the largest and most complex joint in the human body. It combines two major functions: one allowing the transmission of large forces required for stability supporting nearly three to four times the body weight during stair climbing, or even higher forces during jumping that can reach fifteen times the body weight, and a second providing a high degree of flexibility with a range of motion of up to  $140^\circ$  in flexion. The combination of these two functionalities is only possible throughout a perfect interplay between all the components of the knee.

Fig. 3.2 presents the anatomy of the knee. The knee is a two-joint structure composed of the tibio-femoral and patello-femoral joints. The bones of the knee (femur and tibia) meet to the knee joint. The joint is protected by the patella in the frontal part. It is also composed by an articular cartilage that wrap the ends of the femur and the tibia, as well as the underside of the patella. The lateral meniscus and medial meniscus are protections of cartilages that acts as shock absorbers between the bones.

Ligaments help to stabilize the knee. The collateral ligaments (medial and

lateral) limit the abduction-adduction rotation movements (medio-lateral translation from the tibia with respect to the femur). The anterior cruciate ligament, or ACL, connects the tibia to the femur at the center of the knee and limits rotation and forward motion of the tibia. The posterior cruciate ligament, or PCL, limits backward motion of the tibia and it is located behind the ACL.

The patello-femoral joint consists of the femur and the patella, which is a flat bone placed as a cap to the knee. The patella is held by the patellar tendon on the tibial side and by the quadriceps, the most effective active knee stabilizers, on the femoral side. The patellofemoral joint supports the extension of the knee and works as a sagittal stabilizer. The patella is also a protection for the knee in the frontal plane.

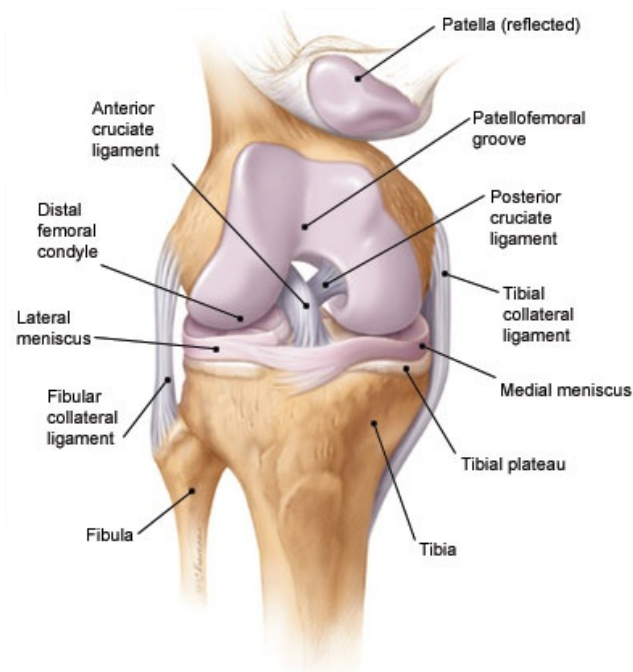


Figure 3.2: Anatomy of the knee. Reprinted from Tandeter H.B., Shvartzman P., Stevens M.A.. *Acute knee injuries: use of decision rules for selective radiograph ordering. Am Fam Physician* 1999; 60:2600.

All these components are the basis of the six degrees of freedom (DOF) motion of the knee (Fig. 3.3). Three of these DOF are translations along the anterior-posterior, medial-lateral, and inferior-superior axes defined at the joint, whereas the other three DOF are rotations around each axis. Because of the deformable

nature of joint soft tissues and the inherent laxity within joints, movement occurs in all six DOF during physiologic motion (although most joints have a limited number of DOF with a large range of motion).

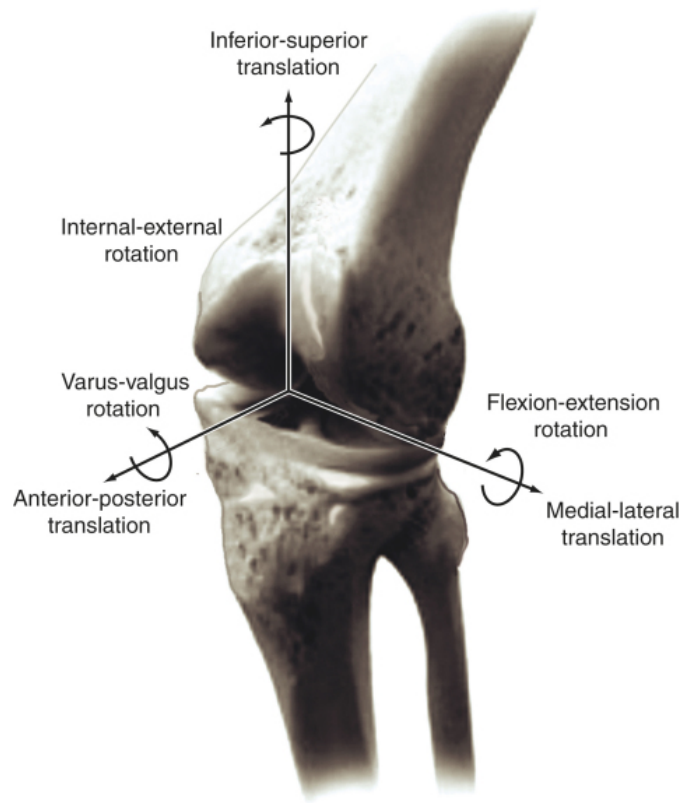


Figure 3.3: The six degrees of freedom motion of the knee joint.

### **Alignment and stability**

A successful TKA produces a well-aligned prosthesis with good ligament balance. The success crucially depends on preoperative assessment of the deformity and the soft-tissue situation (extrinsic stability), the correct choice of implant (intrinsic stability), which also depends on the former, and the adequate intraoperative treatment of the soft-tissue stabilizers.

It is possible to achieve excellent overall alignment and still fail to achieve ligament balance. If the alignment is suboptimal, the distribution of the load created by the body weight is not homogeneously distributed and may provoke postoperative complications. Misalignment has four basic consequences:

interface overload results in prosthesis loosening, lastic overload accelerates prosthesis wear, ligament overload produces pain and/or limit overall motion, and knee instability. By understanding the normal alignment of the human knee, its relationship to normal ligament function and kinematics, and the consequences of misalignment, the surgeon will be well positioned to achieve a high degree of accuracy in both alignment and balance [6].

Implant constraint failures are the consequence of inadequate balance between the given, intrinsic stability of the implant replacing a joint and the extrinsic stabilization provided by the soft-tissues enveloping the joint. In the knee, the stability of the joint is realized by a complex ligament structure. At the time of arthroplasty, this stability must be reevaluated and, if necessary, corrected to ensure a successful outcome. Although it is clear that the forces and moments transmitted across the patello-femoral and tibio-femoral joints affect metabolism of articular cartilage in the normal knee, and wear of joint replacements, very little is known about the magnitude and direction of these forces *in vivo*. In part, this is because the tools that are currently available permit only accurate measurement of displacements and rotations *in vivo*; they do not permit quantification of the forces and moments. A force-sensing device that can precisely measure intraoperative medial-lateral imbalance of the compressive forces of the knee joint could assist the surgeon in this delicate phase of ligament balancing. This would guarantee an optimal distribution of the compressive forces, leading to an increased lifetime of the prosthetic implants.

## **3.2 Cardiac Catheterization**

The modern concepts of heart disease are based on the physiologic and anatomic knowledge investigated in the past 70 years of experience in the cardiac catheterization laboratory. The very first cardiac catheterization was first performed in a horse subject, by Claude Bernard in 1844. By using an approach from the jugular vein and carotid artery he was able to enter both the right and left ventricles. Afterwards, investigation of cardiovascular physiology in animals was intensive followed, resulting in the development of many important techniques and principles (e.g., pressure manometry) which looked for direct

human application in patients with heart disease [7].

The development of catheterization continued in the 1950's and 1960's. The percutaneous technique was developed in 1953, and was soon applied to cardiac catheterization. Afterwards, the coronary angiography was modified for a percutaneous approach in 1962, and already in 1970 catheterization was made using a balloon-tipped catheter. The flow-guided catheter technique was also developed in the 1970s thus enabling the application of catheterization outside the laboratory environment.

As performed today, cardiac catheterization is a combined hemodynamic and angiographic procedure undertaken for diagnostic and often therapeutic purposes. The basic principle is that cardiac catheterization is recommended to confirm the presence of a clinically suspected condition, define its anatomic and physiologic severity. The most common indication for cardiac catheterization today thus consists of a patient with an acute coronary ischemic syndrome (unstable angina or acute myocardial infarction) in whom an invasive therapeutic intervention is necessary as well as for pressure monitoring in patients under intensive care.

### **3.2.1 Pressure monitoring**

Anesthesiologists and clinicians requiring accurate, continuous monitoring of intravascular pressures such as those of radial artery, pulmonary artery, and central vein regard direct measurement to be of fundamental importance. Invasive vascular pressure monitors are systems designed to record, analyze and display pressure information. There are a variety of invasive vascular pressure monitors and they are commonly used in trauma, critical care, and operating room applications for measurement and follow-up of arterial, venous, atrial, and intracranial pressures.

Arterial blood pressure (BP) is most accurately measured when performed invasively. Invasive arterial pressure measurement is performed by placing an intravascular catheter into an artery (usually radial, femoral, dorsalis pedis or brachial). The monitoring of arterial blood pressure is necessary to determine

the "health" of the circulatory system. If blood pressure is too low it can lead to things like fainting and can be a simple sign of dehydration, however if combined with inactivity, the presence blood clots might investigated. Low BP, is a medical concern only if it causes signs or symptoms, such as fainting and dizziness, or when arterial pressure decreases beyond a certain point that can prejudice the perfusion of the brain. If a high blood pressure is identified it can lead to many complications including aneurysms, kidney damage, eye damage and stroke, or even be an indication of certain tumors. High BP can be an indicator of other problems that can lead to long-term adverse effects, since it can damage the arterial walls due to mechanical stress. Higher pressures increase heart workload and promote unhealthy tissue growth within the walls of arteries, and persistent hypertension is a risk factors for heart attacks, heart failure, arterial aneurysms and strokes, and it is also the leading cause of chronic renal failure. Another condition possible to be identified with the catheterization is the fluctuating blood pressure. If fluctuations are significantly high it can be associated with reduced local cerebral blood flow and be an indication of cerebrovascular disease.

### 3.3 References

- [1] V. C. Mow and R. Huiskes, *Basic Orthopaedic Biomechanics and Mechano-Biology*, 3rd ed. Lippincott Williams & Wilkins, third edition ed., Dec. 2004.
- [2] B. Kirking, J. Krevolin, C. Townsend, C. W. Colwell Jr., and D. D. D'Lima, "A multiaxial force-sensing implantable tibial prosthesis," *Journal of Biomechanics*, vol. 39, no. 9, pp. 1744–1751, 2006.
- [3] A. C. Schirm, B. O. Jeffcote, R. L. Nicholls, H. Jakob, and M. S. Kuster, "Sensitivity of knee soft-tissues to surgical technique in total knee arthroplasty," *The Knee*, vol. 18, pp. 180–184, June 2011.
- [4] B. Heinlein, I. Kutzner, F. Graichen, A. Bender, A. Rohlmann, A. M. Halder, A. Beier, and G. Bergmann, "ESB clinical biomechanics award 2008: Complete data of total knee replacement loading for level walking and stair climbing measured in vivo with a follow-up of 6-10 months," *Clinical Biomechanics*, vol. 24, pp. 315–326, May 2009.
- [5] D. Crottet, *A force-sensing device for assistance in soft-tissue balancing during knee arthroplasty*. PhD thesis, 2005.
- [6] J. Bellemans, M. Ries, and J. Victor, *Total knee arthroplasty: a guide to get better performance*. Springer, 2005.
- [7] D. S. Baim and W. Grossman, *Grossman's Cardiac Catheterization, Angiography, And Intervention*. Lippincott Williams Wilkins, 2006.

## Smart Instrumentation for TKA

*This Chapter is based on the following article:*

*W. Hasenkamp, et. al.,*

*"Smart Instrumentation for Determination of Ligament Stiffness and  
Ligament Balance in Total Knee Arthroplasty",  
Medical Engineering Physics (accepted).*

*The important thing in science is not so much to obtain  
new facts as to discover new ways of thinking about them.*

*- Sir William Bragg*



## 4.1 Introduction

To maximize the surgical outcome, the TKA procedures rely on the surgical principle of soft-tissue balance (or ligament balance) to manage post-operative knee stability and mobility, and avoid early implant failure [1, 2]. Despite all the efforts on developing the set of instruments for TKA, ligament balance is still difficult to measure objectively during the operation, leaving its evaluation much to surgeon experience, feel and opinion [3].

The ligament balancing in TKA has the objective of distributing the tibiofemoral compressive forces symmetrically between the medial and lateral compartments as well as to reestablish an equivalent tibiofemoral gap in both flexion and extension [4]. Inadequate ligament balance can lead to unequal load distribution at the tibial-bearing surface consequently increasing prosthesis wear and resulting in early surgical revision [5, 6]. Ideally an instrument that measures simultaneously tibiofemoral forces and flexion-extension gaps could assist surgeons to determine the optimal balance for the artificial knee. Also, it could provide information in order to the surgeon perform corrections on the ligaments to restore some laxity characteristics similar to the natural intact knee [7]. Also a device that allows the determination of the soft-tissue biomechanical properties, such as ligament stiffness, can contribute a better understanding of the intrinsic mechanical behavior of the individual knee joint and benefiting the post-operative outcome [8].

To help improve ligament balance a number of techniques and devices have been developed for assessing soft-tissue stiffness (i.e. distractor, tenses, spacer blocks, trial components, electric instruments, and navigation system) [1, 7, 9–14] but, to the best of our knowledge, there are no TKA instrumentation that simultaneously allow a manual loading control by the surgeon while providing tibiofemoral force measurement and flexion-extension gap information. In fact, previous devices are either autonomous, making it impossible for the surgeon to experience a direct force feedback of the measurement, or they are manually controlled and provide rudimentary quantitative information.

This chapter is dedicated to describe the development and test of a smart

instrumentation for TKA. The approach is to expand the capabilities of a standard manual distractor provided by Symbios Orthopédie SA, currently used in orthopedic surgery, while maintaining the instrument shape and usage. The concept is based on the description of a similar tool used in human lumbar spine surgery [15]. The modified distractor allows the measurement of tibiofemoral forces and flexion-extension gaps during the TKA procedure, and estimation of ligament stiffness.

## 4.2 Materials and methods

The specifications of the device were defined in a collaboration with surgeons and consist of force measurement independent of the surgeon's hand position on the distractor and of the position of the applied load in the tip of the tool, displacement measurement ranging between 13 mm and 27 mm with accuracy of 0.1 mm and force assessment up to 500 N with accuracy of 2 N. The first specification provides the practitioner a freedom to operate, while maintaining the measurement reliability. The force and displacement accuracy are also important in order to provide measurements within expected readouts from the knee structure.

The distractor to be modified was provided by Symbios Orthopédie SA (Switzerland) and is part of the current instrumentation set provided to the hospitals to perform a TKA. The distractor's prototype is presented in Fig.4.1 and it is capable of continuous and real-time measurements of tibiofemoral forces and flexion-extension gaps. Our method for measuring tibiofemoral forces is to detect mechanical deformations in the distractor, and for measuring the flexion-extension gap, to track the distance between the tips of the distractor.

The detection of mechanical deformations is made by strain gauges. The strain gauge positioning on the distractor was chosen based on finite element analysis (FEA) performed with the current distractor's shape and material properties. Also, the position of the strain gauges was chosen to minimize the dependency of the force on the variable position of the hands of the surgeon on the distractor handles and on the position of the applied load in the tip of

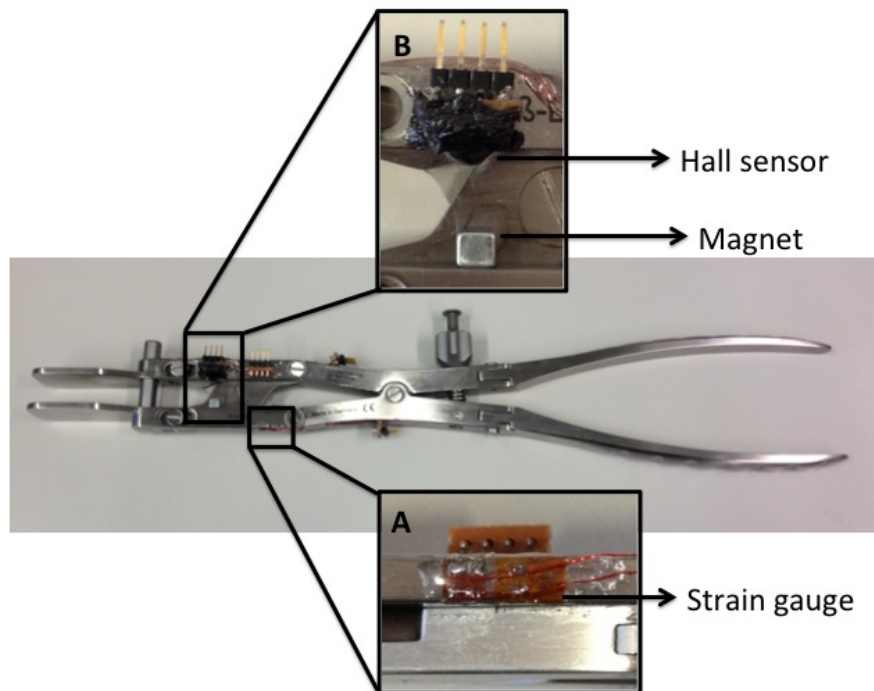


Figure 4.1: Instrumented distractor prototype capable of continuous and real-time measurements of (A) tibiofemoral forces and (B) flexion-extension gaps.

the tool (Fig.4.1A). The strain gauges are connected to a Wheatstone bridge in a half-bridge configuration (Fig. 2.9B). The half-bridge configuration is used to compensate for overall temperature drifts and its resistance is a standard  $120\ \Omega$ . The Wheatstone bridge is powered with 2.5 V and the output signal amplified using an instrumentation amplifier INA 114 (Texas Instruments).

In order to measure displacement an off-the-shelf Hall sensor (Asahi Kasei Microdevices Corporation, HW-322B) is positioned on one shaft of the instrument in front of a magnet positioned on another shaft on the opposite side (Fig.4.1B). The Hall sensor is powered with a transconductance amplifier which provides a constant current of 10 mA. This configuration was chosen to provide a reliable measurement of the Hall sensor signal output. The signal output is connected to another instrumentation amplifier INA 114. Both signals from the strain gauges and the Hall sensor are sampled to a computer with a National Instruments data acquisition board (NI-6259). For displaying real-time measurements a

LabView (National Instruments) interface was used.

The instrumented distractor calibration consists of a semi-automated procedure. The displacement sensor is calibrated after assembly to the distractor. It is performed once and the data saved to file which will be used to extract the coefficients based on a third order exponential decay curve fit. The strain sensors are initially calibrated using a load cell and afterwards, mainly due to drift, necessary corrections can be performed using shunt resistors. Shunt calibration is a standard method accepted throughout the industry as means of periodic calibration of signal conditioners and transducers. The signal conditioner's gain and span controls are set to obtain a full-scale electrical output signal. The shunt calibration procedure is short and simple but it must be performed before each surgical procedure to ensure the accuracy of the instrument and the measurements reliability.

Once the distractor is calibrated, it can be used for measurements. During the measurement, the surgeon can see the force and displacement values on the computer screen through the Labview interface. The surgeon can manually set the ligament balance with the help of his expertise and feeling as well as the displayed values. This manual control provides a safe surgical procedure since the measurement can be stopped at any time by the surgeon.

### 4.3 Results

In order to perform the calibrations and test of this device, the distractor tip (part will be in contact with the bones) was fixed to a bench such that the instrumented arm was free to be operated. The Hall sensor calibration was performed statically using a digital caliper fixed to the tip of the distractor while the signals were sampled to the computer. The calibration curve, distance measured by the caliper as a function of the voltage output of the Hall sensor, and the achieved fitting is shown in Fig.4.2. The fitting was performed with a third order exponential decay function (residual sum of squares = 0.0802 mm and adjusted R-square = 0.9998) and the extracted coefficients updated in the Labview algorithm for real-time calculation of the displacement. For large

displacements (average 25.3 mm) the standard deviation was  $1.6 \times 10^{-2}$  mm and for small displacements (average 15.3 mm) the standard deviation was  $2.9 \times 10^{-4}$  mm.

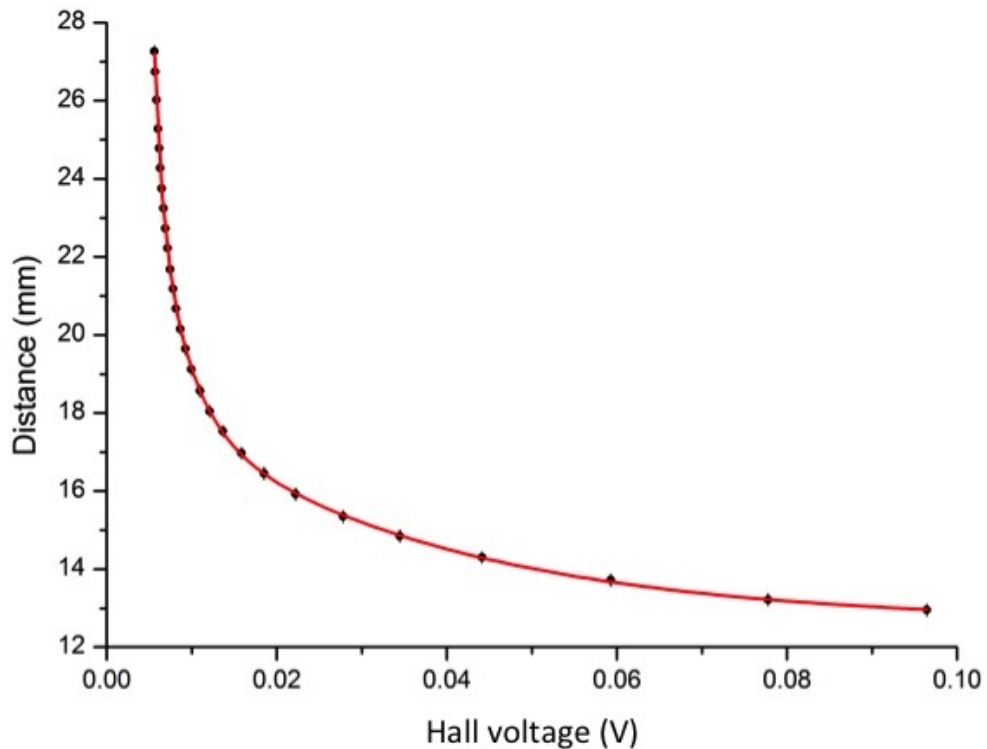


Figure 4.2: Data acquired for the static calibration of the Hall sensor represented by the dots and the third order exponential decay fit to the data represented by the line. The graph presents the distance as a function of the voltage output of the Hall sensor. Error bars are plotted, however they are not visible because it is within the size of the black dots.

The calibration of the strain gauges was performed statically with a load cell positioned at the tip of the distractor. The calibration curve, force output given by the load cell as a function of the voltage output of the Wheatstone bridge after amplification, and correspondent fitting is presented in Fig. 4.3. The fitting was performed with a linear function (residual sum of squares = 7.808 N and adjusted R-square = 0.9995) and the extracted coefficients also updated in Labview for automatically converting voltage into force. For small forces (average 36.3 N) and higher forces (average 399.5 N) the standard deviation was 1.13 N and 1.95 N, respectively. The precision of the measurement for both,

displacement and forces, are in accordance with the desired specification for the distractor.

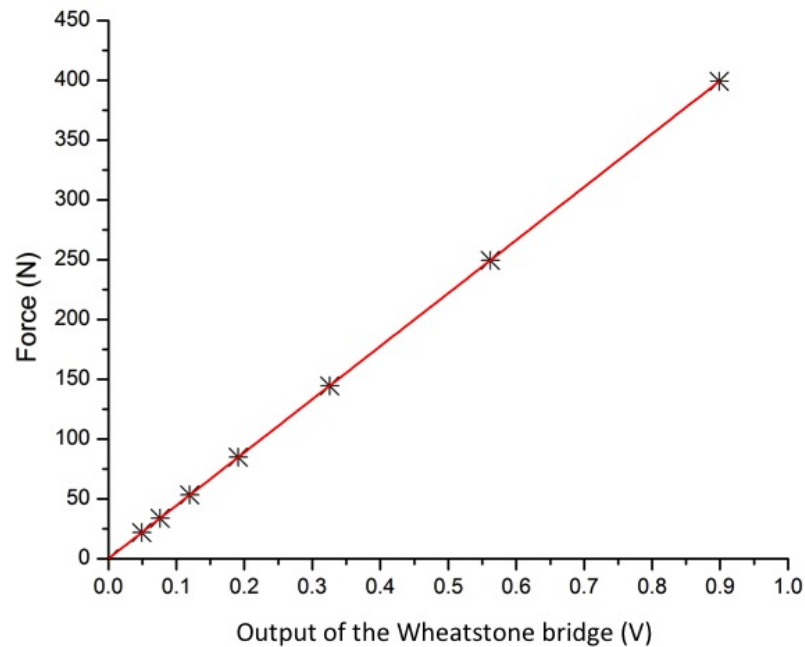


Figure 4.3: Data acquired for the calibration of the strain sensors to transduce the force represented by the star points and the correspondent linear regression to the data. The curve presents the Force as a function of the output of the Wheatstone bridge. Error bars are plotted, however they are not visible because it is within the size of the star points.

To assess the suitability of the device for the purpose of ligament balancing, a control experiment with a spring simulating the ligaments was performed. The spring (with a spring constant of 13 N/mm) was fixated to the tip of the distractor and a series of dynamic movements of opening and closing the instrument was completed. The measurement was repeated several times with the spring attached to the tip of the distractor to assure repeatability of the load readings. The measured displacement and forces are presented in Fig. 4.4 showing the force as a function of distance. As expected, when loading the instrument to distract the spring the force increases linearly with the distance, with a measured spring constant of  $13.1 \pm 0.34$  N/mm. The shift in the curve for unloading is a consequence of the mechanical friction imposed by the distractor

construction. Overall the measurements demonstrate the device suitability for estimating the force and distance and can assist surgeons when performing ligament balance during the TKA.

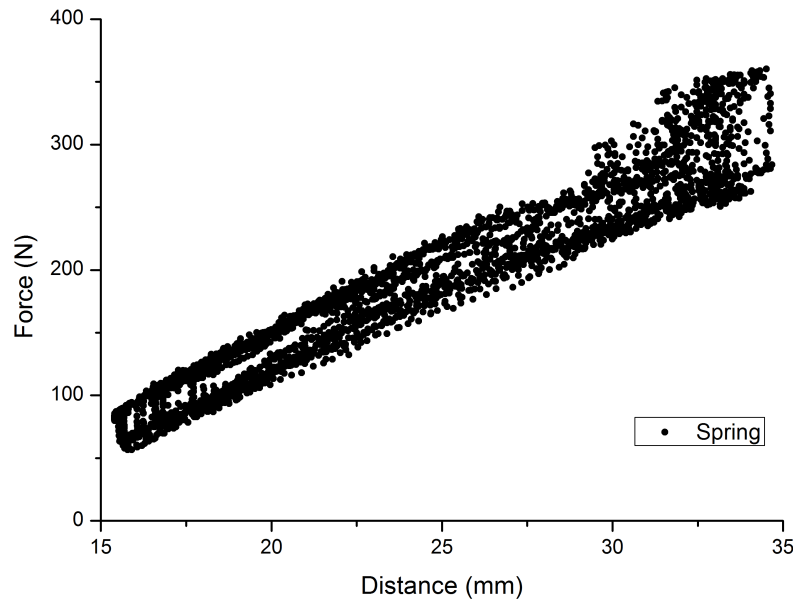


Figure 4.4: Control experiment with a spring attached to the tip of the distractor. The graph shows the force as a function of the distance.

### 4.3.1 *In vitro* measurements

After approval of the local ethical committee we were able to test the device *in vitro*, in two cadaveric legs. The goal was to prove the device concept and verify if the acquired parameters were in accordance with expected stiffness values for medial collateral ligament (MCL) and lateral collateral ligament (LCL). The measurement protocol consisted of distracting the MCL and LCL 7 to 10 consecutive times by controlling the loading and unloading rate while recording the force and distance. Fig. 4.5 shows the recorded signals, force and distance, as a function of time for one of the experiments. Each measurement was repeated 3 times for each compartment (medial and lateral) and took about 1 min.

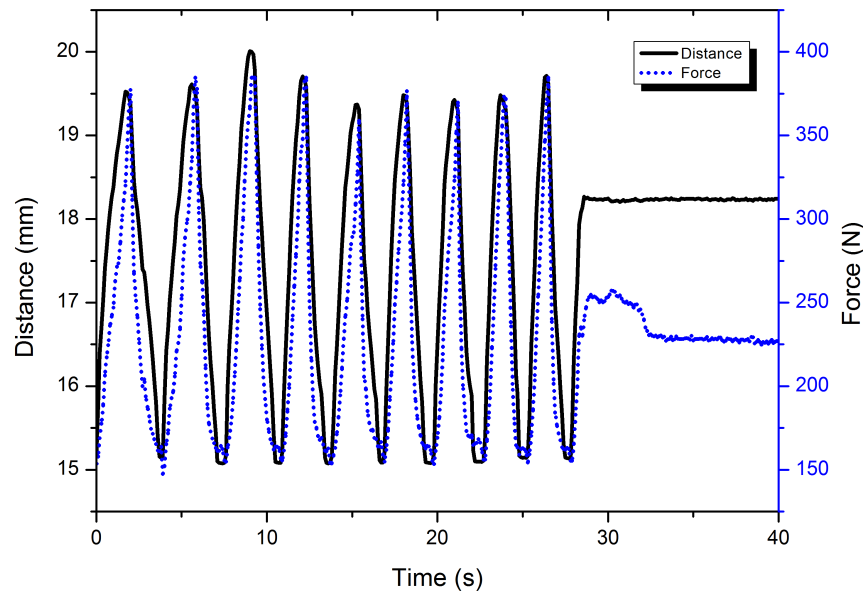


Figure 4.5: Experiment for determining the ligament stiffness which consists of recording the force and distance in a series of consecutive loading and unloading of the distractor. The graph presents the measured Forces and distances as a function of the time.

Two *ex vivo* measurements are presented in Fig. 4.6. The graph shows the force as a function of the distance for determining the stiffness of a MCL for the two cadaveric legs. The stiffness can be estimated by the slope of a linear regression fitting the data. The results from the *ex vivo* experiments to determine the ligament stiffness are summarized in Table 4.1 together with recently reported MCL and LCL stiffness [8]. They represent the average and standard deviation of three consecutive measurements performed in each compartment (medial and lateral) for the two cadaveric legs.

## 4.4 Discussions

In this application of MEMS to medical instrumentation we sought to provide a ligament balance tool to be used during TKA surgery. A commercially available TKA distractor has been instrumented with sensors to indicate distraction forces



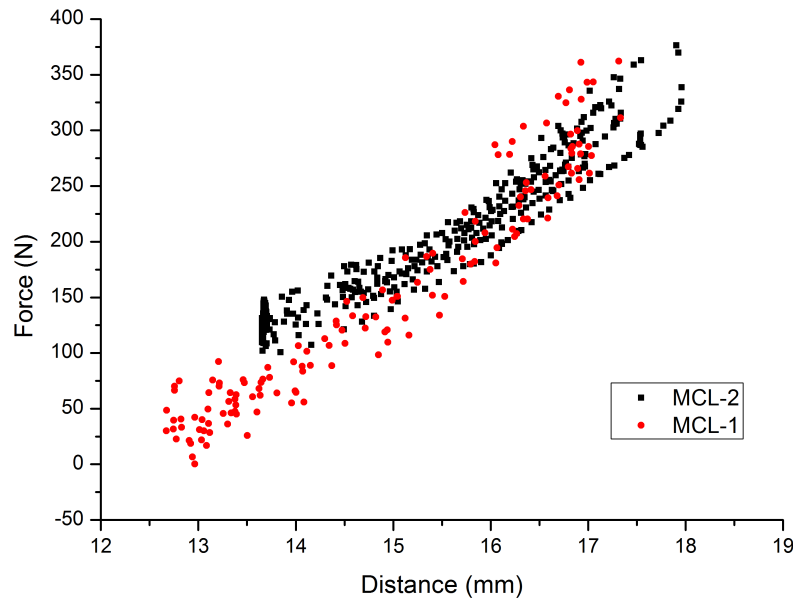


Figure 4.6: Results of two *ex vivo* experiment for determining MCL stiffness. The graph presents the Force as a function of the distance. The stiffness of the ligament can be estimated by the slope of a linear regression fitting the acquired data.

Table 4.1: Summary of the results from the two *ex vivo* experiments to determine the ligament stiffness and previous reported MCL and LCL stiffness [8].

Experiments	Ligament	Stiffness [N/mm]
Cadaveric leg 1	MCL	$62.7 \pm 1.37$
	LCL	$57.6 \pm 1.43$
Cadaveric leg 2	MCL	$47.5 \pm 2.29$
	LCL	$40.1 \pm 1.94$
Reported values [8]	MCL	$63 \pm 14$
	LCL	$59 \pm 12$

and displacement. TKA imposes significant demands on ligament balance to stabilize the artificial knee [6]. The difficulty in judging ligament balance and excessive tightness or release may lead to knee instability leading to abnormal motion that increase prosthesis wear and can result in early surgical revision [5]. In order to simulate the environment encountered by the surgeons we have

tested the device using spring to simulate the ligaments and characterized the distractor behavior during dynamic loading and unloading. Also the distractor was tested *ex vivo* in two cadaveric legs. The knee is a complex joint, and there are many factors that can affect the measurements, however the determined ligament stiffness are in accordance with recent studies performed in dissected medial collateral ligament (MCL) and lateral collateral ligament (LCL) [8]. The small discrepancy (smaller values of MCL and LCL) observed in Table 4.1 for the "cadaveric leg 2" is attributed to the storage conditions of this particular cadaveric leg. However, the values are still close to the lower boundary deviation expected for MCL and LCL ligament stiffness. We believe that the procedures followed during the *in vitro* tests do not differ significantly from what the surgeon will encounter during TKA.

There are several limitations in the current study, i.e. static calibration and shifts imposed by the mechanical friction, but results demonstrated that the distraction gap can be measured reliably and with 0.1 mm accuracy. The distractive loads could be assessed accurately in the range of 2 N, attending the desired surgeon specification for such device. Also, loads as high as 300 N can be measured and are within the linear range of the instrument. The ligament behavior of the knee can be quantified by measuring the tibiofemoral force in the medial and lateral ligaments. Despite the lack of a gold standard for ligament balance, meaning how strong the tension of soft-tissue in total knee arthroplasty is made with respect to the distraction, it would be very helpful if a set of numerical values could be determined that would serve as a reference for the appropriate soft-tissue balance in total knee replacement. Considering the errors, given by the manual operation of the distractor in the *ex vivo* experiments, it can be stated that the ligament stiffness could be assessed with good reliability. The developed tool provides surgeons with data to assist their intra-operative decisions and we believe it can help to improve the implantation technique to increase TKA post-operative results. Also, such tool can be of great help if introduced during training of young surgeons to improve their learning experience by having a quantitative feedback of their correspondent feeling.

Before being tested *in vivo*, we need to establish the measurement protocol and

test the robustness and durability of the device. Also the inclusion of a passive telemetry system is being studied which we believe will improve the usage of the device. We are also addressing technical issues of autoclave sterilization, storage and manufacturing costs.

## 4.5 Conclusion

Extending the capabilities of current available surgical instruments is a versatile and easy way to improve surgical outcome without changing surgical procedures or impose to surgeons new surgical techniques. In contrast with the existing ligament balance tools the developed instrumented distractor allows a manual loading control by the surgeon while providing both real-time measurements of tibiofemoral forces and flexion-extension gaps. The determination of ligament stiffness could also be achieved with good reliability. The quantification of such parameters can possibly contribute to validate the way surgeons implant prosthesis at the same time that it can provide useful *in vivo* information for a better understanding of the complex knee joint.

## 4.6 References

- [1] "Joint gap kinematics in posterior-stabilized total knee arthroplasty measured by a new tensor with the navigation system.," *Journal of Biomechanical Engineering*, vol. 128, pp. 867–871, Dec. 2006.
- [2] D. Crottet, T. Maeder, D. Fritschy, H. Bleuler, L.-p. Nolte, I. P. Pappas, and A. Modeling, "Device Designed to Improve the Ligament Balancing Procedure in TKA," *Evolution*, vol. 52, no. 9, pp. 1609–1611, 2005.
- [3] S. F. Attfield, M. Warren-Forward, T. Wilton, and a. Sambatakakis, "Measurement of soft tissue imbalance in total knee arthroplasty using electronic instrumentation.," *Medical Engineering & Physics*, vol. 16, pp. 501–505, Nov. 1994.
- [4] S. Almouahed, M. Gouriou, C. Hamitouche, E. Stindel, and C. Roux, "Design and evaluation of instrumented smart knee implant.," *IEEE Transactions on Biomedical Engineering*, vol. 58, pp. 971–982, Apr. 2011.
- [5] F. W. Werner, D. C. Ayers, L. P. Maletsky, and P. J. Rullkoetter, "The effect of valgus/varus malalignment on load distribution in total knee replacements.," *Journal of Biomechanics*, vol. 38, pp. 349–355, Feb. 2005.
- [6] A. Arami, M. Simoncini, O. Atasoy, W. Hasenkamp, S. Ali, A. Bertsch, E. Meurville, S. Tanner, H. Dejnabadi, V. Leclercq, P. Renaud, C. Dehollain, P.-A. Farine, B. M. Jolles, K. Aminian, and P. Ryser, "Instrumented prosthesis for knee implants monitoring," in *2011 IEEE International Conference on Automation Science and Engineering*, pp. 828–835, IEEE, Aug. 2011.
- [7] C. Marmignon, a. Leimnei, and P. Cinquin, "Robotized distraction device for knee replacement surgery," *International Congress Series*, vol. 1268, pp. 638–643, June 2004.
- [8] W. T. Wilson, A. H. Deakin, A. P. Payne, F. Picard, and S. C. Wearing, "Comparative Analysis of the Structural Properties of the Collateral Ligaments of the Human Knee.," *The Journal of Orthopaedic and Sports Physical Therapy*, Oct. 2011.
- [9] Y. In, S.-J. Kim, J.-M. Kim, Y.-K. Woo, N.-Y. Choi, and J.-W. Kang, "Agreements between different methods of gap balance estimation in cruciate-retaining total knee arthroplasty.," *Knee Surgery, Sports Traumatology, Arthroscopy : Official Journal of the ESSKA*, vol. 17, pp. 60–64, Jan. 2009.
- [10] T. Takahashi, Y. Wada, and H. Yamamoto, "Soft-tissue balancing with pressure distribution during total knee arthroplasty.," *The Journal of Bone and Joint Surgery. British volume*, vol. 79, pp. 235–239, Mar. 1997.

- [11] T. Skrinskas, D. Viskontas, and L. Ferreira, "Application of an Intra-operative Load Measuring System for Knee Replacement Surgery," *Medical Image Computing and Computer-Assisted Intervention - MICCAI 2003*, pp. 246–253, 2003.
- [12] D. G. Viskontas, T. V. Skrinskas, J. a. Johnson, G. J. King, M. J. Wine-maker, and D. G. Chess, "Computer-assisted gap equalization in total knee arthroplasty," *The Journal of Arthroplasty*, vol. 22, pp. 334–342, Apr. 2007.
- [13] J. Bellemans, M. Ries, and J. Victor, *Total Knee Arthroplasty: A Guide to Get Better Performance*. Springer, 2005.
- [14] S. Rupp and D. Kohn, "Das besondere Instrument Der so genannte Knee Balancer," *Operative Orthopädie und Traumatologie*, vol. 60, no. Heft 3, pp. 256–260, 2000.
- [15] S. Ambrosetti-Giudici, A. Pfenniger, M. H. Krenn, W. P. Piotrowski, S. J. Ferguson, and J. Burger, "Surgical instrumentation for the in vivo determination of human lumbar spinal segment stiffness and viscoelasticity," *Medical Engineering & Physics*, vol. 31, pp. 1063–1068, Nov. 2009.

## Strain Sensors for Knee Prosthesis

*This Chapter is based on the following article:*

*W. Hasenkamp, et. al.,  
"Design and Test of a MEMS Strain-Sensing Device for Monitoring  
Artificial Knee Implants",  
Biomedical Microdevices (submitted).*

*Never leave that till tomorrow  
which you can do today.  
- Benjamin Franklin*

## 5.1 Introduction

The knee is a complex joint that is difficult to model accurately, however mathematical models are commonly used as initial screening tools for evaluating the prosthesis design. Finite Element Analysis (FEA) is the most frequently used technique to evaluate the artificial implants, mainly to investigate the influence of load application and identify fragile regions to avoid premature prosthesis failure [1]. If FEA contributes to extend the life of the orthopedic implant other factors significantly impact on the prosthesis lifetime. Several different artificial knee implant designs are commercially available but misalignment, leading to knee imbalance, and wearing are still the major reasons for revision. Forces acting directly on the artificial joint affect the knee balance and induce wear of the bearing surface, which is associated to prosthesis loosening, consequently impacting on the implant lifetime [2].

One of the most affected components of the artificial knee implant is the ultra-high-molecular-weight polyethylene (UHMWPE) insert, due to its geometry and the high forces acting upon it [3]. Therefore monitoring the strain, associated to knee imbalance and forces acting upon the prosthesis, can help on the development of new articulating components, lead to a better understanding of the artificial knee biomechanics, support improvements on the mathematical models that describes the constitutive model of the materials and the knee behavior, improve prosthesis alignment during surgery and give continuous feedback on the status of the artificial knee implant.

Valuable efforts have been made to design implantable systems for monitoring biomedical implants, either using strain gauges, fiber Bragg gratings or Tekscan sensing systems [4–7]. Though the systems have their specific advantages many require alterations of the current prosthesis designs or can only be used during surgery not being suitable for implantation. To overcome these limitations sensors can be fabricated using biocompatible materials, such as polyimide, and embedded into the polyethylene insert without introducing design changes [8, 9]. Polymer-based microelectromechanical systems (MEMS) are increasingly being used in biomedical applications [10] and, recently, micro-

machined polyimide sensors have been used as sensing elements in a broad range of biomedical applications, e.g. deep brain recording and stimulation [11] and contact lens pressure sensors for glaucoma [12].

In this chapter we present a versatile MEMS strain-sensing device for the monitoring of loads acting upon an artificial knee implants, at the level of the UHMWPE insert. The goal of evaluating the strain is to help surgeons on the alignment of prosthesis, which can improve the knee balance and provide a follow-up tool to help monitoring the artificial knee along its lifetime assuring the overall integrity of the prosthetic limb. Likewise, the strain monitoring, which is associated to loads acting upon the prosthesis, can lead to a better understanding of the artificial knee biomechanics and help in the development of new generation of implants. Moreover, the continuous monitoring of the strain evolution can be used to track the wear of the UHMWPE insert. The basic design and working principle of the sensors are presented as well as results of the preliminary bench tests. The manufacturing process is based on polyimide micro-machining, which allows to adapt the shape and design of the micro-devices. The sensors are based on polyimide-metal-polyimide sandwich structures that are embedded into the UHMWPE part.

## 5.2 Finite element analysis

Finite Element Analysis (FEA) is an effective tool to investigate the distribution of the stress and strain in various kinds of engineering structures [13]. In this article, FEA was used to investigate the distribution of strain in an artificial knee implant and assist on the strain gauges placement inside the ultra-high-molecular-weight polyethylene insert (UHMWPE). The Computer Aided Design (CAD) model was obtained from the manufacturer of an artificial knee, Symbios Orthopédie SA (Yverdon-Les-Bains, Switzerland), and the 3D finite element model built into a commercial FEA software, COMSOL Multiphysics (v4.2). The components of the CAD model are presented in Fig. 5.1, and comprise the femoral component (FC), the UHMWPE insert, the tibial component (TC) and the guide pin. The location of the strain sensors in a cross-sectioned UHMWPE insert is also depicted in Fig. 5.1. The original CAD description of the prosthesis



is overly complicated, therefore simplifications were made to generate a 3D model suitable for computing. The simplified 3D model is sketched in Fig. 5.2.

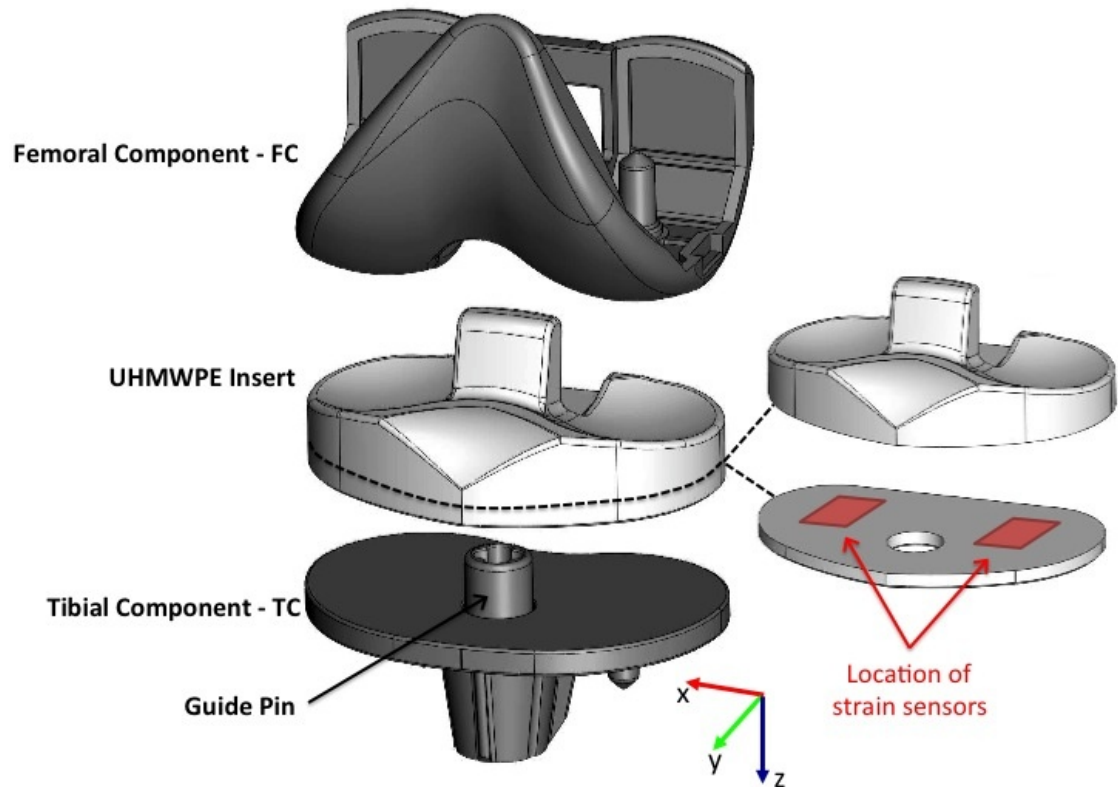


Figure 5.1: Components of the CAD model comprising the femoral component (FC), the UHMWPE insert, the tibial component (TC) and the guide pin, and a UHMWPE insert cross-section depicting the location of the strain sensors.

FEA was modeled in the structural mechanics module of COMSOL in stationary mode assuming a linear elastic behavior for all parts. The fundamental considerations of this approach are to assume a small strain (or stress) and the linear relationship between components stress/strain (i.e. Young's modulus). The material properties (Young's modulus  $E$  and Poisson constant  $\nu$ ) used in the FEA are the following: for the FC and TC (made of a Co-Cr-Mo alloy)  $E = 115$  GPa,  $\nu = 0.3$ , and for the UHMWPE  $E = 0.34$  GPa,  $\nu = 0.4$ .

To establish boundary conditions for the simulation the following constraints were added to the model. Between the FC and the UHMWPE insert a contact interface is established. A surface constraint is defined on the guide pin hole to keep the alignment between the UHMWPE insert and the TC. Boundary

condition uniaxial loads acting on the prosthesis were applied to the upper flat area of the FC, in the z-axis direction, varying from 200 N up to 3100 N, and defined as such to be in accordance with the biomechanical conditions in the human body. To complete the model, a fixed constraint is defined at the bottom surface of part of the TC to avoid overall implant displacement which can introduce discrepancies in the simulations. Unstructured progressive triangular meshing algorithm, to form tetrahedral elements, was utilized for meshing the model. The minimum and maximum element size was defined as 0.1 mm and 1 mm, respectively. The meshed structure consisted of 116933 tetrahedron elements and the convergence criteria for simulations was established by a MUMPS solver. FEA was used to investigate the distribution of strain inside the UHMWPE insert and to identify regions for placement of strain gauges sensors. In order to comply with implant regulatory standards the sensors where placed in the xy-plane at 6 mm from the FC/UHMWPE bearing surface (refer to Fig. 5.1).

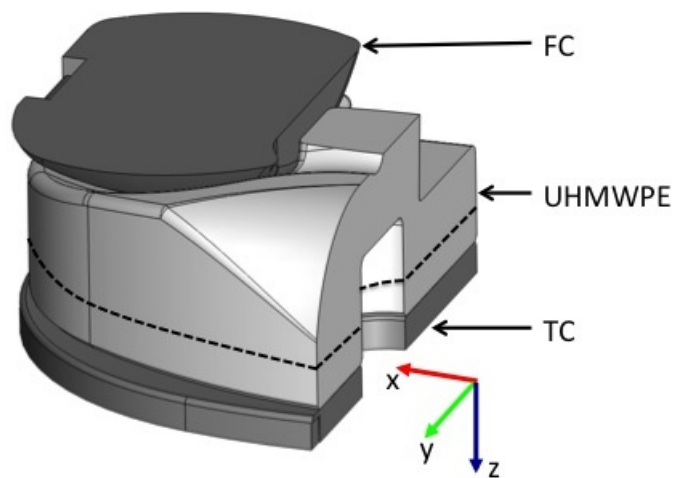


Figure 5.2: Simplified 3D CAD model used in the FEA.

### 5.3 Results of finite element analysis

Fig. 5.3 shows the evolution of the x-component strain, in the previously defined xy-plane (at 6 mm from the FC/UHMWPE bearing surface), for different applied loads. Highly positive strain values, associated with tensile strain in the x-axis direction, are visible under the contact points of the FC/UHMWPE bearing

surface. Negative strain values, associated with compressive strain in the x-axis direction are also visible on the surroundings of the tensile region. Moreover, from this investigation we could identify a xz-plane with good strain symmetry at nearly 1/3 of the UHMWPE height (14 mm), therefore these region is suitable for positioning the sensors.

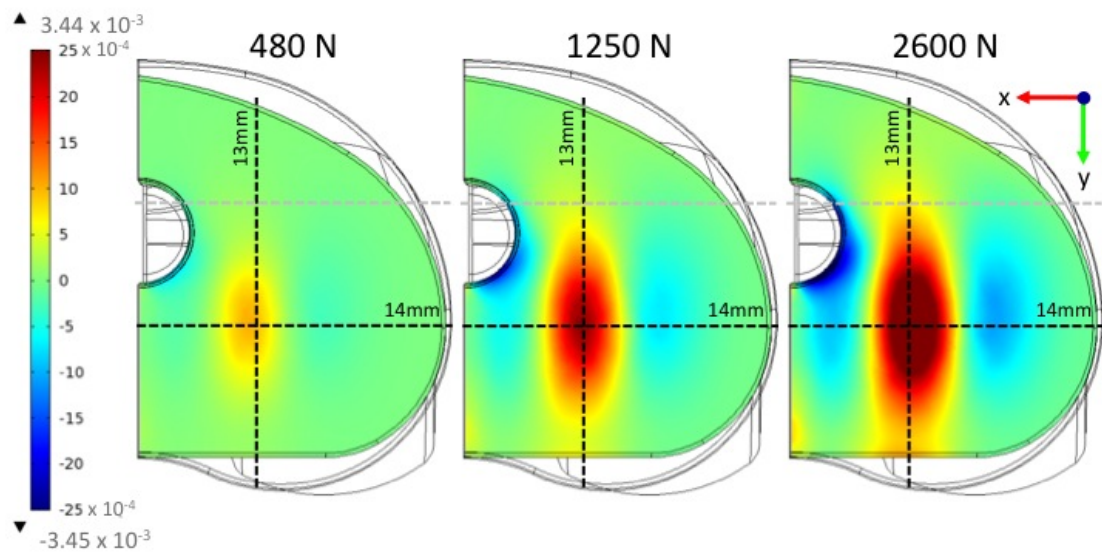


Figure 5.3: Evolution of the x-component strain, in the xy-plane at 6 mm from the FC/UHMWPE bearing surface, for different applied loads.

At the intersection between the defined xy- and xz-plane a line is defined and used to position and orient the strain sensors. Fig. 5.4 presents the evolution of the x-component strain at the intersection of xy- and xz-planes, along the UHMWPE width, for different applied loads. The insert in Fig. 5.4 shows the line of intersection between the xy- and xz-planes where the strain values were taken. Highly compressive strain is visible in a region that extends roughly for 6 mm, having its maximum nearly 13 mm along the UHMWPE width. Therefore, the strain sensors were defined to be located in the compressive

strain region with their center located at 13 mm along the UHMWPE insert width, while passive strain sensors were located in regions of zero strain to compensate for overall temperature variations.

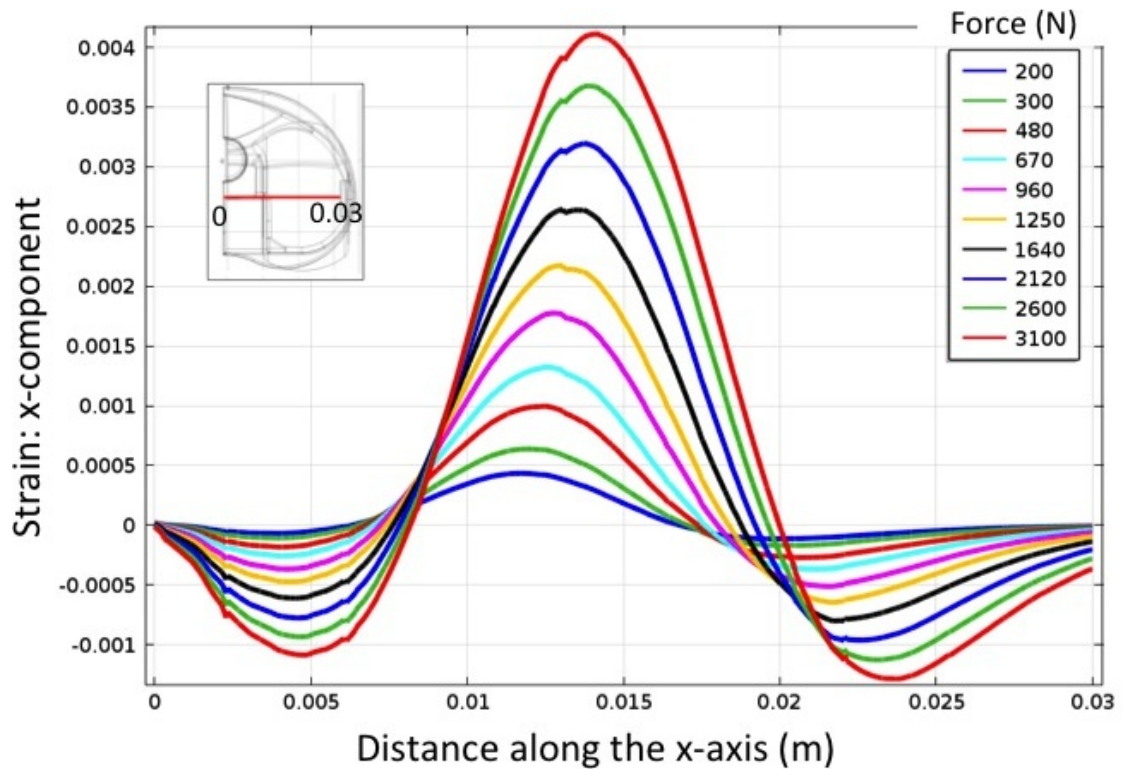


Figure 5.4: Evolution of the x-component strain at the line of intersection between the xy- and the xz-planes, along the UHMWPE width, for different applied loads.

## 5.4 Sensor design, fabrication and packaging

The strain sensors resistance was defined to be 3.2 k $\Omega$  in order to decrease power consumption and facilitate readout by the Sensimed wireless telemetry chip. The strain sensors to be embedded into the UHMWPE were built in polyimide-metal-polyimide sandwich structures by dry etching, using standard photolithography manufacturing processes. Polyimide (PI) is an excellent material for biomedical microdevices due to its chemical and thermal stability, low water uptake and biocompatibility [14]. Such PI properties are crucial because the sensors are placed under bearing surfaces which are prone to wear

and it will not risk patients health. Furthermore, PI is widely used in MEMS devices, therefore suitable for mass production. The total thickness of the sensor is about  $10\ \mu\text{m}$ . A cross-sectional view of the microfabrication process is presented in Fig. 5.5.

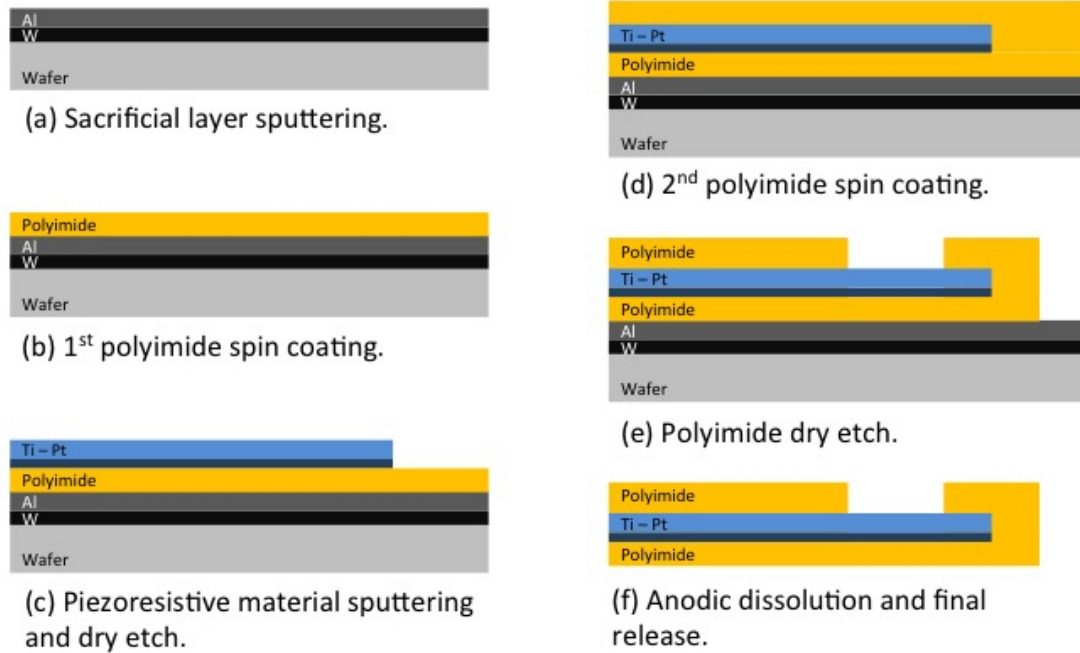


Figure 5.5: Cross section view of the fabrication process.

The detailed microfabrication process comprises the following steps: A sacrificial layer of tungsten ( $100\ \text{nm}$ ) and aluminum ( $1\ \mu\text{m}$ ) is first deposited through thermal evaporation onto a carrier silicon wafer (Fig. 5.5(a)). A  $5\ \mu\text{m}$  layer of PI (PI2611, HD Microsystems) is applied on top of the aluminum by spin-coating and cured at  $300\ ^\circ\text{C}$  for 1 h in nitrogen atmosphere (Fig. 5.5(b)). A titanium adhesion layer ( $20\ \text{nm}$ ) and platinum layer ( $180\ \text{nm}$ ) are then sputtered onto the cured polyimide. The strain gauges are patterned by reactive ion etching in  $\text{Cl}_2$  using a patterned photoresist as an etch mask (Fig. 5.5(c)). A second layer of PI,  $5\ \mu\text{m}$  in thickness, is spin-coated and likewise cured (Fig. 5.5(d)). An etch mask of sputtered  $\text{SiO}_2$  ( $500\ \text{nm}$ ) is deposited onto the sandwich structure and then patterned by reactive ion etching using a photoresist etch mask. This oxide layer is then used as hard mask during the subsequent oxygen-plasma etch of the polyimide to define both the structure outline and open contact

pads to the strain gauges (Fig. 5.5(e)). The polyimide devices are detached from the silicon carrier wafer by anodic metal dissolution in a 10 wt% sodium chloride solution: the substrates are immersed in the salt solution at room temperature with a platinum counter electrode, and a constant positive potential (0.7 V) is applied to the aluminum layer. The anodic metal dissolution process dissolved the aluminum, leaving the tungsten on the substrate and releasing the polyimide-metal-polyimide structures (Fig. 5.5(f)).

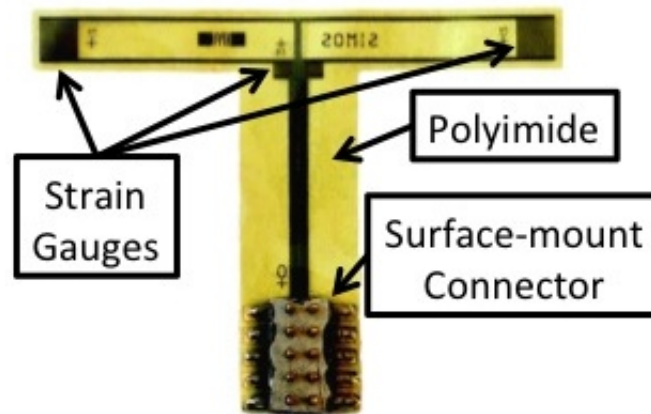


Figure 5.6: Polyimide-metal-polyimide micro-machined structure.

The packaging of the device consists of bonding a surface-mount connector (Samtec, Inc.) to the contact pads using a conductive epoxy. The connector provides the link between the strain gauges and the electronic circuitry. Despite the fact that the utilization of a connector prevents the usage of this device *in vivo*, the technology versatility allows for design changes without prejudicing the device feasibility. A fabricated polyimide-metal-polyimide structure is shown in Fig. 5.6. It consists of four strain gauges, two active gauges positioned (according simulation results) under the contact bearing surfaces, and two passive gauges towards the center of the artificial knee in regions of zero stain (according simulations).

To complete the fully packaged strain-sensing device the sensors are embedded into the UHMWPE insert. For that, the UHMWPE insert is sectioned in two parts, the polyimide-metal-polyimide sandwich is positioned, and the UHMWPE parts re-joined and sealed using a biocompatible epoxy glue. A

cross-sectioned UHMWPE insert with the strain sensors positioned for final assembly is presented in Fig. 5.7A and the complete packaged device is shown in Fig. 5.7B. The packaged device is capable of continuous real-time measurement. The built strain-sensing devices are versatile, simple, cost effective, and are ready to be integrated with implantable wireless telemetry, which can increase monitoring efficiency outside healthcare facilities.

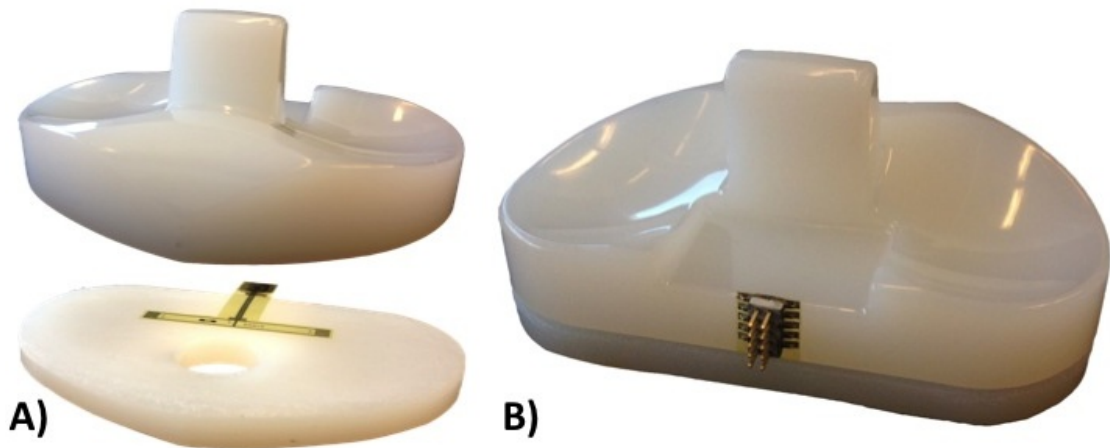


Figure 5.7: (A) A cross-sectioned UHMWPE insert with the strain sensors positioned for final assembly and (B) the complete packaged device re-joined and sealed using a biocompatible epoxy glue.

## 5.5 Experimental setup and results

The experimental study was carried out in a mechanical knee simulator (MTS Bionix Servohydraulic Test Systems). The tests were performed using static and dynamic axial load conditions (perpendicular to the referred xy-plane) similar to those encountered *in vivo*. The strain-sensing device is attached to the knee simulator and subjected to loads varying from 200 N up to 3100 N. The applied forces are close-loop controlled by a load cell, attached underneath the strain-sensing device, and connected to the knee simulator controller.

The fully packaged strain-sensing device is connected in a Wheatstone bridge configuration using external standard resistors with similar impedance to those in the polyimide-metal-polyimide sandwich. The bridge is DC powered with

2.5 V. The output signals are recorded with a National Instruments acquisition board (NI-Daqqad-6015) through a signal conditioning unit (SC-2345) connected to a full-bridge input channel (SCC-SG04). For displaying and recording the measurements a LabView (National Instruments) interface is configured. The signal conditioner's gain and span controls for the strain-sensing devices are set to obtain a full-scale electrical output signals.

Results for the identification (fitting) of parameters of the strain-sensing device are presented in Fig. 5.8. The curve presents both the expected strain (simulated x-component strain) and the measured strain as a functions of applied loads. The measured strain was calculated from the output voltage of the Wheatstone bridge, according the equation presented in Fig. 2.9B, being the input voltage 2.5 V and the gauge factor 2. These results indicate that the measured strain is in accordance with the simulated strain, and that applied forces can be estimated from measured strain. Therefore, validating the results obtained from the numerical model. Despite the overall non-linear behavior of the device, the measured data presents a linear region within forces varying from 0 N up to 1500 N. This is the range of forces exerted upon the knee during normal walking activities. A linear regression in this range of forces (from 0 N to 1500 N) indicates an average device sensitivity of  $2.4 \mu\text{V}/\text{N}$  (adjusted R-square = 0.99).

Tests of the assembled device were also carried out dynamically. Fig. 5.9 shows a series of slow (Fig. 5.9A) and fast (Fig. 5.9B) dynamic loading/unloading and the sensor's output as a function of time. The influence of the UHMWPE viscoelastic behavior on the measurements can be verified in Fig. 5.9A, where non-linearities, i.e. creep, can be observed in the measurements. Creep has an undeniable influence on the repeatability of the measurements affecting device accuracy in long-term measurements. A good sensor response to fast dynamic loading can be verified in Fig. 5.9B, thus allowing the sensor to be used for measuring knee forces during walking.



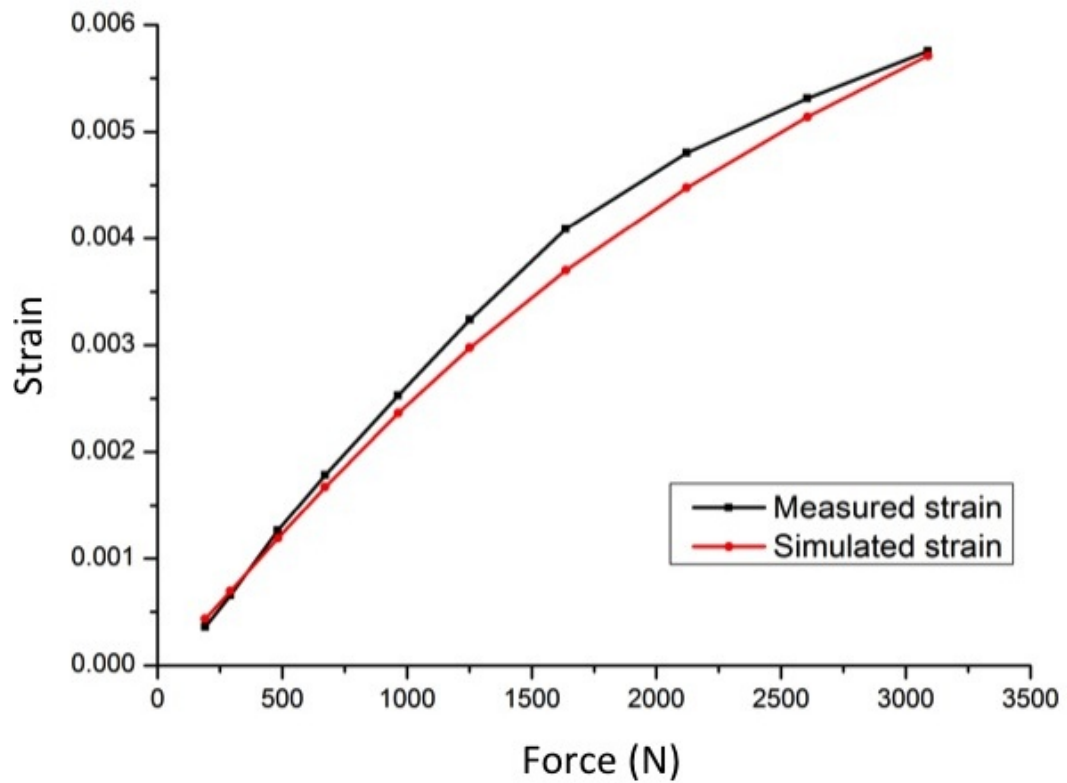


Figure 5.8: Simulated x-component strain and measured strain as a functions of applied loads.

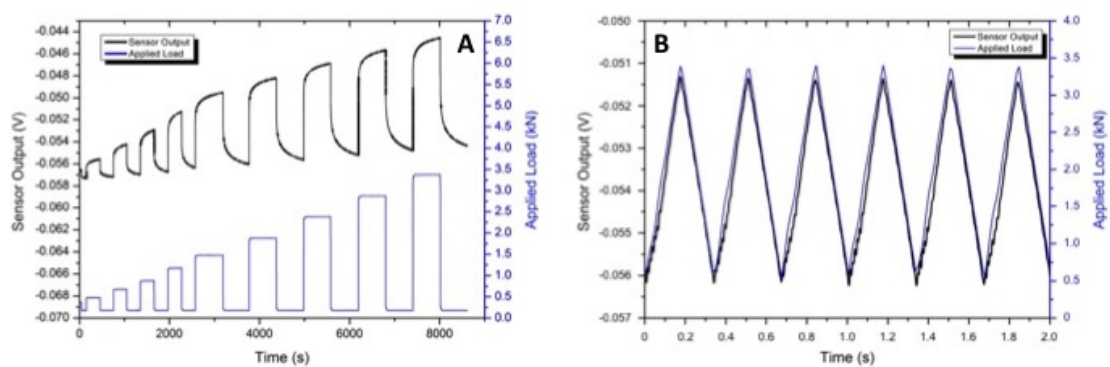


Figure 5.9: Series of slow (A) and fast (B) dynamic loading/unloading and respective sensor's output as a function of time.

## 5.6 Viscoelasticity and Creep

Viscoelasticity is the study of materials with mechanical characteristics of both solid and fluid materials, and as such it implies that its properties are function of time, with the material possessing a "memory" of past events [15]. A Viscoelastic material exhibit time dependent strain, since it has elements of both elasticity and viscosity. The elasticity (in an ordered solid) is usually the result of the elongation of chemical bonds along the crystallographic planes. The viscosity, whereas, can be defined as a result of the diffusion of atoms or molecules inside an amorphous material.

These materials can be modeled to establish their stress or strain behavior, and time dependency. These models are used to estimate a material's reaction under a variety of loading conditions. The most employed models are: the Maxwell model, the Kelvin-Voigt model, and the Standard Linear Solid (SLS) Model [16]. In Fig. 5.10 we present these models with it respective constitutive equations. In these models the viscoelastic behavior is represented as a linear combinations of springs and dashpots. The springs represents the elastic component while the dashpots represents the viscous components of the model. Each model is different in the arrangement of the components and can be represented by an equivalently electrical circuits. Stress is represented by voltage, while the derivative of strain by current. The springs are represented by capacitors, since it stores and restores energy, while the dashpots are represented by resistors, since it dissipates energy. By analogy the elastic modulus of a spring is equivalent to the capacitance of the circuit, while the viscosity of a dashpot is equivalent to the resistivity.

The most widely used among these models is the SLS model because it can describe stress relaxation and creep behavior. In this approach the springs represents deformations due to bending and stretching of intermolecular bonds, and the dashpot represents deformation due to viscous effect. In the SLS model, the total stress is decomposed into rate dependent stress component in the spring  $E_2$  and the dashpot  $\eta$ , and rate independent equilibrium stress in the spring  $E_1$ . The governing equation for the total stress in the SLS can

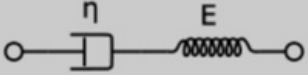
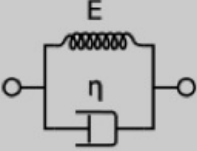
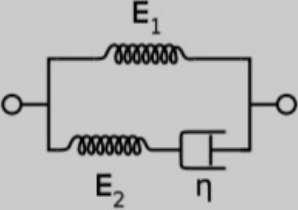
Maxwell Model	Kelvin-Voigt Model	Standard Linear Solid Model
		
$\frac{d\epsilon_{Total}}{dt} = \frac{d\epsilon_D}{dt} + \frac{d\epsilon_S}{dt} = \frac{\sigma}{\eta} + \frac{1}{E} \frac{d\sigma}{dt}$	$\sigma(t) = E\epsilon(t) + \eta \frac{d\epsilon(t)}{dt}$	$\frac{d\epsilon}{dt} = \frac{\frac{E_2}{\eta} \left( \frac{\eta}{E_2} \frac{d\sigma}{dt} + \sigma - E_1\epsilon \right)}{E_1 + E_2}$

Figure 5.10: Most common viscoelastic models employed to predict material's response under different loading conditions [16].

be solved to define the stress-strain relationship at constant strain rate where creep and stress relaxation can be modeled. Despite this approach provides a model for the behavior of viscoelastic material its application to dynamic systems is cumbersome and analytical relationships are preferred. For the case of many plastics the creep and stress relaxation behavior is subject to an empirical approach employing the following equation:

$$\epsilon(t) = \epsilon_0 + m * t^n \quad (5.1)$$

where  $\epsilon_0$  is the instantaneous strain and,  $m$  and  $n$  are material constants which depends on the applied stress.

In our experiments with the strain gauge sensors embedded in the UHMWPE, when applying a static force, a drift of the recorded values is observed over time and a similar behavior appears when releasing the force, affecting the measurements. In Fig. 5.11 and 5.12 we present the response over time when applying and releasing forces on the implant, respectively, showing the necessity to model these phenomena in order to gain insight on the behavior of the strain sensors inside the UHMWPE insert.

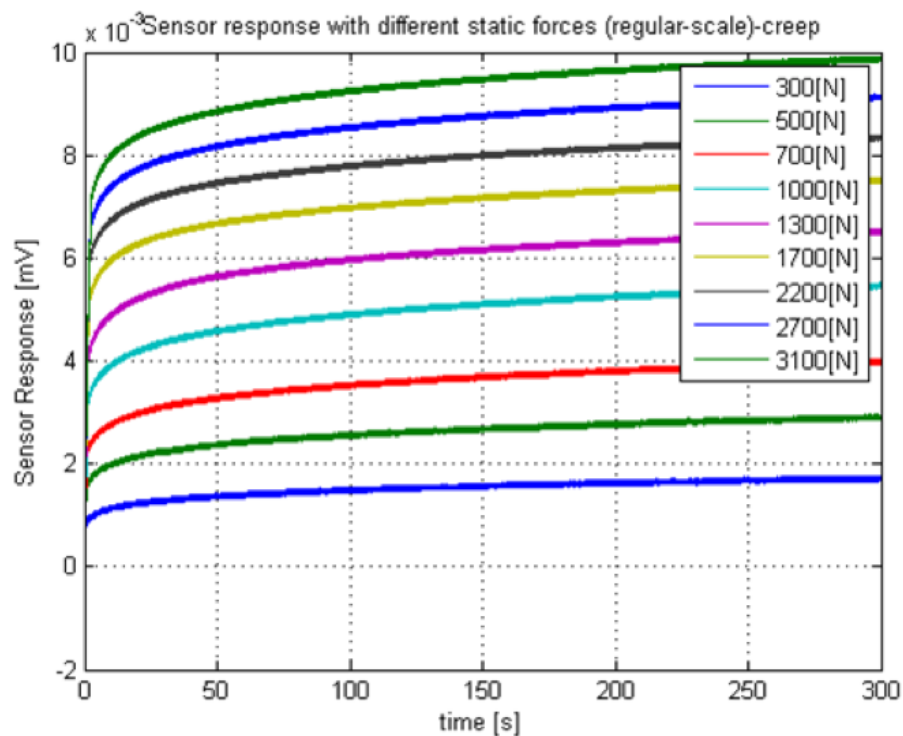


Figure 5.11: Sensor's response over time for several constant forces applied.

A first attempt to model this creep and relaxation, is to assume that the sensor response and the creep or relaxation can be separated in two phases, the immediate sensor response due to the application or the release of the force, and the creep or stress relaxation. The goal would be to fit the creep and stress relaxation part for each force and therefore being able to build a model to remove it. The point that identifies the transition between the two phases is selected manually and a step function for the force is assumed to be the input. This procedure must be followed because the MTS Load frame is not able to generate this kind of ideal patterns. The hydraulic actuator is relatively slow

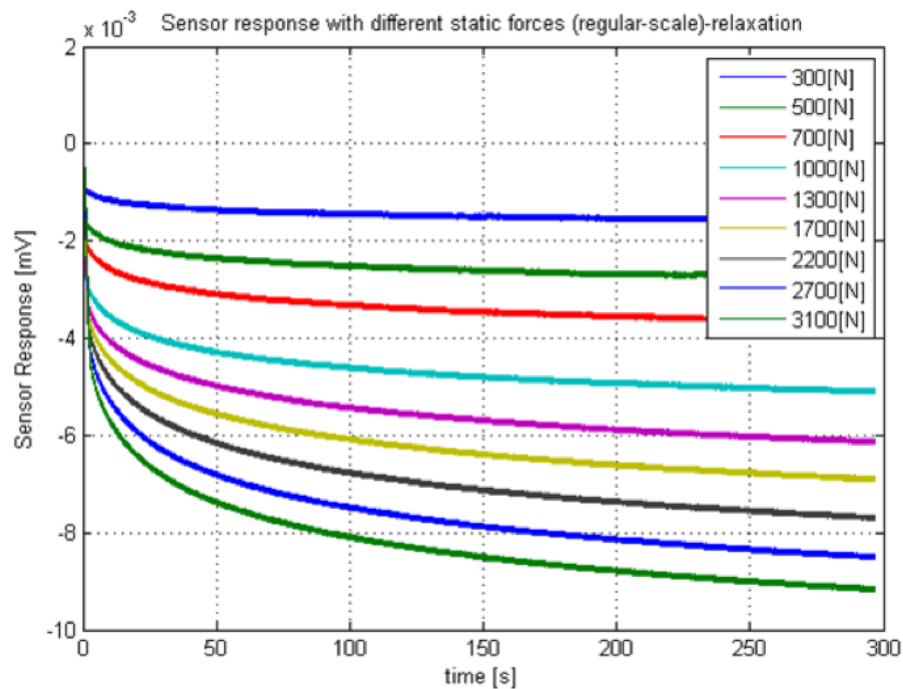


Figure 5.12: Sensor's response over time when the applied constant forces are released.

and the PID controller is a trade-off between decreasing the time response of the output and avoiding side effects such as overshoots of the signal or loss of stability.

For modeling this creep and stress relaxation, the curves presented in Fig. 5.11 and 5.12 are fitted with a power function ( $f(x) = a * x^b$ ), according to recent work by H. Liu *et. al.* [17], therefore following a traditional empirical approach. Using the power function model the evolution of the parameters "a" and "b" as a function of the force is shown for creep and stress relaxation in Fig. 5.13.

The model presented for fitting the creep and stress relaxation signals provides an initial approach towards understanding creep and stress relaxation on the knee implants. It is difficult to build an accurate and reliable model using this approach, at least with the experimental set-up used. The ideal goal would be to compensate on-line the effect of the creep and relaxation. However, the main issue for performing an on-line compensation is that the model for creep and stress relaxation is self-dependent, meaning it is dependent on the applied

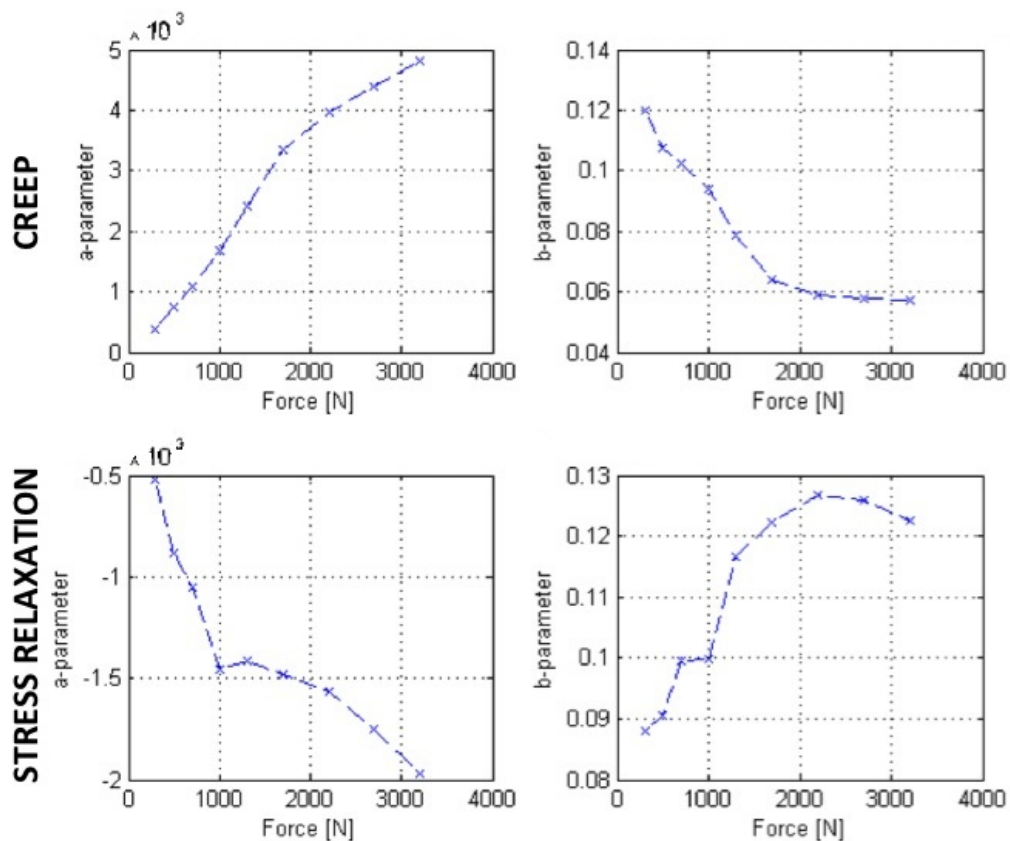


Figure 5.13: Evolution of the fitting parameters "a" and "b", for both creep and stress relaxation, as a function of the force.

force which has to be measured. Moreover, creep and stress relaxation are dependent on the history of the forces which were previously applied on the material. Furthermore, if a small error is computed using the model it will be propagated over time making the predictions unreliable. The future work is to explore more complex models to model creep and stress relaxation. These models should be then tested on new recordings to be validate as well as the setup needs to be modified.

To analyze the influence of the creep on the measurements the experimental creep curve was extracted from the data. Fig. 5.14 shows the experimental creep curves for different loading levels. The creep is plotted versus the logarithm of time. The experimental curves indicates the creep is dependent on the applied load as well as on the time. When analyzing Fig. 5.14 we are able to determine the proposed sensor is accurate for measuring events happening within a

1s time window, with errors below 8% the applied load. For measurements lasting 10s and 100s the creep introduces substantial drift on the measurement, respectively, 38% and 85% the applied load. However, in slow pace walking a single load cycle is within a 1s time window, therefore in gait studies it is important to monitor events happening below a 0.1s time window, region where errors are below 3%.

The developed device has thus the potential to measure *in vivo* activity and help to improve TKA surgery and postoperative follow-up. In TKA surgery the device can be used to assist in the ligament balance, which is currently only qualitatively assessed, and is crucial for the stability and lifetime of implants. During the postoperative physical therapy the device can provide information regarding the artificial knee implant function and help to improve overall rehabilitation and treatment of patients with total knee implants.

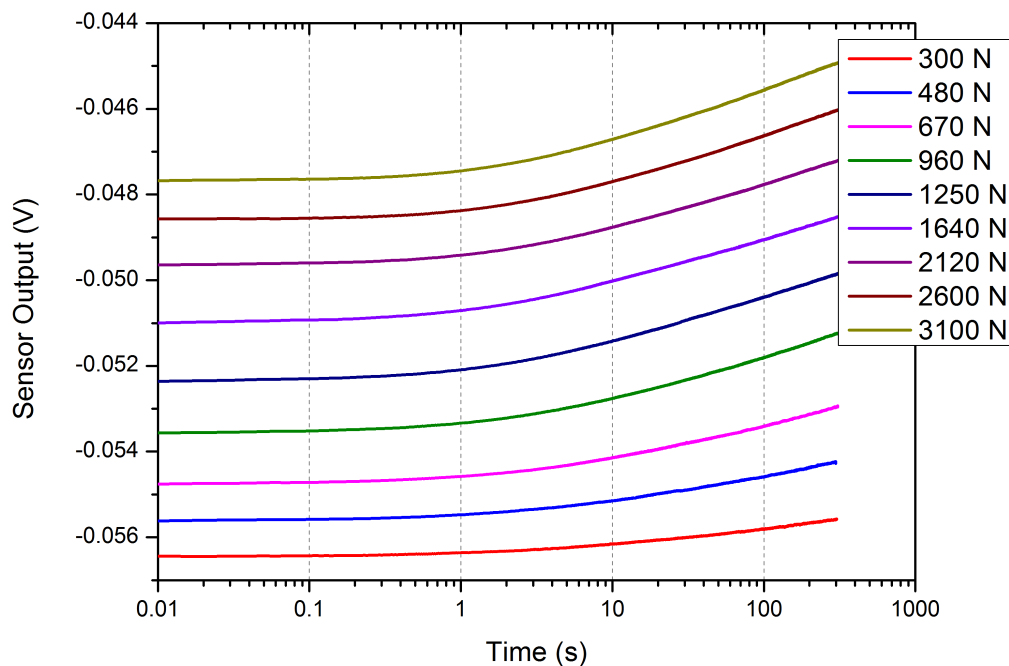


Figure 5.14: Experimental creep curves for different loading levels versus the logarithm of time.

## 5.7 Discussion

In this chapter, a polymer-based strain-sensing device was developed for monitoring an artificial knee implant. The experimental data demonstrates the sensor is capable of measuring the strain associated to the total axial forces exerted on the UHMWPE insert in the range of approximately 4 times body weight with a good sensitivity and accuracy for events happening within 1s time window. This device has been designed to monitor the total load and simple alterations on the strain-sensor design can allow the measurements of forces in each individual compartment of the UHMWPE insert, allowing for the monitoring of instantaneous artificial knee balance. Other alterations can also be made in the design to allow the measurement of other force components (e.g. momentum) and temperature monitoring, to investigate the effect of different activities, such as walking and cycling, on the implant wear rate. Improvements on the sensors design and packaging, as well as increasing the number of strain-sensors on the device can allow the mapping of strain in other regions of interest in the UHMWPE.

Although, *in vivo* measurements of the knee joint forces are broadly available, very little is known on the evolution of artificial knee implants after TKA and the aging of such prosthesis, hence the proposed device will allow studies of biomechanics on the prosthetic knee and improve implant design. The results demonstrated that the proposed strain-sensor represents a promising new system for *in vivo* load monitoring of medical implants with the advantage that this device can be introduced into the surgery procedure with minimal disruption to usual protocols. Also we expect this sensor could be used to investigate the creep deformation on the UHMWPE. Creep is a property of viscoelastic materials [18] which introduces non-linearities on the system and are a cause for errors in long-term measurements. The understanding of the creep behavior of the UHMWPE can also help on accurately quantify the prosthesis wear [19].

The strain-sensing device is simple to package and represents a cost effective solution since it does not imply changes on current artificial knee implant



designs. Future applications include the ability to validate mathematical models that describes the knee biomechanics, the capability to study the effect of postoperative physical therapy and evaluate the knee balance to improve overall rehabilitation. Moreover, it can be customized for different models of prosthesis combined with various materials, therefore the proposed autonomous sensor can lead to new redesigns regarding the function of knee implants and the treatment of patients with total knee implants. Additionally, the device could be integrated with low-power wireless telemetry, which will allow for long-term measurements *in vivo*.

## 5.8 Conclusion

We demonstrated a polyimide-based MEMS strain-sensing device for monitoring knee implants. Throughout the design process, FEA modeling results were used to optimize device placement inside an artificial knee component (UHMWPE). The PI-based technology is well suited for biomedical applications and can provide a significant cost advantage since it does not imply changes on current prosthesis. The device was subjected to tests in a mechanical knee simulator using static and dynamic axial load conditions similar to those encountered *in vivo*. Results indicated the measured strain is in accordance with simulated strain and that the applied forces can be estimated from measured strain. The experimental data demonstrates the sensor is capable of measuring the strain associated to the total axial forces in the range of approximately 4 times body weight with a good sensitivity and accuracy for events happening within a 1 s time window.

Compared with the current available technology either using strain gauges, fiber Bragg gratings or Tekscan sensing systems [4–7] or even most recent solutions, such as the one provide by OrthoSensor (which followed a similar approach though providing a disposable instrument) the system developed in this thesis provides a suitable solution for implantation while the available solutions can only be used during surgery. This advantage comes at the cost of having sensors embedded on the UHMWPE insert which is a viscoelastic material and therefore are prone to creep and stress relaxation. In the current application,

where high forces can be exerted, the UHMWPE may be deformed beyond the limit where linear viscoelasticity is accurate, and traditional plasticity models are not accurate since the applied loads are not monotonic. To overcome these limitations it is necessary to develop an advanced thermo-mechanical constitutive model for UHMWPE where the developed sensors can provide valuable information on the behavior of the material. Afterwards, the constitutive model could be used to perform real-time estimation and compensation of creep and stress relaxation.

## 5.9 References

- [1] G. Bergmann, A. Rohlmann, F. Graichen, P. Westerhoff, A. Bender, B. Heinlein, and R. Ehrig, "Design and Calibration of Load Sensing Orthopaedic Implants," *Journal of Biomechanical Engineering*, vol. 130, no. 2, p. 021009, 2008.
- [2] D. D. D'Lima, S. Patil, N. Steklov, J. E. Slamin, and C. W. Colwell, "Tibial forces measured in vivo after total knee arthroplasty," *The Journal of Arthroplasty*, vol. 21, pp. 255–262, Feb. 2006.
- [3] A. Arami, M. Simoncini, O. Atasoy, W. Hasenkamp, S. Ali, A. Bertsch, E. Meurville, S. Tanner, H. Dejnabadi, V. Leclercq, P. Renaud, C. Dehollain, P.-A. Farine, B. M. Jolles, K. Aminian, and P. Ryser, "Instrumented prosthesis for knee implants monitoring," in *2011 IEEE International Conference on Automation Science and Engineering*, pp. 828–835, IEEE, Aug. 2011.
- [4] S. J. Taylor, P. S. Walker, J. S. Perry, S. R. Cannon, and R. Woledge, "The forces in the distal femur and the knee during walking and other activities measured by telemetry," *The Journal of Arthroplasty*, vol. 13, pp. 428–437, June 1998.
- [5] B. Kirking, J. Krevolin, C. Townsend, C. W. Colwell Jr., and D. D. D'Lima, "A multiaxial force-sensing implantable tibial prosthesis," *Journal of Biomechanics*, vol. 39, no. 9, pp. 1744–1751, 2006.
- [6] B. Heinlein, F. Graichen, A. Bender, A. Rohlmann, and G. Bergmann, "Design, calibration and pre-clinical testing of an instrumented tibial tray," *Journal of Biomechanics*, vol. 40, pp. S4–S10, Jan. 2007.
- [7] L. Mohanty, S. C. Tjin, D. T. Lie, S. E. Panganiban, and P. K. Chow, "Fiber grating sensor for pressure mapping during total knee arthroplasty," *Sensors and Actuators A: Physical*, vol. 135, pp. 323–328, Apr. 2007.
- [8] D. Crescini, E. Sardini, and M. Serpelloni, "An Autonomous Sensor for Force Measurements in Human Knee Implants," *Procedia Chemistry*, vol. 1, pp. 718–721, Sept. 2009.
- [9] D. Crescini, E. Sardini, and M. Serpelloni, "Design and test of an autonomous sensor for force measurements in human knee implants," *Sensors and Actuators A: Physical*, vol. 166, pp. 1–8, Mar. 2011.
- [10] A. Grayson, R. Shawgo, A. Johnson, N. Flynn, Y. Li, M. Cima, and R. Langer, "A BioMEMS review: MEMS technology for physiologically integrated devices," *Proceedings of the IEEE*, vol. 92, no. 1, pp. 6–21, 2004.

- [11] A. Mercanzini, K. Cheung, D. Buhl, M. Boers, A. Maillard, P. Colin, J. Bensadoun, A. Bertsch, and P. Renaud, "Demonstration of cortical recording using novel flexible polymer neural probes," *Sensors and Actuators A: Physical*, vol. 143, pp. 90–96, May 2008.
- [12] M. Leonardi, E. M. Pitchon, A. Bertsch, P. Renaud, and A. Mermoud, "Wireless contact lens sensor for intraocular pressure monitoring: assessment on enucleated pig eyes.," *Acta Ophthalmologica*, vol. 87, pp. 433–437, June 2009.
- [13] H. Kasi, W. Hasenkamp, G. Cosendai, A. Bertsch, and P. Renaud, "Simulation of epiretinal prostheses - Evaluation of geometrical factors affecting stimulation thresholds.," *Journal of Neuroengineering and Rehabilitation*, vol. 8, p. 44, Aug. 2011.
- [14] R. R. R. Jr, J. A. Miller, W. M. Reichert, and R. R. Richardson, "Polyimides as biomaterials: preliminary biocompatibility testing.," *Biomaterials*, vol. 14, pp. 627–635, July 1993.
- [15] H. F. Brinson and L. C. Brinson, *Polymer Engineering Science and Viscoelasticity: An Introduction*. Springer, Jan 2008.
- [16] W. N. S. Jr and W. N. Sharpe, *Springer Handbook of Experimental Solid Mechanics*. Springer, Dec 2008.
- [17] H. Liu, M. A. Polak, and A. Penlidis, "A practical approach to modeling time-dependent nonlinear creep behavior of polyethylene for structural applications," *Polymer Engineering Science*, vol. 48, pp. 159–167, Jan 2008.
- [18] K. L. Phan, "Methods to correct for creep in elastomer-based sensors," *Sensors, 2008 IEEE*, pp. 1119–1122, Oct. 2008.
- [19] A. El-Domiaty and M. El-Fadaly, "Wear characteristics of ultrahigh molecular weight polyethylene (UHMWPE)," *Journal of Materials Engineering*, vol. 11, no. October, pp. 577–583, 2002.

# CHAPTER 6

## Catheter Pressure Sensor

*This Chapter is based on the following article:*

*W. Hasenkamp, et. al.,*

*"Polyimide/su-8 catheter-tip mems gauge pressure sensor",*

*Biomedical Microdevices (published).*

*The human mind treats a new idea the same way*

*the body treats a strange protein; it rejects it.*

*- P. B. Medawar*

## 6.1 Introduction

Silicon strain-gauge, metal-diaphragm sensors were first introduced commercially in 1958. In these early stage, due to its high-cost and low-volume manufacturing possibilities, biomedical and aerospace applications were targeted. This trend continued into the 1970s [1] when microsensor companies began to move toward higher-volume, lower-cost applications [2], in particular, the automotive industry [1]. From the 1980s to the present, biomedical and automotive applications are some of the most widely reported in the literature, however new market applications and technologies are constantly being developed.

Currently, polymer-based microelectromechanical systems (MEMS) are increasingly being used in biomedical applications [3]. Inexpensive well-established micromachining techniques, material versatility, robustness and biocompatibility constitute some of its potential advantages over conventional biomedical device fabrication methods [4]. A number of polymer-based devices has been realized including implantable microelectrodes [5], microsystems for neural prostheses [6], microfluidic devices [7], temperature sensors [8], humidity sensors [9], sensors for orthopedic implants [10], tactile sensors [11] and pressure sensors [12–15].

In general, equipment requirements for polyimide/SU-8 MEMS processing are similar to those of conventional microfabrication techniques, hence commonly available cleanroom equipment and materials can be utilized for processing without extensive development. We have chosen to integrate polyimide and SU-8 into the fabrication of a catheter-tip MEMS gauge pressure sensor. Polymer-based pressure sensors have many *in vivo* applications such as intracranial pressure monitoring in case of head trauma [16], intraocular pressure evaluation for glaucoma [17], blood pressure and heart rate monitoring for cardiovascular assessment [3].

In biomedical research, genetically modified mice are seen with growing interest, since diseases can be expressed and studied in a convenient platform, creating needs for more compact and precise devices. Miniaturized pressure sensors offer potential improvement over fluid-filled catheters [18], as they can be

mounted on the catheter-tip directly which avoids signal damping due to pressure dynamics. In fluid-filled systems, the catheter is inserted into the target site and transmits the pressure to a remote sensor through the fluid column - effectively creating a low-pass filter impairing the monitoring of rapid fluctuations [19]. Furthermore, miniaturize sensors can decrease the risk of thrombosis, embolism and infections since common available commercial sensors are oversized and will not fit into specific small vessels or cavities [13].

This chapter presents the development of a 400  $\mu\text{m}$ -wide hybrid polymer-based (polyimide/SU-8) strain gauge pressure sensor mounted at the tip of a Pebax catheter (inner diameter/outer diameter: 0.20/0.48 mm). Finite Element Analysis (FEA) was used to investigate the distribution of the stress and strain on the polyimide membrane and to evaluate the device dimensions and the appropriate locations for the placement of the sensing elements. The sensing elements consist of piezoresistive thin-film metallic wires embedded in a flexible polyimide membrane. A sealed pressure chamber is created upon the polyimide membrane using an adapted bonding technique, commonly employed to fabricate microchannels [7]. The sealing is made at ambient temperature in air which becomes the permanent internal reference pressure of the sensor. Next, the device is evaluated experimentally. First, its performance is compared with a commercial silicon-based pressure sensor. Next, the response of both sensors are compared when exposed to high-speed pressure fluctuations. Finally, the device is used *in vivo* to measure blood pressure of a mouse.

## 6.2 Finite element analysis of the UHMWPE insert and sensing element placement

The chosen method for measuring the pressure is to detect mechanical deformations in a thin polyimide membrane supported by a sealed pressure chamber made in SU-8. In this development, FEA was used to investigate the stress and strain in the polyimide (PI) membrane in order to determine the appropriate membrane thickness, to assure no plastic deformation occurs during the operation of the device, and to assist with the placement of the strain gauges

within the device. A 2D Computer Aided Design (CAD) model was built into a commercial FEA software, COMSOL Multiphysics (v4.2a). The 2D CAD model is presented in Fig. 6.1, and comprises a PI membrane, platinum wires as the piezoresistive element and a pressure chamber made of SU-8, which is an epoxy-based negative photoresist. The total width of the device was limited to  $400\ \mu\text{m}$  in order to match the tip-width of a Pebax catheter (inner diameter/outer diameter:  $0.20/0.48\ \text{mm}$ ). The  $100\ \mu\text{m}$ -wide,  $50\ \mu\text{m}$ -thick SU-8 pressure chamber was designed to prevent deformations other than those of the PI membrane. Other geometrical dimensions (i.e. membrane thickness and strain gauge line length) were chosen from the results of the simulation.

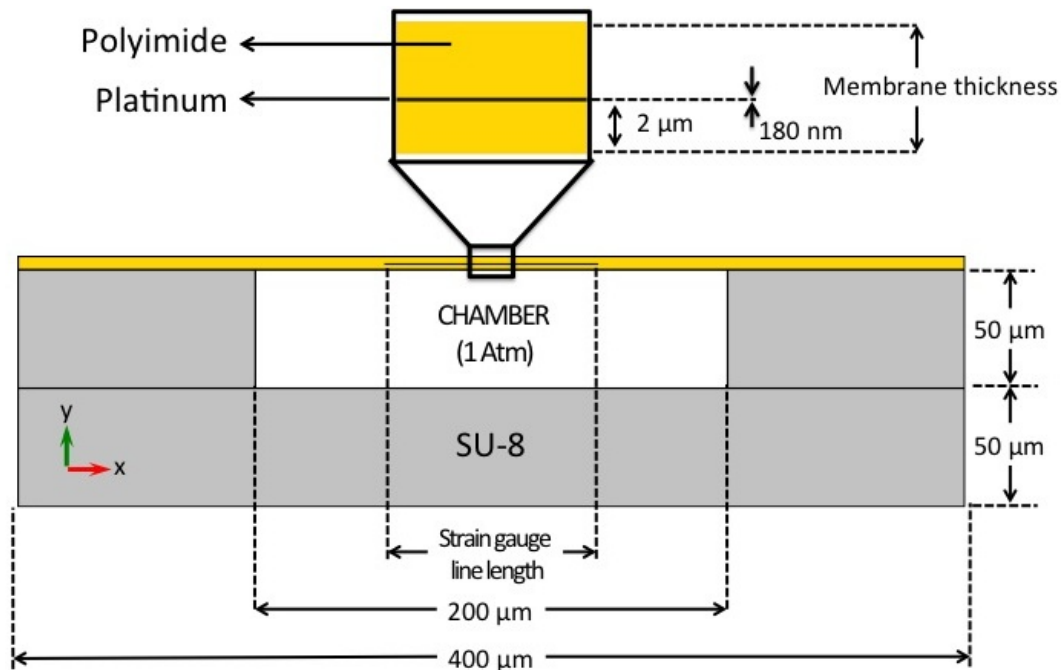


Figure 6.1: CAD model comprising the polyimide membrane, the platinum as piezoresistive material and the SU-8 enclosed chamber (cross-section along the device width).

The FEA was modeled using the Structural Mechanics module of Comsol in stationary mode assuming a linear elastic behavior for all parts. The fundamental considerations in this approach are to assume a small strain (or stress) and a linear relationship between the components stress/strain (i.e. Young's modulus). Moreover, the results are valid only for stress states that do not produce plastic deformation, therefore stresses above the yield point (YP) of the



materials will be discredited. The material properties necessary to perform the FEA are: density ( $\rho$ ), Young's modulus ( $E$ ) and Poisson's ratio ( $\nu$ ). The assumed values are presented in Table 6.1.

Table 6.1: Material properties used in the FEA.

Material	$\rho$ [ $kg/m^3$ ]	$E$ [ $Pa$ ]	$\nu$
Polyimide	1400	$8 \times 10^9$	0.2
Platinum	21450	$145 \times 10^9$	0.38
SU-8	1200	$4.4 \times 10^9$	0.22

The following constraints were added to the model. A boundary condition load was applied around the device to account for pressure changes outside the device. Another boundary condition load was defined inside the device, corresponding to the inner part of the SU-8 pressure chamber. This constraint accounts for pressure changes inside the device due to changes in the cross-sectional area of the pressure chamber induced by the external change in pressure. Equation 6.1 defines the pressure change as a function of the cross-sectional area, where  $\Delta p$  corresponds to the pressure change inside the device,  $p_0$  is the gauge pressure inside the pressure chamber (considered to be the ambient pressure in which the the device was fabricated),  $A_0$  is the pressure chamber cross-sectional area at ambient pressure ( $10^5 \mu m^2$ ),  $A$  is the pressure chamber cross-sectional area induced by the external changes in pressure and  $\gamma$  is the adiabatic index (1.4 for air). To complete the model, a fixed constraint is defined at the bottom of the device to avoid overall device displacement which can introduce discrepancies in the simulation.

$$\Delta p = p_0 \left( \left( \frac{A_0}{A} \right)^\gamma - 1 \right) \quad (6.1)$$

Unstructured progressive triangular meshing algorithm was utilized for meshing the model with minimum and maximum element size of 8 nm and 4  $\mu m$ , respectively. The total number of elements generated by the meshing was 34088. The convergence criteria were establish by a MUMPS solver.

### 6.3 Results of the finite element analysis

FEA was first used to evaluate the acceptable thickness values for a PI membrane closing the SU-8 chamber. The PI has a yield point (YP) of approximately 65 MPa and larger values of stress result in plastic deformation of PI, permanently damaging the device. The simulation was performed in a simplified model using a monolithic PI membrane without platinum tracks and exposed to a pressure of 350 mmHg, corresponding to more the twice the blood pressure for mice. Fig. 6.2 shows the evolution of the x-component of the membrane stress with the membrane thickness, along the device width and in the location where the membrane stress is maximum (in the transverse plane situated at the top of the PI membrane). Clearly visible is the presence of high values of stress where the PI membrane is attached to the SU-8 chamber, and the limit of plastic deformation of PI is reached at those locations for membranes thinner than 3  $\mu\text{m}$ . For the fabrication of the device, PI membranes were therefore chosen to be 5  $\mu\text{m}$  in total thickness.

The PI membrane deflection was also analyzed, both in width and in length, for different values of pressures. These pressure variations were added to the atmospheric pressure of 1 atm. Fig. 6.3 presents the results for a 5  $\mu\text{m}$  thick PI membrane deflection in response to applied pressure, in the transverse plane situated at the top of the PI membrane. Fig. 6.3(a) shows the deflection in a cross-section along the width of the device and Fig. 6.3(b) presents the deflection in a cross-section along the length of the device. Both graphs in Fig. 6.3 show no deflection of the PI membrane at 0 mmHg (corresponding to the atmospheric pressure). This is expected since the pressure inside the sensor's pressure chamber was set to 1 atm (matching the packaging ambient pressure). At the pressure of 300 mmHg the computed deflection of the membrane is approximately 2.1  $\mu\text{m}$  with the two graphs in Fig. 6.3 showing a linear deformation of the membrane with the applied pressure. In Fig. 6.3(b) we verify a constant strain region in the center of the membrane along approximately 0.6 mm in length. Therefore, we chose to fabricate strain gauges having a maximum width of 600  $\mu\text{m}$  to fit into a 1 mm long membrane.

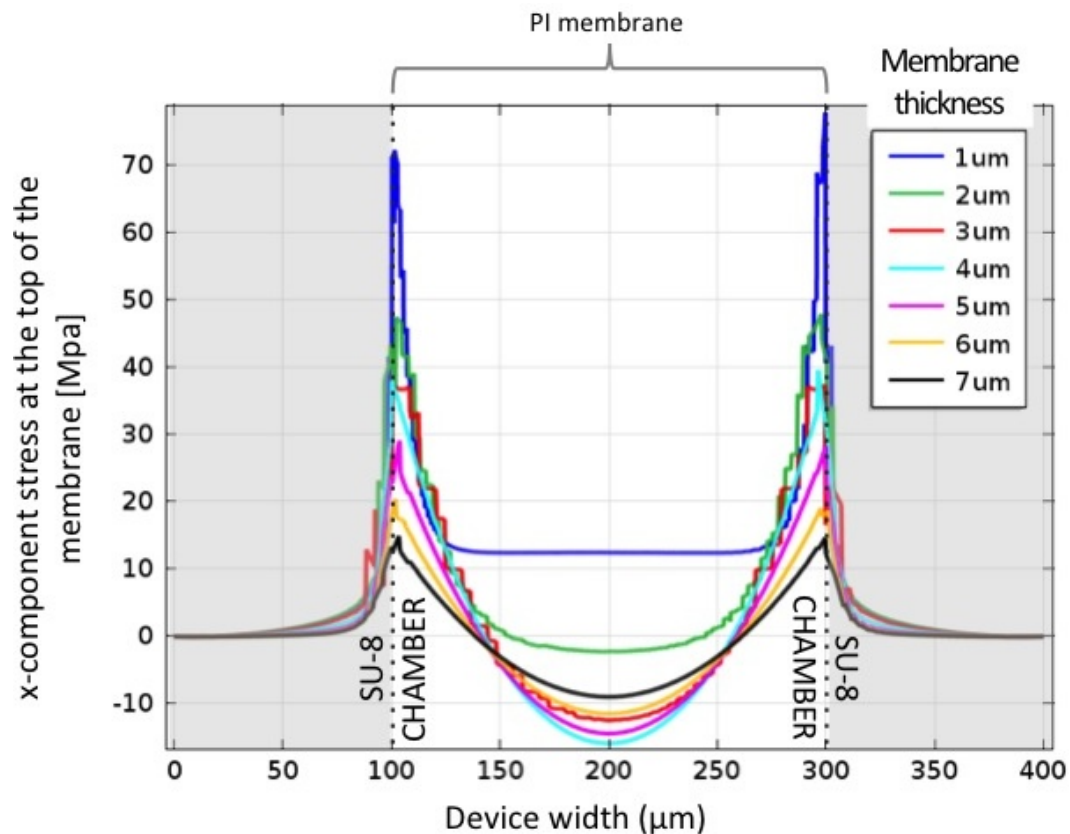


Figure 6.2: x-component of the membrane stress along the device width as a function of the membrane thickness, in the transverse plane situated at the top of the PI membrane.

To define the line length of the active strain gauge a FEA simulation was performed to investigate the strain on the PI membrane. Fig. 6.4 shows the x-component of the strain of a 5  $\mu\text{m}$  thick membrane as a function of the applied pressure, in the transverse plane situated at the top of the PI membrane, along the device width. Highly strained regions are present in the middle of the device (mostly compressive) and close to the SU-8 walls (both compressive and tensile), however the central part of the membrane sustains the strain over a longer region, without changing from compressive to tensile strain. Therefore, the active strain gauge of the device was placed in the central part of the membrane. To avoid tensile strain and keep a safe margin for alignment during fabrication, a line length of 90  $\mu\text{m}$  was chosen for the active strain gauge. To fit the defined maximum strain gauge area width of 600  $\mu\text{m}$  and simplify the

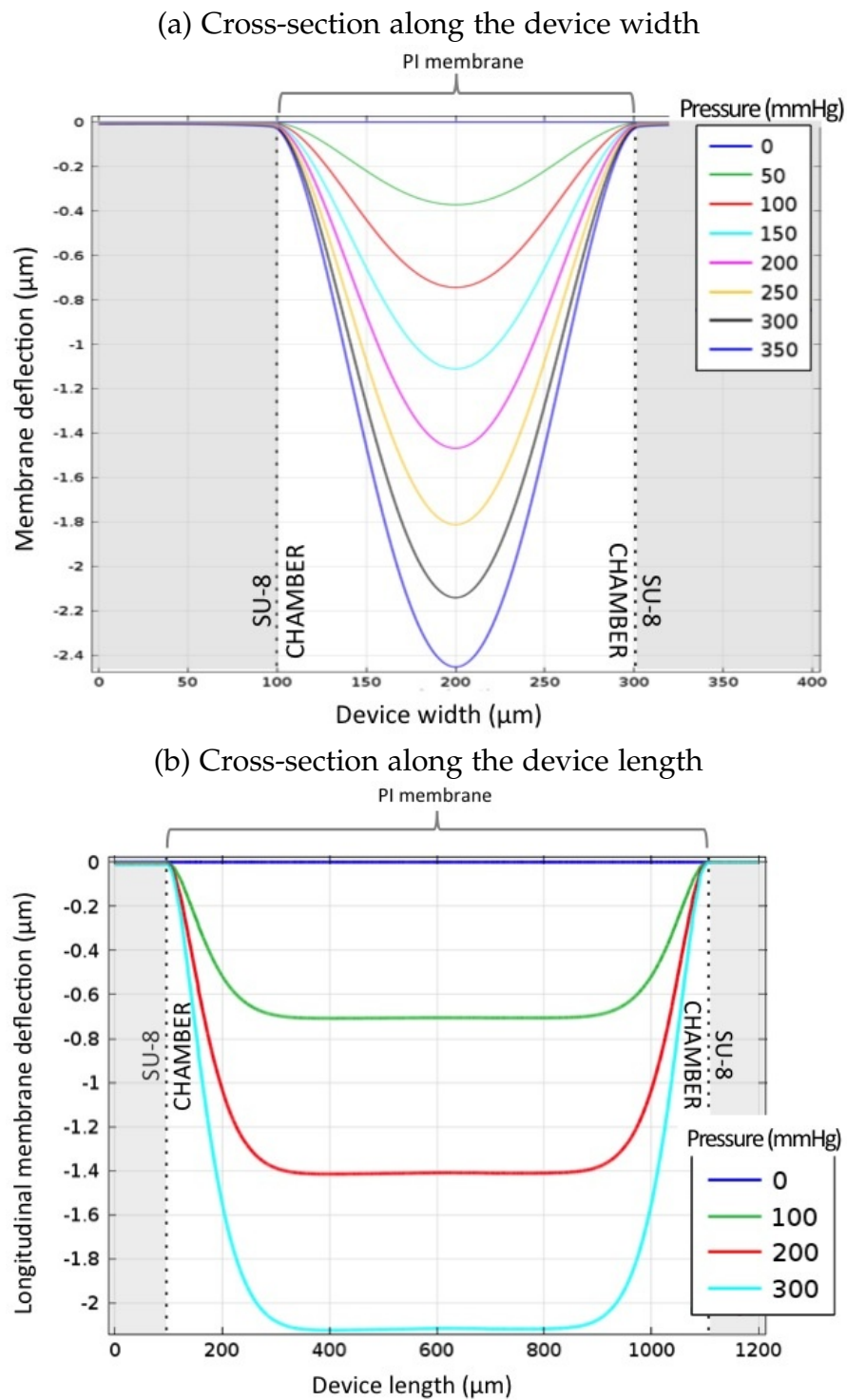


Figure 6.3: PI membrane deflection with the applied pressure, in the transverse plane situated at the top of the PI membrane. (a) Width cross-section and (b) Length cross-section.

photolithography process during device fabrication the line width of the strain gauges was defined to be  $4\ \mu\text{m}$  with line spacing of  $6\ \mu\text{m}$ .

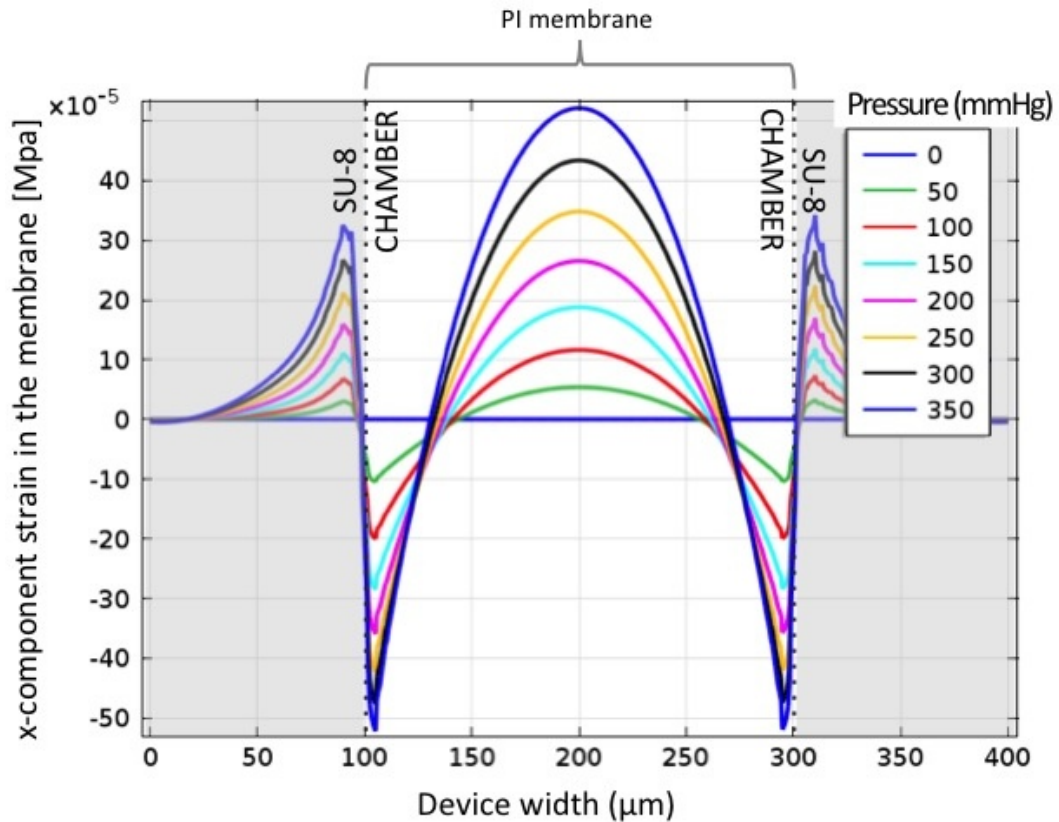


Figure 6.4: x-component of the membrane strain with the applied pressure, in the transverse plane situated at the top of the PI membrane and along the device width. 2D model without platinum trace.

Having defined the location and dimensions of the active strain gauge to be placed as sensing element in the PI membrane, a second FEA modeling step was performed using a model in which the metal tracks are considered in order to evaluate their effect on the PI membrane strain and stress. The platinum metal tracks were inserted  $2\ \mu\text{m}$  from the bottom of the PI membrane. Fig. 6.5 presents the impact of the  $90\ \mu\text{m}$  line length strain gauge on the x-component of the strain (Fig. 6.5(a)) and stress (Fig. 6.5(b)) in the PI membrane with the applied pressure, in the transverse plane situated at  $2\ \mu\text{m}$  from the bottom of the PI membrane and along the device width. The highly strained regions seen close to the metal line (at  $160\ \mu\text{m}$  and  $240\ \mu\text{m}$  in width) are artifacts due to

the interactive convergence and discretization methods governing the algebraic expressions in a discrete domain (e.g. finite-element). The stiffening effect of the piezoresistive material embedded in the PI membrane is clearly visible in the central part of the graph. When compared to the results from Fig. 6.4 a 32 % reduction of the strain was found as a consequence of the presence of the metal tracks in the PI membrane. In Fig. 6.5(b) the stress on the platinum domain is much higher than in the PI material, however the YP of platinum is  $\sim 1$  GPa. Therefore, no plastic deformation is expected in the device since results show a maximum stress of 55 MPa for 350 mmHg. Also, from Fig. 6.5 we can derive the expected sensitivity of the modeled device to be  $\sim 1 \mu\text{V}/\text{mmHg}$ .

Another important information on the membrane is the resonant frequency, which was calculated to be around 80 to 100 kHz. This is an important parameter to be verified in order to consider the measurements to be reliable. Consequently, the resonant frequency of the membrane should be higher (at least three to five times) than the highest frequency of the dynamic pressure under investigation.

## 6.4 Sensor design, fabrication and packaging

The polyimide/SU-8 catheter-tip MEMS gauge pressure sensor contains 2 strain gauges, one active gauge positioned in the middle of the deformable PI membrane and one passive gauge to account for temperature compensation, positioned on the SU-8 wall where no deformation occurs. The resistance of the strain gauges was designed to be 3.2 k $\Omega$  in order to facilitate readout and decrease the power consumption, to be able to connect directly to a commercially available passive telemetry chip. The membrane containing the strain gauges was built in polyimide-metal-polyimide sandwich structures by dry etching. The SU-8 pressure chamber was micromachined by standard photolithography and an adapted bonding technique was used to close the chamber with a SU-8 layer. The membrane thickness was selected from the results of the FEA and defined to be 5  $\mu\text{m}$  in order to have a good tradeoff between having a good device sensitivity while safely operating to prevent plastic deformation. The total thickness of the complete device is approximately 105  $\mu\text{m}$ . A cross-

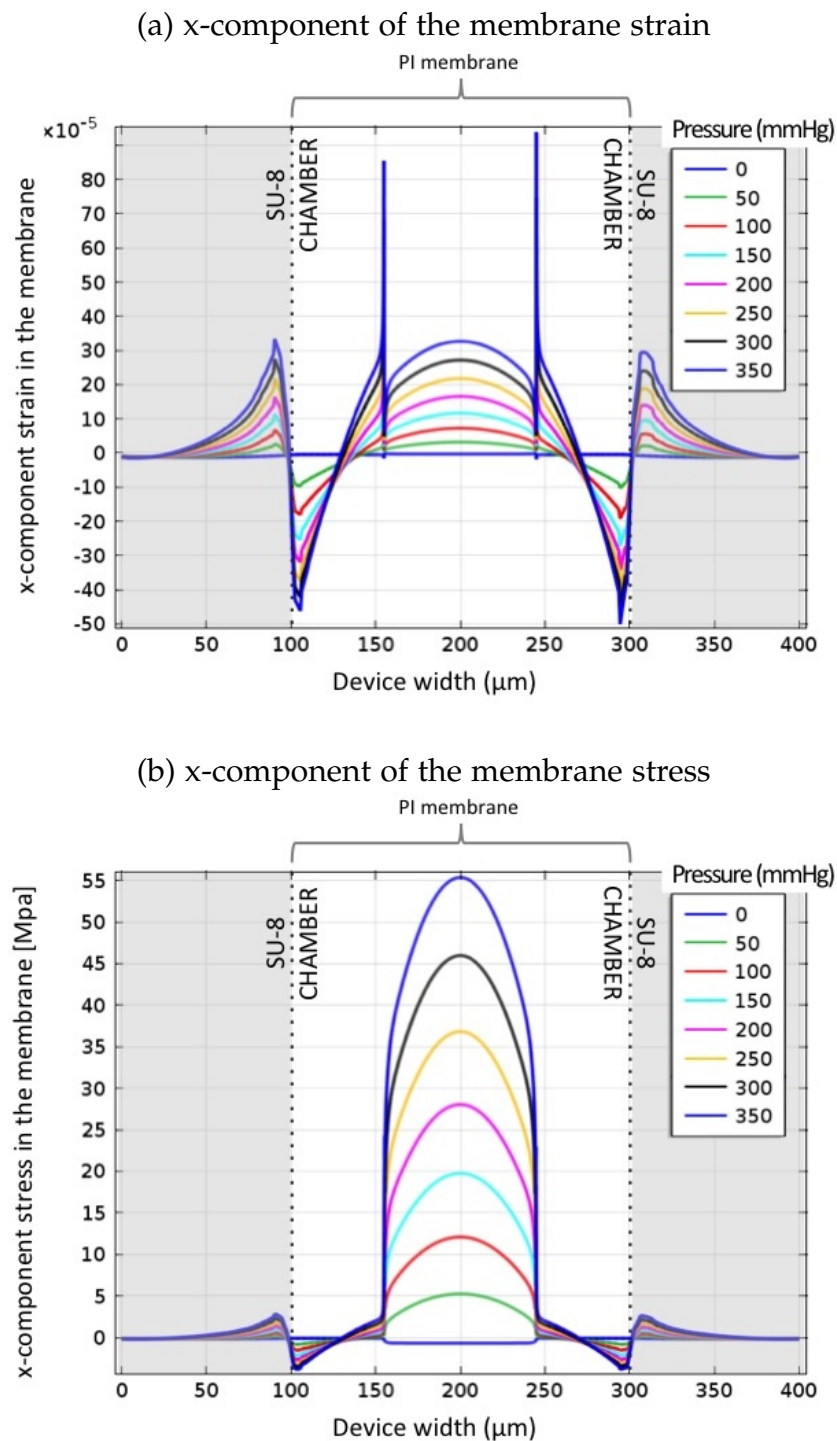


Figure 6.5: x-component of the membrane (a) strain and (b) stress with the applied pressure, in the transverse plane situated at 2  $\mu\text{m}$  from the bottom of the PI membrane and along the device width. 2D model including the defined platinum line embedded into the polyimide membrane.

sectional view of the microfabrication process is presented in Fig. 6.6.

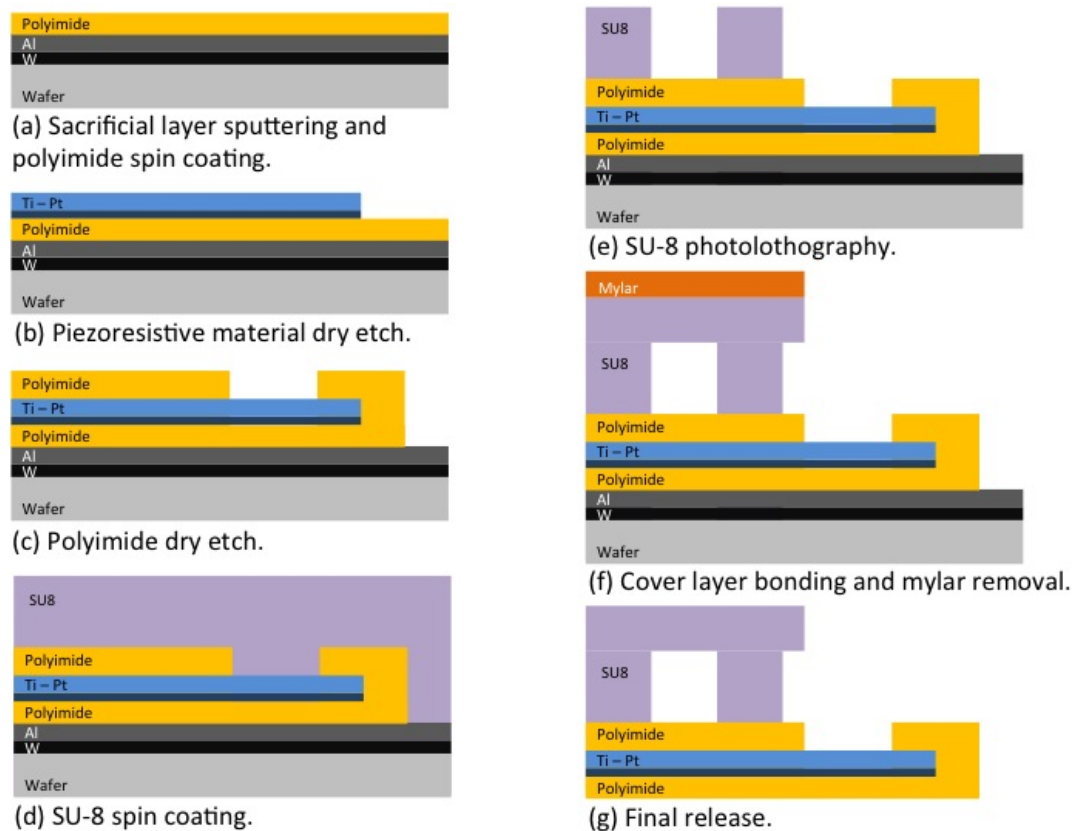


Figure 6.6: Cross-section view of the fabrication process.

The detailed microfabrication process comprises the following steps: A sacrificial layer of tungsten (100 nm) and aluminum (1  $\mu\text{m}$ ) is first thermally evaporated onto a carrier silicon wafer. A 2.5  $\mu\text{m}$  layer of PI (PI2611, HD Microsystems) is applied on top of the aluminum by spin-coating and cured at 300  $^{\circ}\text{C}$  for 1 h in nitrogen atmosphere (Fig. 6.6(a)). A titanium adhesion layer (20 nm) and platinum layer (180 nm) are then sputtered onto the cured polyimide. The strain gauges are patterned by reactive ion etching in  $\text{Cl}_2$  using a patterned photoresist as an etch mask (Fig. 6.6(b)). A second layer of PI, 2.5  $\mu\text{m}$  in thickness, is spin-coated and likewise cured. An etch mask of sputtered  $\text{SiO}_2$  (500 nm) is deposited onto the sandwich structure and then patterned by reactive ion etching using a photoresist etch mask. This oxide layer is then used as hard mask during the subsequent oxygen plasma etch of the polyimide to define both the structure outline and open contact pads to the strain gauges



(Fig. 6.6(c)). A 50  $\mu\text{m}$  layer of SU-8 (GM1070, Gersteltec Engineering Solutions) is applied on top of the polyimide membrane by spin-coating and processed according to the manufacturer specifications (Fig. 6.6(d)). The SU-8 wall that will support the cover layer is made by photolithography, the development of the SU-8 is performed in propylene glycol methyl ether acetate (PGMEA) after which it is cured at 90  $^{\circ}\text{C}$  for 15 min (Fig. 6.6(e)). On a second carrier substrate, two thin layers of Ordil<sup>TM</sup> and one layer of Mylar<sup>TM</sup> are made to adhere temporarily to the carrier. Ordyl<sup>TM</sup> is negative tone resist while Mylar<sup>TM</sup> is a polyester film, however their use in such combination, on a carrier, are made to facilitate the lamination procedure. Afterwards, 50  $\mu\text{m}$  of SU-8 is spun onto the Mylar<sup>TM</sup> foil. The SU-8 is then pre-baked up to 65  $^{\circ}\text{C}$ , flipped onto the first wafer, contacting the SU-8 sidewalls and then the Mylar<sup>TM</sup> is removed (Fig. 6.6(f)). The laminated SU-8 sandwich undergoes photolithography to define the pressure chamber on the underlying device. Development is performed with PGMEA, and laminate is heated up to 90  $^{\circ}\text{C}$  to ensure bonding and cure the epoxy effectively, thus sealing the pressure chamber. The devices are detached from the substrate by anodic metal dissolution in a 10 wt% sodium chloride solution, dissolving the aluminum and releasing the devices (Fig. 6.6(g)). Optical images of a released device comprising the enclosed SU-8 chamber, the active and passive strain gauges, as well as the suspended PI membrane are shown in Fig. 6.7. At this stage the device is ready to be packaged into a catheter.

The packaging of the device into the Pebax catheter consists of bonding 40  $\mu\text{m}$  diameter insulated copper wires to the device contact pads using a conductive epoxy. This Pebax tube has an inner diameter of 0.20 mm and an outer diameter of 0.48 mm. The copper wires provide the connection between the strain gauges and the complementary electronic circuitry. They were wired through the inner part of the catheter and connected to the rest of the circuit. To protect the connections and attach the device to the tip of the Pebax catheter a standard insulating epoxy was used. The assembled polyimide/SU-8 catheter-tip MEMS gauge pressure sensor is shown in Fig. 6.8 in comparison with a commercial Millar Mikro-Cath<sup>TM</sup> disposable pressure catheter fabricated using CMOS technology.

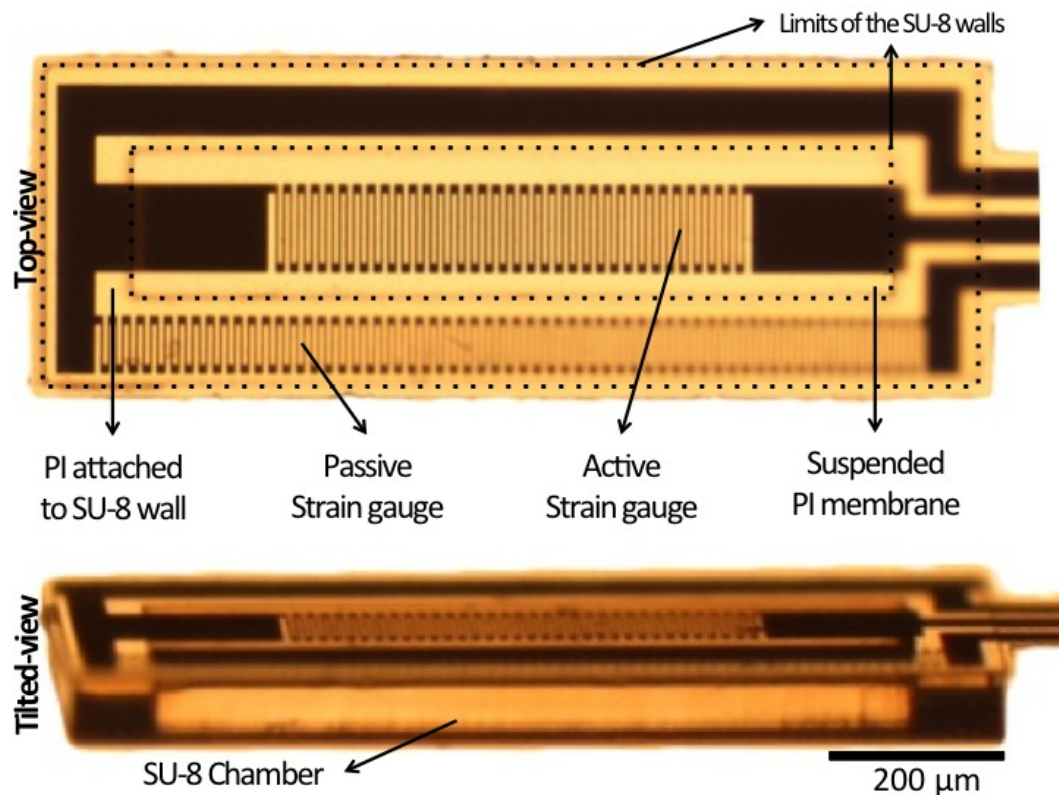


Figure 6.7: Optical images, respectively top-view and tilted-view, of a released device comprising the enclosed SU-8 chamber, the active and passive strain gauges, as well as the suspended PI membrane.

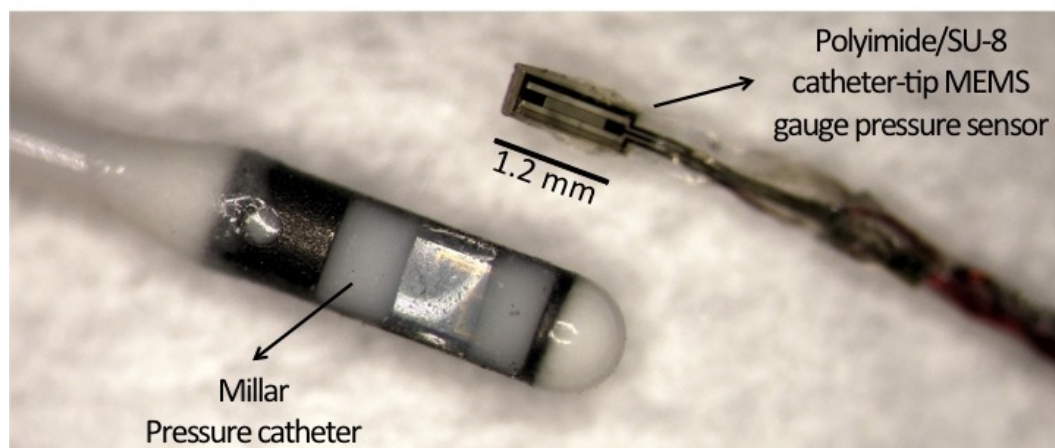


Figure 6.8: Assembled polyimide/SU-8 catheter-tip MEMS gauge pressure sensor in comparison with a commercial Millar Mikro-Cath™ disposable pressure catheter.

## 6.5 Experimental setup and procedure

The calibration consists of measuring the voltage output of the device when it is submitted to pressure changes. For this procedure the device and a reference pressure sensor are inserted into a sealed rigid tube. The tube is plugged to a relief valve, which will provide a constant value of pressure ( $P_{DC}$ ). The relief valve is directly connected to a compressed air supply ( $P_{supply}$ ). Pressure variations ( $P_{AC}$ ) are generated with a pneumatic actuator also connected to the rigid tube. The schematic diagram of the experimental setup is presented in Fig. 6.9.

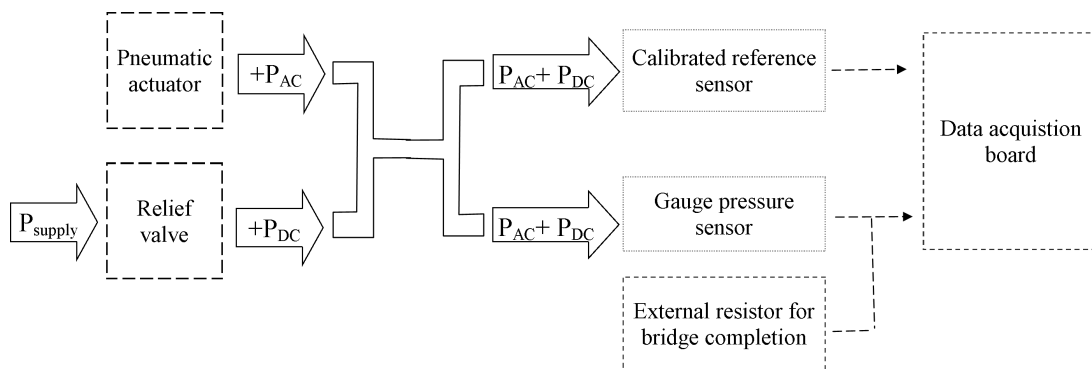


Figure 6.9: Schematic diagram of the experimental setup

The polyimide/SU-8 catheter-tip MEMS gauge pressure sensor is connected in a Wheatstone bridge configuration using two external standard resistors with similar impedance to strain gauges in the membrane. The bridge is powered with 2.5 V and the output signals were recorded with a National Instruments data acquisition board (NI-Daqpad-6015) and a signal conditioning unit (SC-2345) connected to a full-bridge input channel (SCC-SG04). For displaying and recording the measurements a LabView (National Instruments) interface is configured. A calibrated pressure sensor (ENTRAN Pressure Transducer, Model EPX-N01-0.7B) is also attached to the experimental setup and used as reference sensing element for calibrating the device. The reference pressure sensor is powered with 10 V and the signal is acquired using the National Instruments electronic interface previously described, and adding a full-bridge input channel (SCC-SG24). The signal conditioner's gain and span controls for both sensors are set to obtain a full-scale electrical output signal.

## 6.6 Experimental Results

A time-dependent signal was acquired during the dynamic change in pressure using both sensors, the Polyimide/SU-8 catheter-tip MEMS gauge pressure sensor and the reference pressure sensor. The calibration curve (reference pressure as a function of the voltage output of the gauge pressure sensor) is shown in Fig. 6.10. The linear regression (adjusted R-square = 0.9982) shows that the gauge pressure sensor has a sensitivity of  $2.78 \mu\text{V}/\text{mmHg}$ . The sensor response to changes in temperature is shown in Fig. 6.11 together with a linear fit of the data (adjusted R-square = 0.9974). This fit implies a temperature sensitivity of  $90 \mu\text{V}/^\circ\text{C}$ , or approximately  $30 \text{ mmHg}/^\circ\text{C}$ .

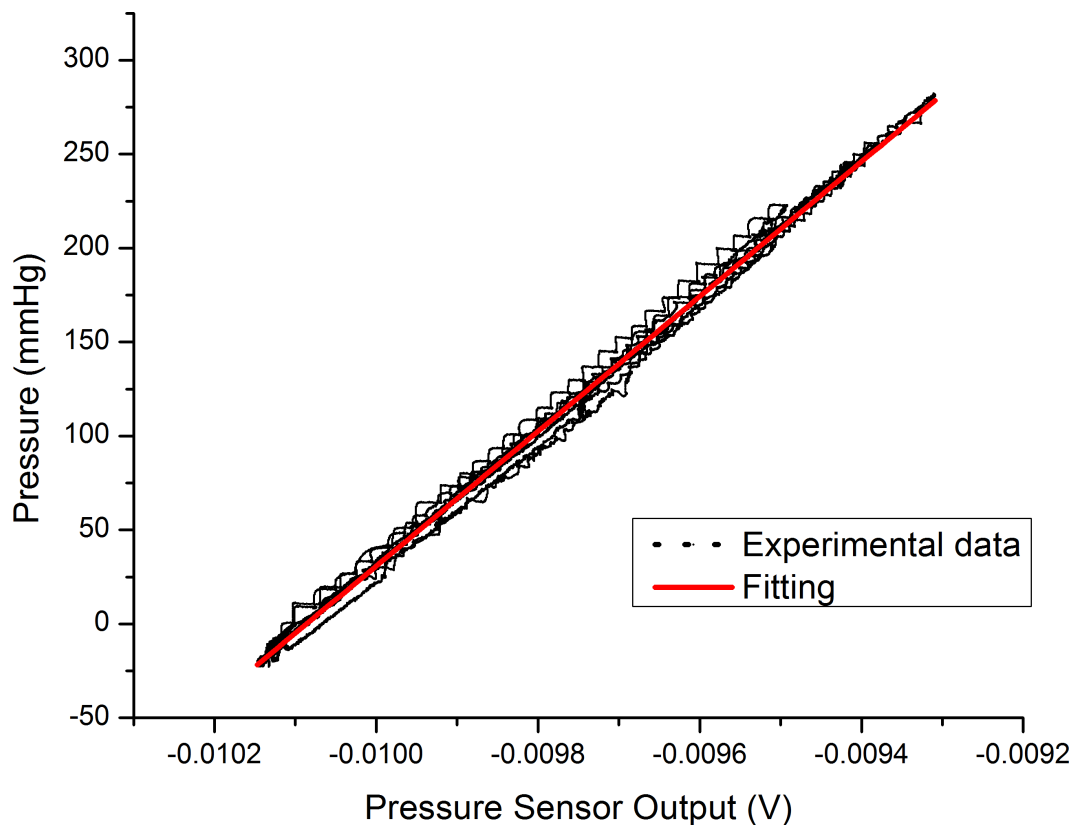


Figure 6.10: Polyimide/SU-8 gauge pressure sensor calibration curve showing reference pressure as a function of the voltage output of the gauge pressure sensor and corresponding linear regression fitting the data.

Before *in vivo* testing, the performance of the packaged sensor was evaluated in response to an external oscillating pressure. The pressure inside the rigid

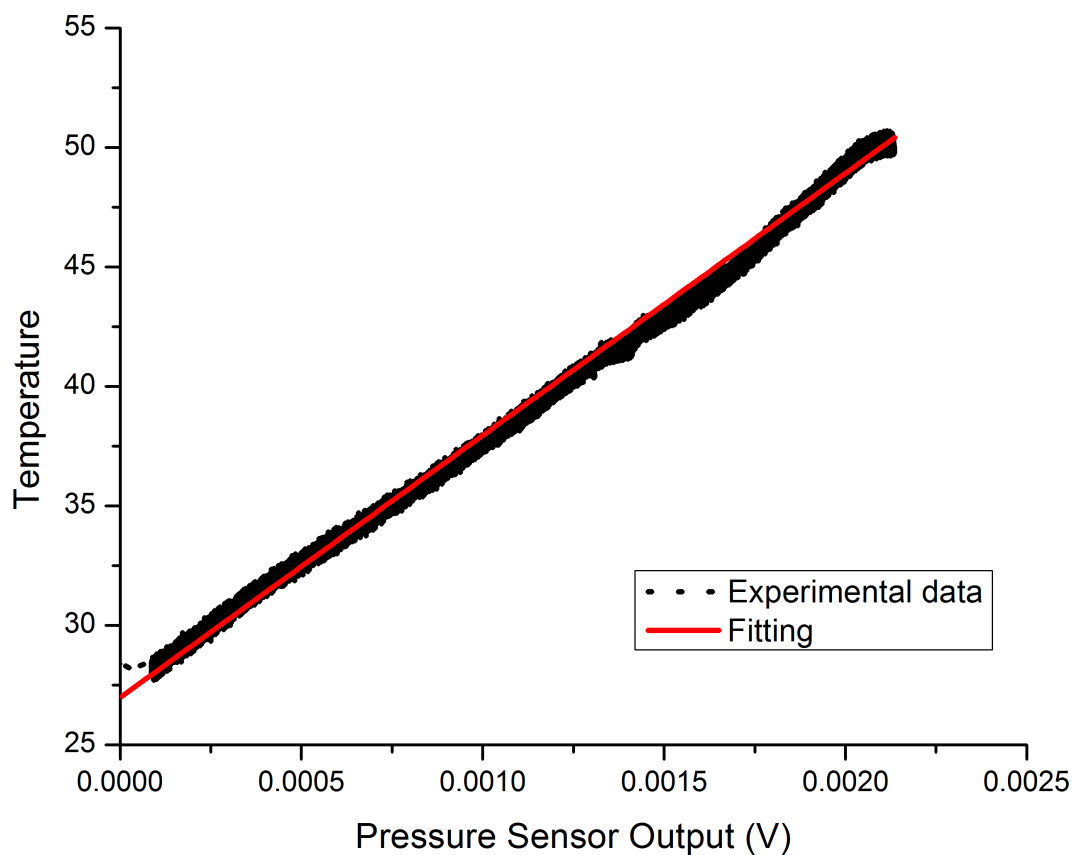


Figure 6.11: Polyimide/SU-8 gauge pressure sensor response to changes in ambient temperature as a function of the voltage output of the gauge pressure sensor and corresponding linear regression fitting to the data.

tube was varied at a frequency of  $\sim 7$  Hz to emulate the mouse heart beat while the pressure was recorded using both the reference pressure transducer and the polyimide/SU-8 gauge pressure sensors. Results are presented in Fig. 6.12. The polyimide/SU-8 catheter-tip MEMS gauge pressure sensor performed similarly to the commercial reference sensor. The time-delay observed between the reference sensor and the polymer-based pressure sensor is due to the distance between the sensors in the experimental setup.

## 6.7 *in vivo* experiment

The goal of the *in vivo* experiment was to prove the device concept and measure mouse blood pressure and heart rate. A male C57BL/6J mouse (weighing

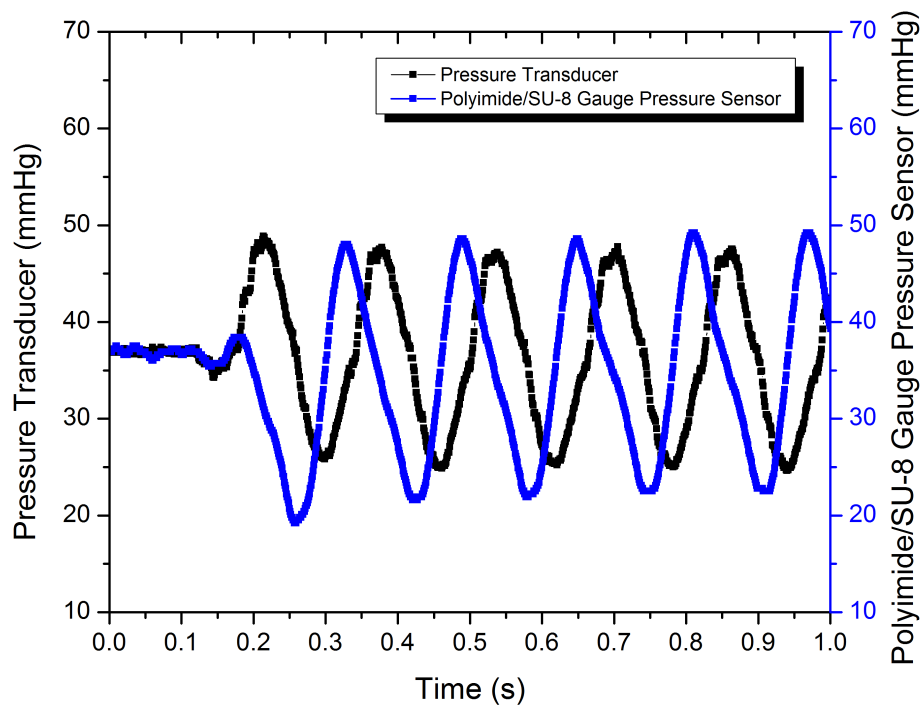


Figure 6.12: Response of the reference pressure transducer and the polyimide/SU-8 gauge pressure sensor as a function of the time for pressure variations at a frequency of  $\sim 7$  Hz

45g) was anesthetized via inhalation of 1-2% isoflurane mixed with oxygen. The left carotid artery was exposed for a length of 5 mm. The fabricated polyimide/SU-8 catheter-tip MEMS gauge pressure sensor was inserted 4 mm into the left carotid artery and tied. The pressure sensor wire was connected to the data-acquisition system to record blood pressure (BP) and heart rate (HR) for about 5 min at a sampling rate of 1 kHz. Anesthesia was maintained by 0.5-1% isoflurane inhalation mixed with oxygen.

Fig. 6.13 shows a trace of intra-arterial BP and HR for 2 seconds. HR is 450 beats/min, systolic BP is  $129 \pm 1$  mmHg and diastolic BP is  $115 \pm 1$  mmHg. The waveform of blood pressure is similar to results obtained with fluid-filled catheters and standard commercial sensors [19].

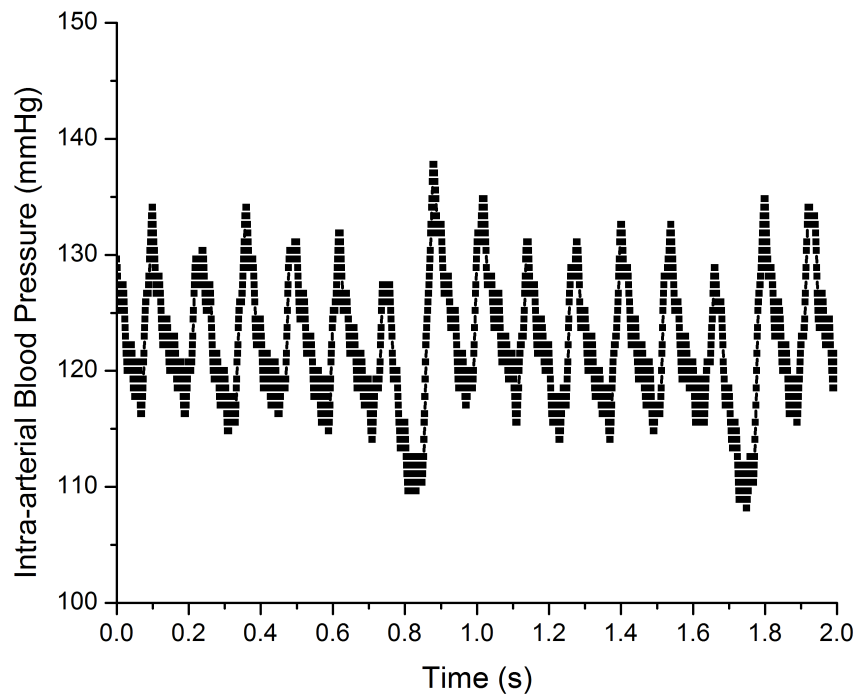


Figure 6.13: Trace of carotid arterial blood pressure and heart rate in a male C57BL/6J mouse during inhalation of 0.5-1% isoflurane.

## 6.8 Discussion

In this study, a polymer-based catheter-tip gauge pressure sensor was developed for biomedical applications. Experimental results were in good agreement with simulations regarding the device sensitivity. The experimental data demonstrated the sensor has similar characteristics to commercial available devices and can be used in selected biomedical applications (i.e. cardiovascular assessments), and as an alternative to fluid-filled catheters or pressure sensors catheters.

The sensitivity of the device can be improved by decreasing the PI membrane thickness and by changing the placement of the strain gauges inside the PI membrane. FEA indicates a nearly 10 fold increase in sensitivity when using a 4  $\mu\text{m}$  thick PI membrane with platinum strain gauges positioned 500 nm from

the bottom of the membrane. Optionally, in order to improve sealing of the cavity a layer of Parylene could be evaporated on the device.

The polyimide/SU-8 catheter-tip MEMS gauge pressure sensor is simple to package and represents a cost effective solution for certain *in vivo* pressure monitoring applications. Adapting the design, improving the packaging and further miniaturizing the pressure sensor will allow not only to insert the device in the carotid artery of mice, but also to place it directly on the heart of the mouse to measure the pressure in the ventricle. Moreover, the device could be integrated with implantable wireless telemetry, which can increase monitoring efficiency, allowing for long time measurements and permitting pressure measurements in awake animals.

## 6.9 Conclusion

In this chapter, we demonstrated a polyimide/SU-8 catheter-tip MEMS gauge pressure sensor. Throughout the design process, FEA modeling results were used to optimize the device before fabrication. Compared to a silicon-based pressure sensor the polymer-based device was found to show a similar performance in terms of response and sensitivity, despite not being a true gauge sensor neither an absolute pressure sensor. A good definition for this sensor would be "sealed pressure sensor" since it is similar to a gauge pressure sensor except that it measures pressure relative to some fixed pressure rather than the ambient atmospheric pressure (which varies according to the location and the weather). From the experimental results it is clear that the limitation of the device relies on the thermal drift, which is mainly dominated by the thermal expansion of the air inside of the cavity. However such limitation is not critical in applications where the thermal drift is minimal such as in implantable devices. Therefore, the polymer-based technology and SU-8 lamination step are well suited for biomedical applications and provide a significant cost advantage over silicon microfabrication techniques while also simplifying the packaging of such devices. Finally, the *in vivo* use of this sensor was demonstrated by measuring the heart rate and carotid blood pressure in mice.



## 6.10 References

- [1] S. Clark and K. Wise, "Pressure sensitivity in anisotropically etched thin-diaphragm pressure sensors," *IEEE Transactions on Electron Devices*, vol. 26, pp. 1887–1896, Dec 1979.
- [2] J. Meindl and K. Wise, "Foreword," *IEEE Transactions on Electron Devices*, vol. 26, pp. 1861–1863, Dec 1979.
- [3] A. Grayson, R. Shawgo, A. Johnson, N. Flynn, Y. Li, M. Cima, and R. Langer, "A BioMEMS review: MEMS technology for physiologically integrated devices," *Proceedings of the IEEE*, vol. 92, no. 1, pp. 6–21, 2004.
- [4] C. Liu, "Recent Developments in Polymer MEMS," *Advanced Materials*, vol. 19, pp. 3783–3790, Nov. 2007.
- [5] S. Metz, A. Bertsch, D. Bertrand, and P. Renaud, "Flexible polyimide probes with microelectrodes and embedded microfluidic channels for simultaneous drug delivery and multi-channel monitoring of bioelectric activity.," *Biosensors & Bioelectronics*, vol. 19, pp. 1309–1318, May 2004.
- [6] A. Mercanzini, K. Cheung, D. Buhl, M. Boers, A. Maillard, P. Colin, J. Bensadoun, A. Bertsch, and P. Renaud, "Demonstration of cortical recording using novel flexible polymer neural probes," *Sensors and Actuators A: Physical*, vol. 143, pp. 90–96, May 2008.
- [7] S. Metz, R. Holzer, and P. Renaud, "Polyimide-based microfluidic devices.," *Lab on a chip*, vol. 1, pp. 29–34, Sept. 2001.
- [8] Y. Moser and M. Gijs, "Miniaturized flexible temperature sensor," *Journal of Microelectromechanical Systems*, vol. 16, no. 6, pp. 1349–1354, 2007.
- [9] H. Zeng, Z. Zhao, H. Dong, Z. Fang, and P. Guo, "Fabrication and Test of MEMS/NEMS based Polyimide Integrated Humidity, Temperature and Pressure Sensor," *2006 1st IEEE International Conference on Nano/Micro Engineered and Molecular Systems*, pp. 788–791, Jan. 2006.
- [10] A. Arami, M. Simoncini, O. Atasoy, W. Hasenkamp, S. Ali, A. Bertsch, E. Meurville, S. Tanner, H. Dejnabadi, V. Leclercq, P. Renaud, C. Dehollain, P.-A. Farine, B. M. Jolles, K. Aminian, and P. Ryser, "Instrumented prosthesis for knee implants monitoring," in *2011 IEEE International Conference on Automation Science and Engineering*, pp. 828–835, IEEE, Aug. 2011.
- [11] Z. Fan, J. Engel, J. Chen, and C. Liu, "Parylene surface-micromachined membranes for sensor applications," *Journal of Microelectromechanical Systems*, vol. 13, no. 3, pp. 484–490, 2004.

- [12] S. C. B. Mannsfeld, B. C.-K. Tee, R. M. Stoltenberg, C. V. H.-H. Chen, S. Barman, B. V. O. Muir, A. N. Sokolov, C. Reese, and Z. Bao, "Highly sensitive flexible pressure sensors with microstructured rubber dielectric layers.," *Nature Materials*, vol. 9, pp. 859–864, Oct. 2010.
- [13] G. Hill, R. Melamud, F. Declercq, a. Davenport, I. Chan, P. Hartwell, and B. Pruitt, "SU-8 MEMS Fabry-Perot pressure sensor," *Sensors and Actuators A: Physical*, vol. 138, pp. 52–62, July 2007.
- [14] H. Lim, B. Schulkin, M. Pulickal, S. Liu, R. Petrova, G. Thomas, S. Wagner, K. Sidhu, and J. Federici, "Flexible membrane pressure sensor," *Sensors and Actuators A: Physical*, vol. 119, pp. 332–335, Apr. 2005.
- [15] M. Leonardi, P. Leuenberger, D. Batrand, A. Bertsch, and P. Renaud, "A soft contact lens with a MEMS strain gage embedded for intraocular pressure monitoring," *Solid-State Sensors*, pp. 1043–1046, 2003.
- [16] C. Li, P.-M. Wu, L. a. Shutter, and R. K. Narayan, "Dual-mode operation of flexible piezoelectric polymer diaphragm for intracranial pressure measurement," *Applied Physics Letters*, vol. 96, no. 5, p. 053502, 2010.
- [17] M. Leonardi, P. Leuenberger, D. Bertrand, A. Bertsch, and P. Renaud, "First steps toward noninvasive intraocular pressure monitoring with a sensing contact lens.," *Investigative Ophthalmology & Visual Science*, vol. 45, pp. 3113–3117, Sept. 2004.
- [18] S. Glantz and J. V. Tyberg, "Determination of frequency response from step response: application to fluid-filled catheters," *American Journal of Physiology-Heart and Circulatory Physiology*, pp. 1–3, 1979.
- [19] Q. Wang, H. R. Brunner, and M. Burnier, "Determination of cardiac contractility in awake unsedated mice with a fluid-filled catheter.," *American Journal of Physiology. Heart and Circulatory Physiology*, vol. 286, pp. H806–H814, Feb. 2004.

# CHAPTER 7

## Conclusion

*Hell, there are no rules here,  
we're trying to accomplish something.*

*- Thomas A. Edison*

Along this thesis, it has been shown that the microfabrication technologies, born out of the microelectronics industry, permitted the development of a range of MEMS devices that can be employed in the medical field. As MEMS manufacturing has developed, a broad spectrum of materials have been incorporated into devices and this evolution has promoted the development of a variety of tools for producing a diversity of materials on different substrates, and subsequently patterning techniques to fabricate the desired structures. The contributions of this thesis can be summarized by three main applications of MEMS. First, in the development of smart medical instrumentation. Second, in the development of strain sensing elements for artificial knee implants. And lastly, in the development of a catheter-tip pressure sensors. Despite the broad range of applications, the key common element in all these devices is a MEMS strain gauge sensor fabricated using polyimide micro-machining process. The fabrication technology of our thin film strain gauge sensors is based on a Polyimide-Platinum-Polyimide (PI-Pt-PI) sandwich with direct application in the medical field due its biocompatibility. In the following sections a short summary of the major results and accomplishments is given as well as an outlook on future improvements and possible research directions.

## 7.1 Summary of results

In **Chapter 4** we have extended the capabilities of a current available surgical instruments, the distractor, to improve surgical outcome without changing surgical procedures or impose to surgeons new surgical techniques. In contrast with the existing ligament balance tools the developed instrumented distractor allows a manual loading control by the surgeon while providing both measurements of tibial-femoral forces and flexion-extension gaps. By bringing quantitative information with regards to ligament stiffness, in real-time during surgery, can improve ligament balance and consequently surgical outcome. Also, the quantification of such parameters can possibly contribute to validate the way surgeons implant prosthesis at the same time that it can provide useful *in vivo* information for a better understanding of the complex knee joint.

In **Chapter 5** we have demonstrated a polyimide-based MEMS strain-sensing

device for monitoring knee implants. In this research a class of sensors were embedded in the load-bearing materials used in orthopedic components for the monitoring the state of strain and stress in that component. The challenge of developing sensors which can monitor pressure or strain in soft materials while having good response and a minimal effect on the state of stress in that material is significant. Results indicated the measured strain is in accordance with simulated strain and that the applied forces can be estimated from measured strain. The experimental data demonstrates the sensor is capable of measuring the strain associated to the total axial forces in the range of approximately 4 times body weight with a good sensitivity and accuracy for events happening within 1 s time window.

In **Chapter 6** we demonstrated a polyimide/SU-8 catheter-tip MEMS gauge pressure sensor. The polymer-based technology and SU-8 lamination step are well suited for biomedical applications and provide a significant cost advantage over silicon microfabrication techniques. Compared to a silicon-based pressure sensor the polymer-based device was found to show a similar performance in terms of response and sensitivity, despite of being not a true gauge sensor neither an absolute pressure sensor. Finally, the *in vivo* use of this sensor was demonstrated by measuring the heart rate and carotid blood pressure in mice.

## 7.2 Future perspectives

The future of MEMS is very dependent on the market growth but the increasing demand for controlling and monitoring our environment as well as the increasing number of equipments and instruments we interact in our daily lives is driving the MEMS expansion. Perhaps an even greater development of MEMS is occurring on the usage of such devices on identification of the problems and needs on our healthcare system, and which can be solved by this engineering technology and systems methodology. Such increase in demand for MEMS leads to the need for more sensors and devices that can make our healthcare system more effective and efficient while improving the quality of life. Another tendency in MEMS is to investigate production technologies that can be more flexible and affordable, such as printed electronics, pushing the research into

low cost and large surface area devices (e.g. disposable diagnostics devices and solar cells). Last but not least, several devices and products will be developed with the evolution of nanotechnologies, and MEMS will serve to connect the "nano" world with human size world.

In order to avoid the need for wires, sensors must be self sustaining and able to communicate wirelessly and, as a result, other types MEMS devices, such as small energy generating and wireless modules, will need to be developed therefore pushing the evolution of MEMS. As consequence, the increasing number of devices will drive the scaling of MEMS components pushing higher levels of integration. The big advantage of self sustained wireless systems is that it allows the embedding of sensors in previously inaccessible locations as well as it motivates the use of a large number of sensors since batteries are no longer needed.

In the developed devices the data transfer from the strain-sensing element to the computer could be improved by using a telemetry device, such as Triggerfish from Sensimed, to reduce or avoid wires. Actually the devices were conceived having this future integration in mind, therefore the immediate continuation of this work would be to connect our devices to the Sensimed wireless telemetry chip, being one step closer to the end-user application of the devices developed in this thesis.

The inclusion of multiple sensing elements that can simultaneously track geometrical parameters, such as angles, lengths, axes, and mechanical parameters, such as forces and moments, is another future perspective of current work. These additional elements should improve the device capabilities and provide more quantitative biomechanical interpretation. The precise and objective assessment of biomedical parameters is a valuable complement to the medical perception and should definitely lead to a significant benefit for the patient. In addition, the fabrication technology provides assembly flexibility therefore opening up new possibilities for the development of implantable microsystems for human biometric parameters monitoring and animal long term monitoring and testing, where small wireless sensors and no battery are demanded.

Considering the developed devices, for example, the instrumented distractor concept can be applied to other tools, such as screwdrivers that can be used in other types of surgery, or even in production line manufacturing to measure the tightness of a screws. The strain sensing device that monitor knee implants is another potential concept that can be extrapolated to other kinds of prosthesis or even for creating self-sensing devices. Specially with the development of 3D printing techniques that could allow the changing of the printed materials during the printing process, similarly to a multi-head inkjet printer. This could boost the development of a new class of objects capable of monitoring itself and prevent failure at risky situations. The concept presented in the catheter-tip pressure sensor could be applied to other diseases, such as in urinary retention to monitor the bladder pressure. For example, our device could be coupled with and electrode to stimulate the nerves that control the bladder and sphincter muscles in order to empty the bladder at users will, therefore preventing the increasing in bladder pressure that can cause infections and damage the kidneys or the bladder itself. The device can be tuned to monitor other variables such as flow velocity. By rearranging the device sensors on the membrane we can build a hot-wire velocity probe to perform such task.

Thin film and integrated circuit type of micro-fabrication techniques enabled the development of a large number of two- and three-dimensional micro-sensors and sensor arrays. In combination with selective and protective bio-structures, integrated circuit fabrication, and SU-8 and PI micromachining, the structures developed in this thesis can be able to form the basis for cost-efficient, high-quality BioMEMS devices. Particularly to this thesis, the key common element - a MEMS strain gauge sensor fabricated using polyimide micro-machining (PM) process - can be much further developed into an unforeseen and endless range of medical and industrial applications.

# Appendix A - MEMS/NEMS Technology

Microfabricated devices can be made of several miniature structures such as cantilevers, diaphragms, resistors, transistors, flow channels, wells or even proteins and cells. These parts (i.e. moving, static, electrical and chemical sensitive surfaces) when employed in particular sequences can improve existing devices or generate completely new devices with unforeseen applications.

The close relationship between microfabrication and conventional semiconductor fabrication allows the integration of conventional electronic components with microfabricated systems. However, in order to achieve such integration it is necessary to establish process steps that are mutually acceptable. MEMS consolidates such integration by using fabrication processes taken from the semiconductor industry and developing technology specifically for micromachining in a sequence of process steps (process flow) that allow the assemble of several structures to produce a physical device [1]. The great diversity in process steps and materials of the MEMS technology motivates the development of a variety of devices with a large range of possible applications.

The MEMS/NEMS devices can generally be built with a combination of four basic processes. The first is a film growth or deposition, in which different materials can be grown or deposited onto a substrate (e.g. silicon wafer). The second is photolithography, which allows the transfer of patterns into a material. Etching is the third kind of process, which creates features by selectively removing materials in defined patterns. And the fourth step is the usage of techniques to perform the safe release of the microfabricated structures



from the carrier, becoming ready to be used.

## Materials growth and deposition

Different materials (i.e. organic and inorganic) are exploited for a variety of distinct purposes in MEMS/NEMS (e.g. masking materials, structural materials, sacrificial materials, and electrical devices), and two process, either chemical or physical deposition, are usually used to deposit such materials on the carriers. In chemically driven processes the formation of solid materials is made directly from chemical reactions in gas and/or liquid compositions or using the substrate material as a precursor. Examples of depositions that happen because of a chemical reaction are: chemical vapor deposition (CVD), electrodeposition, epitaxy and thermal oxidation. On the other hand, physical depositions (e.g. physical vapor deposition (PVD) and spin coating) are defined when no chemical reaction are involved on the process to form the material on the substrate.

The most common deposition methods used in microelectronics are the low-pressure processes such as sputtering and chemical vapor deposition, and they are very important for the creation of MEMS/NEMS devices [2]. Inorganic metallic materials such as Al, Ti and Pt are usually physically deposited by the sputtering technique. Complementarily, deposition of organic materials such as polyimide and SU-8 are made by the spin coating.

### Sputtering

Sputtering is preferred over other methods such as evaporation due to the wider choice of materials to work with, better step coverage, better uniformity and better adhesion to substrates. During the sputtering, the target (material to be deposited) is subjected to a highly negative potential and bombarded with positive argon ions created in a plasma. Due to the impact of the ions and momentum transfer the target material is ejected and the sputtered target atoms are condensed onto the substrate (placed on the anode). The general concept of the sputtering process is depicted in Fig. 1.

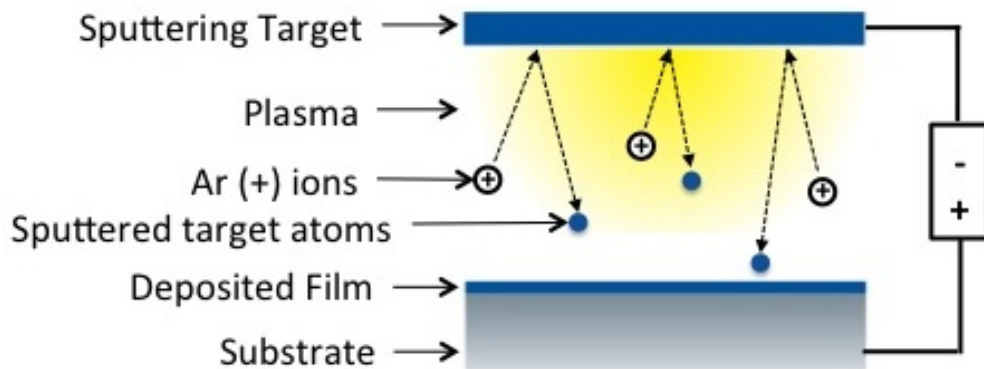


Figure 1: General concept of the sputtering process.

## Spin coating

Spin coating is intensively used in microfabrication in order to uniformly deposit thin or thick organic films onto flat substrates. It is also an important step in the photolithography process for depositing layers of photoresist. The general steps of the spin coating process is depicted in Fig. 2. The process consists of dropping an excess amount of a photoresist solution on the substrate, which is rotated at high speed, so that excess of solution is pushed over the edge of the wafer due to the centrifugal forces, while the residue of photoresist solution on the substrate remains due to surface tension. The thickness of the photoresist will depend on the rotation speed as well as on the concentration of the photoresist solution and the solvent. Once spin coating is complete, the wafer is placed quickly onto a hot plate and heated up to somewhere around 100 °C for several seconds or minutes to evaporate solvent and solidify the photoresist coating.

## Photolithography

Photolithography is a well-known, low-cost, mass-production process used to transfer a pattern envisioned by the designer into a material. A general photolithography process is presented in Fig. 3. A drawn pattern is transferred onto a mask made of a glass plate that has a photo-definable opaque material

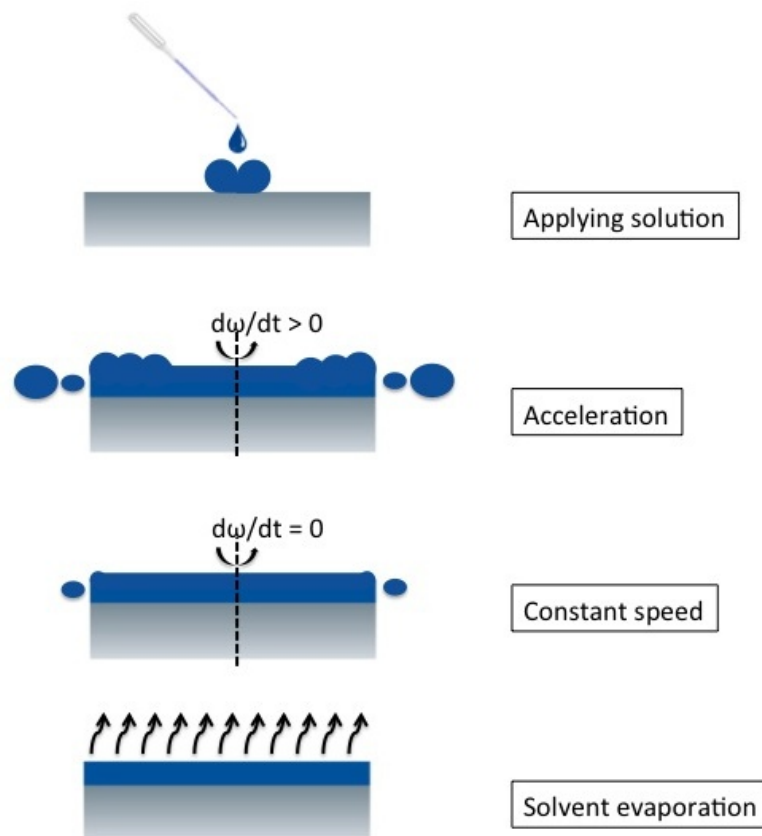


Figure 2: General steps of the spin coating process.

(e.g. chrome). After mask preparation the pattern transfer begins by spin coating a photosensitive material (photoresist) onto the substrate. After spin coating, the substrate and the mask are brought into contact, and ultraviolet (UV) light is shown through the mask onto the photoresist (photochemical cross-linking). In a positive photoresist the transparent portions of the mask will be exposed, causing it to become soluble in a developing solution, while negative photoresist gives the inverse pattern. The wafer and mask are separated, and the exposed photoresist is removed in the developing solution. The photoresist can now be used as a protective mask to transfer the pattern into the underlying material utilizing etching methods or as a shadow mask in a lift-off process.

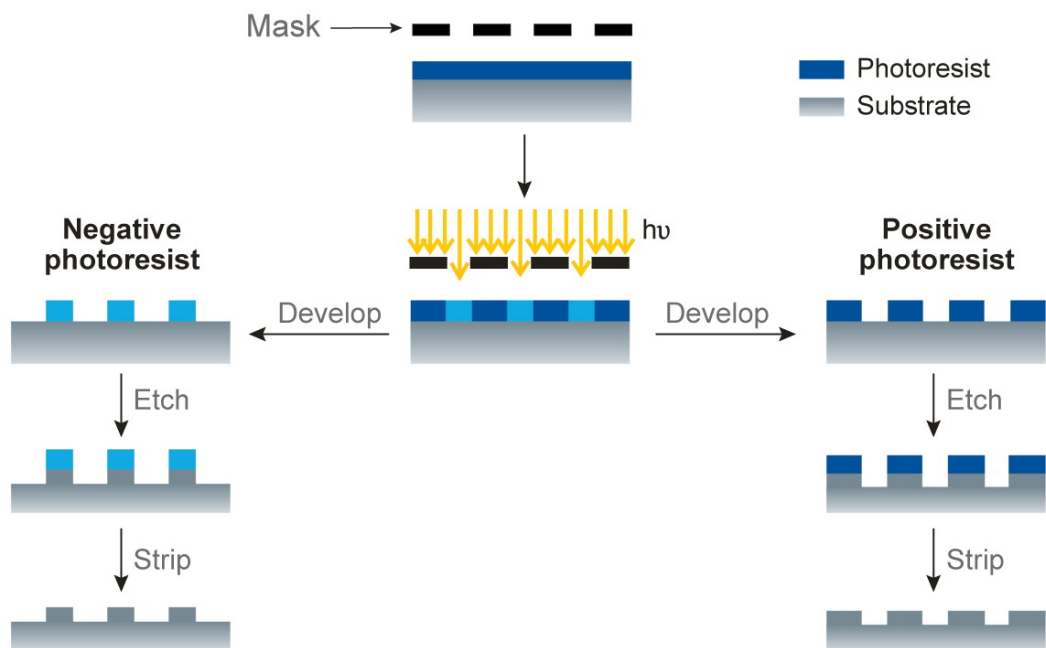


Figure 3: General photolithography process [3].

## Etching

Etching techniques can be divided into wet (using liquid chemicals) or dry (using gas-phase chemistry) etching. Either method can lead to isotropic or anisotropic etching and the etch selectivity is defined as one film etching faster than another film under the same etching conditions. Isotropic etching etches in all directions equally, leading to mask undercutting and a rounded etch profile. Anisotropic etching is directional leading to vertical wall. In general, wet etching is more selective than dry etching and are most often used for isotropic etching, whereas anisotropic etching is more common with dry etching. Dry etching is done in a weakly ionized plasma at low pressure.

Chemical etch processes give good selectivity and isotropic profiles are obtained, but physical etch processes have low selectivity and induce damage from ion bombardment. However, physical etch processes give anisotropic etch profiles, which are extremely important for sub-micrometer semiconductor fabrication. In order to build a MEMS/NEMS device the aim is to find a complementary set of materials and etchants, thus allowing selective pattern transfer.

## **Surface micromachining**

One of the most employed sensor fabrication technology is bulk micromachining using deep wet or dry etching below the surface of the silicon, surface micromachining provides a complementary technique in which materials are added above the surface. These materials often act as spacers or sacrificial layers to be removed at a later stage to produce freestanding structures and moveable parts. Typically surface-micromachined structures use silicon dioxide as the sacrificial layer or hard mask and other materials, such as silicon or metallic films, in the structural layer. In the most basic process the oxide is usually deposited by CVD because this etches more rapidly than thermally grown oxides. The desired patterns are etched in the oxide to form anchor points for the structural layer or to serve a protective layer to remove materials underneath. The challenges with surface micromachining are to control the mechanical properties of the layers, trying to prevent the formation of internal residual stresses and at the same time facilitating the released structures from the surface of the wafer afterwards [4].

## References

- [1] J. Voldman and M. Gray, "Microfabrication in biology and medicine," *Annual review of*, pp. 401–425, 1999.
- [2] M. J. Madou, *Fundamentals of microfabrication: the science of miniaturization*. Boca Raton, FL: CRC Press, 2 ed., Mar. 2002.
- [3] A. J. Torres, M. Wu, D. Holowka, and B. Baird, "Nanobiotechnology and cell biology: micro-and nanofabricated surfaces to investigate receptor-mediated signaling," *Annu. Rev. Biophys.*, vol. 37, pp. 265–288, 2008.
- [4] S. P. Beeby, G. Ensel, and M. Kraft, *MEMS Mechanical Sensors*. Artech House Publishers, Apr. 2004.

## Biography and Curriculum Vitae

Willyan Hasenkamp Graduated in Electrical Engineering from Pontifícia Universidade Católica do Rio Grande do Sul (PUCRS) in 2005 and concluded the Master of Science in Materials Science from Universidade Federal do Rio Grande do Sul (UFRGS) in 2007. Still in 2007 he started the Erasmus Mundus Master of Nanoscience and Nanotechnology (EMMNano), getting double degree Master from the Chalmers Tekniska Högskola, Sweden (2008) and from the Katholieke Universiteit Leuven, Belgium (2009). During the Masters he was part of the research group in Bioelectronic Systems at IMEC, Belgium – the largest European independent research center in nanoelectronics and nanotechnology. In September 2009, he joined the Doctoral Program in Biotechnology and Bioengineering (EDBB) at the Ecole Polytechnique Fédérale de Lausanne (EPFL) – Europe's number 1 university in the field of "Engineering/Technology and Computer Sciences" according the academic ranking of world universities 2009 – under the supervision of Prof. Dr. Philippe Renaud.

Academic Curriculum Vitae: <http://lattes.cnpq.br/1394591111411272>

# Willyan Hasenkamp

e-mail: hasenkamp@gmail.com

## EDUCATION:

- 2009 – 2012**     **PhD in Biotechnology and Bioengineering.**  
*École Polytechnique Fédérale de Lausanne, EPFL, Lausanne, Switzerland*
- 2007 – 2009**     **Double Degree – Master of Nanoscience and Nanotechnology.**  
*Katholieke Universiteit Leuven, KULEUVEN, Leuven, Belgium*  
*Chalmers Tekniska Hogskola, CHALMERS, Gothenburg, Sweden*
- 2006 – 2007**     **Master of Material Sciences.**  
*Universidade Federal do Rio Grande do Sul, UFRGS, Porto Alegre – RS, Brazil*
- 2001 – 2005**     **Bachelor of Electrical Engineering.**  
*Pontifícia Universidade Católica do Rio Grande do Sul, PUCRS, Porto Alegre – RS*

## EXPERIENCE

- 2010 – 2012**     **Medical Devices Consulting – Aleva Neuroprosthetics, Switzerland**
- 2009 – 2012**     **R&D – Microsystems Laboratory – EPFL, Switzerland**
- 2008 – 2009**     **R&D – Bioelectronic Systems Group – IMEC, Belgium**
- 2005 – 2006**     **R&D – Wireless Systems Laboratory – PUCRS, Brazil**

## COMPLEMENTARY EDUCATION:

- 2010**     **Managing Rational Decision Making.**  
*École Polytechnique Fédérale de Lausanne, EPFL, Lausanne, Switzerland.*
- 2010**     **Innovation, Entrepreneurship and Business Development.**  
*Venture Challenge Program, VentureLab, Switzerland.*
- 2010**     **Leadership and Project Management.**  
*École Polytechnique Fédérale de Lausanne, EPFL, Lausanne, Switzerland.*

## PRIZES:

- 2012** - Best Business Idea – Venture.ch – Switzerland
- 2007** - EU Scholarship – Erasmus Mundos
- 2005** - Best Student Award – Class of Electrical Engineering 2005/1.

## INDIVIDUAL COLLABORATIONS:

- Dr. Jimmy Villard: Development of new technologies for spinal surgery.
- Dr. Kristopher Pataky: Development of electrochromic devices and flexible solar cells using low-cost manufacturing.

## ADDITIONAL INFORMATION:

- Personality (typo MBTI): ENTJ.
- Academic CV: <http://lattes.cnpq.br/1394591111411272>
- Hobbies: Basket, soccer, weiqi "The game of Go" and barbecue.
- Personal interests: Entrepreneurship, innovation, philosophy and psychology.

## LANGUAGES:

- Native in Portuguese, fluent in English, and good knowledge of French and Spanish.

## REFERENCE:

- Dr. André Mercanzini – CTO – Aleva Neuroprosthetics – [andre@aleva-neuro.com](mailto:andre@aleva-neuro.com)
- Dr. Philippe Renaud – Director – Laboratory of Micro/Nanosystems – [philippe.renaud@epfl.ch](mailto:philippe.renaud@epfl.ch)